Physics from the Very-High Energy Cosmic-Ray Shadows of the Moon and Sun with Milagro

by

Grant E. Christopher

A dissertation submitted in partial fulfillment
of the requirements for the degree of
Doctor of Philosophy
Department of Physics
New York University

May, 2011

Prof. Allen I. Mincer

In Memoriam
Dedicated to My Grandparents,
Walter and Margaret.

Acknowledgments

I would first and foremost like to thank Allen for all his patience and guidance, without which there would be no chance of me getting to write this. I would also like to thank my committee: Peter Nemethy, Andrei Gruzinov, Michael Blanton and David Hogg.

The whole Milagro collaboration have my thanks; especially Brenda, John, and Petra for working with me and making me feel so welcome in Los Alamos. Andy, Gus, Cy and Bob also deserve my thanks for many useful conversations and communications.

I have had many useful conversations with the department at NYU, and would especially like to thank Kyle Cranmer for conversations about statistics.

Ronnie has been so helpful in pretty much everything, and I owe a few beers for that.

I'd also like to thank Jonathan Roberts for helpful comments on the Sun. After moving into a new office I am lucky to have been able to call on Long, Johnny and George for help.

Finally, it's been a long strange trip and the inspiration for me to complete this work has come from many sources, but in particular I would like to thank Jennifer, Phil and Kat for keeping me going.

Abstract

The shadows of the Moon and Sun in TeV cosmic rays are unique probes of the character of these particles and the magnetic fields they traverse. Milagro was a water-Cerenkov cosmic-ray observatory at an elevation of 2630 m, near Los Alamos New Mexico, which operated from 2000-2008. With continuous operation and a large field of view, the Milagro detector was an ideal instrument for observations of these shadows.

The Milagro data analyzed here are primarily a sample of 700 million events within $\pm 10^{\circ}$ of the Moon and 650 million events within $\pm 10^{\circ}$ of the Sun, collected in 2.5 years from 2005 to 2008.

We investigate the possibility of using the Milagro-measured Moon shadow to perform the first energy scale calibration of an air shower array that is independent of shower and detector simulations. A Moon shadow simulation is found to agree well with data where magnetic field effects are small, but a better model of the magnetic field will have to be implemented in order for a conclusive energy scale determination to be made.

An antiproton component is expected in TeV cosmic rays as a result of spallation in the interstellar medium. This gives rise to a Moon shadow deflected in the opposite direction to the particle shadow. A simulation-free fit is performed over a probable range of parameters describing the antiproton Moon shadow. Using the simulation-determined proton trigger fraction of 72% yields 95% upper limits on $\bar{p}/p$ of 3.4 to 3.9%. This is currently the most stringent upper limit at TeV energies.

The Milagro-measured solar shadow probes the Sun's magnetic field, as solar activity and the sunspot number decreases over the second half of solar cycle 23, in the first study of the coronal magnetic field using the cosmic-ray shadow. We find a strong time dependence of the depth of Sun's shadow, which is anti-correlated with sunspot number. Simulating the Sun's shadow, using a dipole model of the coronal field, results in a good fit to data close to solar minimum.

Contents

List of Figures

List of Tables

Chapter 1

Overview of Cosmic Rays

As the centenary of the discovery of cosmic rays draws near, many fundamental questions about their nature remain unanswered. They consist primarily of protons and heavy nuclei that are incident on Earth with a high degree of isotropy, due to their scattered paths in galactic magnetic fields that obfuscate their origins. Current observations of cosmic rays span 14 orders of magnitude in energy: the highest energy cosmic rays ever observed had as much energy as a little-league baseball, 3.2×10^{20} eV [1]. Since their discovery, we still do not have answers to the following questions:

1. What are the sources of cosmic rays?
2. How are they accelerated to such high energies?
3. What is their composition?

We have potential solutions to these questions –we think sources of cosmic rays are supernovae [2], and other objects from late stellar evolution for lower energy

galactic sources, whilst the highest energy sources must be extra-galactic due their high rigidities, but the debate still rages about their origins between active galactic nuclei [3] and the γ-ray burst sources. We think the mechanism for acceleration lies in shock fronts expelled by supernovae; but modeling accelerations to reproduce energies and spectra is difficult (see [4] and references therein). We also have evidence that the sources of cosmic rays also produce γ-rays [5] and neutrinos [6]. Unlike charged particles, neutrinos and γ-rays, are neutral so are not deflected by magnetic fields. If they are produced close to cosmic-ray sources they therefore provide a window directly back to the source.

1.1 Very High Energy Cosmic Rays (VHE CR)

The lowest energy cosmic rays are a few MeV and at these energies the solar wind will wash them away from Earth. At the equator, only cosmic rays above approximately GeV energies may penetrate the Earth's magnetic field [7]. A few orders of magnitude higher in energy are the $\sim$TeV cosmic rays that concern us in this thesis. These are known in the literature as Very High Energy (VHE) cosmic rays and are defined to lie in the energy range 30 GeV-30 TeV. For a recent review of VHE CR and γ-ray astronomy see [8].

The spectrum of cosmic rays incident on Earth can be described as a power law of the form

$$\frac{dN}{dE} = AE^{-\alpha} \tag{1.1}$$

where α lies in the range 2.5-3. An image of the full cosmic-ray spectrum is shown in fig. 1.1. The low-energy region of the spectrum has a spectral index $\alpha \sim$2.7. The

spectrum steepens around 1-10 PeV and beyond this point, known as the knee, the spectral index is $\alpha \sim 3$. Finally, the ultra-high energy spectrum flattens again, at around 1-10 EeV, which is known as the ankle. Physically, it is thought that the ankle represents the transition of cosmic-ray origins from galactic to extra-galactic [9]. Below the knee, all cosmic rays are thought to be galactic in origin [2], having been confined in the galaxy for approximately 10^7 years in the $\sim \mu$G galactic magnetic field.

1.2 Detection of VHE CR

Since the flux of cosmic rays on Earth at VHE is low, (about 1 every 3 minutes per m^2 at 1 TeV) any detector must have a large detection area and so must be ground based. However, the atmosphere is opaque to cosmic rays and γ-rays. When a primary particle interacts with atmospheric molecules, typically at a few tens of km above the surface of the Earth, a chain reaction occurs producing millions of particles. This is known as an Extensive Air Shower (EAS).

1.2.1 Extensive Air Showers

An EAS begins when an incident cosmic-ray primary interacts strongly with an atmospheric nucleus, such as nitrogen or oxygen. The amount of atmosphere traversed before the initial interaction is dependent on the CR-air cross section, and for TeV cosmic rays this grammage (density$\times$distance traversed) is approximately 37 g/cm^2. The atmosphere down to sea level corresponds to an atmospheric overburden of approximately 1000 g/cm^2; therefore the cosmic ray has a vanishing

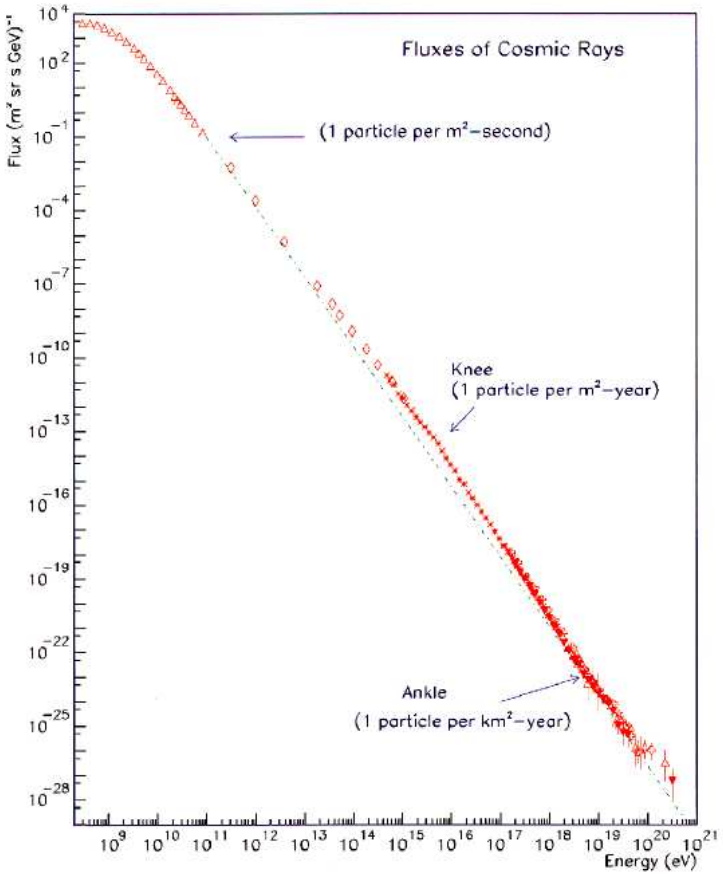

Figure 1.1: The full cosmic-ray spectrum.

probability of getting close to ground level without interacting.

The initial collision results in fragmentation of the atmospheric nucleus hit by the primary. This first interaction produces baryon-antibaryon pairs, which produce hadronic jets. However, the majority of particles produced are pions. The π^0s decay into photons and induce electromagnetic showers in which the photons pair produce electron/positron pairs. These in turn emit high-energy photons via bremsstrahlung, which themselves can pair produce. This cyclic process produces an electromagnetic cascade.

The $\pi^{\pm}$ decay into muons and neutrinos. The muons are extremely penetrating and if the decay length is longer than the interaction length the muons will get to ground level. Otherwise, the muons may decay into electrons/positrons. The reaction chain for all these processes is shown in fig. 1.2.

An EAS grows in number of particles nearly exponentially until the energy losses of the e^+/e^- are dominated by ionization losses, rather than radiation processes. This occurs when the energy of particles produced is $\sim$80 MeV and point is known as shower maximum; beyond which the number of secondary particles decreases towards the ground.

Non-Hadronic Primaries

Other than hadronic primaries, γ-ray primaries may occur, but on the order of 10^{-4} relative to cosmic rays at TeV. Electronic and positronic primaries also occur, with electrons at a similar 10^{-4} level at TeV, and a much lower, positron flux. Simulations of TeV proton and photon initiated showers are shown in fig. 1.3.

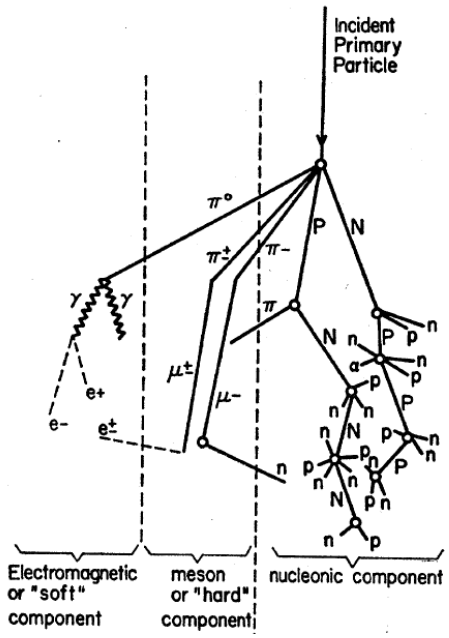

Figure 1.2: The development of a CR-initiated EAS, taken from [10].

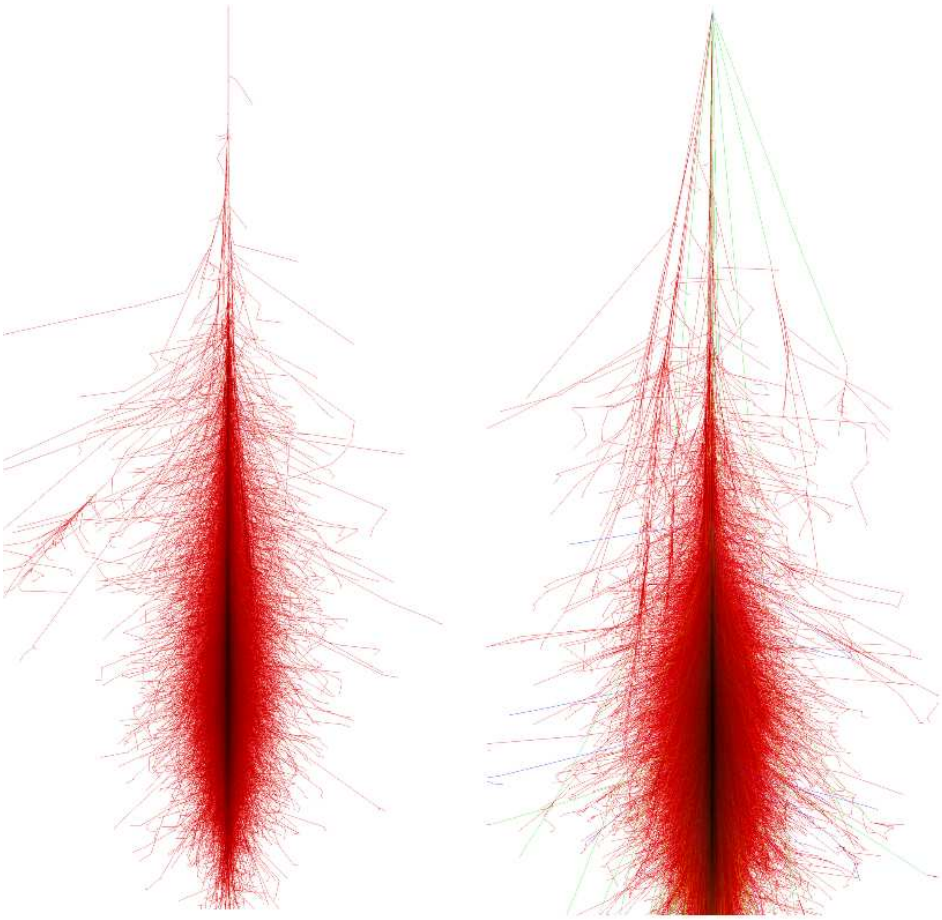

Figure 1.3: EAS showers generated by CORSIKA. The image on the left is a from a 1 TeV photon primary and the image on the right is a from 1 TeV proton. The images are color coded, so the red tracks are electromagnetic, the green tracks are muons and the blue are hadrons. Taken from [11].

EAS Shape at Ground-Level

The EAS is highly beamed: through full shower development it extends tens of km on-axis, but only few tens of meters laterally. The shower arrives at the surface of the Earth at 100 m or so in radius and a few meters thick -a kind of parabolic pancake.

The lateral development of the shower is due to the electrons/positrons undergoing multiple Coulomb scattering from electric fields of nuclei and photons Compton scattering from atomic electrons. The lower energy secondaries and tertiaries will scatter farther and as a result will end up farther from the shower core, which is defined as where the primary would arrive, at ground level, without interactions. The particles farther from the core, being lower in energy, travel slower than those close to the core giving the EAS a non-planar shape. The mixture of particle energies and speeds gives a typical TeV shower a 1m thickness on-axis.

1.2.2 Air Shower Array Detectors

Air shower array detectors are designed to detect the EAS at ground level. Examples of arrays operating in the VHE part of the spectrum are Tibet AS-γ [12], ARGO-B [13], Milagro, and its yet-to-completed successor HAWC. A picture of the Tibet AS-γ detector is shown in fig. 1.4.

The principle behind air shower arrays is to use the atmosphere like layers of a calorimeter, but at ground level we see only a sample of particles at the tail-end of the shower. Arrays detect secondaries and tertiaries from the EAS, so the altitude of detection governs the number of particles in the shower at detector

level. This governs the energy threshold of the detector. Higher energy primaries produce more particles in the EAS, and the probability of shower being detected is a strong function of the number of particles reaching the detector level. At higher altitudes low energy showers contain more particles, so are more likely to be detected. Therefore the higher the altitude of the detector, the lower its energy threshold.

The direction of the primary is, to a good approximation, perpendicular to the layer of particles formed in the EAS. It can be reconstructed using an array of detectors (often scintillator counters), each of which measures hit size and hit time of from EAS particles. The hit times and hit sizes for each detector in the array are then used to reconstruct the EAS shower front and hence the direction of the primary.

In their favor, arrays have high duty cycles and large fields of view, which is useful when observing extended emission [14], and other large scale features, such as the cosmic ray anisotropy [15]. However, air shower arrays suffer from poor angular resolution.

Milagro

Milagro uses the water-Cerenkov technique, which it pioneered, rather than scintillator to detect the secondaries and tertiaries at ground level. At Milagro's altitude there are approximately five γs for every e^+/e^- pair in the EAS. When passing though water the γs either pair produce, or transfer their energy to electrons via Compton scattering. Then, any charged particles traveling faster than the speed of light in the medium will produce Cerenkov light. In water, particles radiate

Figure 1.4: The Tibet AS-γ array near Yangbajing, Tibet, located 4300m above sea level [16].

visible blue Cerenkov light in a wide 42° cone. So, this technique uses water as both a detection medium and to transfer the energy of the air-shower photons to charged particles, so a much larger fraction of shower particles can be detected than in other arrays. This leads to high sensitivity for showers with lower primary energies than would otherwise be possible.

Cerenkov Radiation

The speed of light in a medium of refractive index n is c/n, where c is the speed of light in a vacuum. Cerenkov radiation is produced when a charged particle travels at super-luminal speeds (faster than the speed of light in that medium). As charged particles pass through the medium it becomes locally polarized, as the particle attracts like charges. This polarization is totally symmetrical. However, if the particle speed is super-luminal the polarization charges cannot arrange themselves rapidly enough in the medium. The arrangement of poles is still symmetrical

azimuthal to the motion, but behind the particle a cone of dipoles develops, producing a dipole field in the medium. This field collapses with Cerenkov radiation being emitted as a light cone at a fixed angle θ_c with respect to the motion of the particle:

$$\cos\theta_c = \frac{c}{nv} \tag{1.2}$$

where v is the velocity of the particle, n is the refractive index of the medium and c is the speed of light in a vacuum. The energy threshold, above which a particle will emit Cerenkov light, as a function of rest mass m_0 and index of refraction is given by

$$E_{threshold} = \frac{m_0 c}{\sqrt{1 - \frac{1}{n^2}}} \tag{1.3}$$

In an array of scintillators, particles must directly hit the scintillator material for detection. In the water Cerenkov technique however, with the correct geometry of light-sensors, any Cerenkov light in the water will be detected, which covers a potentially much larger area than expensive scintillator material.

Using eq. 1.3, we find that the threshold for Cerenkov radiation production is 0.76 MeV for electrons, 0.16 GeV for muons and 1.4 GeV for protons. These are the energy thresholds for detection with the light sensors in Milagro. The Milagro detector is described in detail in the following chapter.

Chapter 2

The Milagro Detector

Milagro was a ground-based water Cerenkov detector in the Jemez Mountains near Los Alamos, New Mexico (35.88°N, 106.68°W), at 2630 m above sea level, which corresponds to an atmospheric overburden of 750 g/cm^2. It was designed as a γ-ray instrument and was sensitive in the VHE (TeV) region of the spectrum. It operated day and night from 2000 to 2008, leading to a duty cycle of >90% and had a large (2 steradian) field of view.

This chapter outlines how Milagro detects cosmic rays and how the arrival direction is reconstructed. In section. 2.1 we describe the physical instrument. Then, in sec. 2.2 we describe the electronic system designed to extract hit-times and hit-sizes, from the photomultiplier tubes (PMTs) that detect Cerenkov light initiated by particles in the EAS. Once we have the hit-time and size from each PMT, the electronics must determine if the signals are from an EAS event. To do this we need an event trigger, which is described in sec. 2.3. If an event triggers the detector, using the hit-times and hit-sizes for each PMT, the Milagro reconstruction

Figure 2.1: Inside the Milagro pond, before any PMT installation. The pond is about the size of a gridiron football field. The grid positions correspond to eventual PMT positions.

algorithms are used to reconstruct the incident primary particle direction from the EAS, which is described in sec. 2.4. Finally, sections 2.5 and 2.6 discuss detector variability.

2.1 Detector

The detector consisted of a central pond and 175 outrigger detectors, all filled with water and two nearby buildings to house the electronics. The site was chosen as the pond already existed from a geothermal experiment at Los Alamos National Lab. The exposed mountainous location left the equipment open to electrical storms so it was covered in a giant Faraday cage to protect the electronics.

2.1.1 Pond

The pond contained 24 million liters of water, covered with a light-tight 1 mm layer of polypropylene. The cover had to transmit no light, so the detector would be sensitive to single photons in the pond during the day. This cover was held in place in inclement weather by a series of high tension nylon cables criss-crossing the cover sheet. To perform repairs the cover was inflated and raised about 20 ft above the surface of the pond. The inside of the pond is shown in fig. 2.1 and a schematic of the pond is shown in fig. 2.2.

To detect Cerenkov light from charged particles the pond contained two layers of PMTs. The top, or Air-Shower-layer (AS), had 450 PMTs under 1.5 m of water on a 2.8 m×2.8 m grid. The bottom, or MUon-layer (MU), had 273 PMTs under 6 m of water arranged on a 2.8 m×2.8 m grid; offset from the AS-layer by half a grid spacing, as shown in fig. 2.3.

At Milagro's altitude, secondary particles in a TeV EAS are nearly all electromagnetic, with roughly five γs for every e^+/e^- pair. The AS-layer was in place to detect the Cerenkov light from these electromagnetic particles, as described in section 1.2.2, so was placed under 1.5 m or 4 radiation-lengths of γ in water. The amount of water above the PMT was large enough so that nearly all photons could convert into an e^+/e^- pair, but not so thick so the light produced at the top water level is absorbed before it reaches the PMT and the exact value was determined from simulations.

The muon layer was under 6 m, which corresponds to 16 radiation-lengths of γ in water; hence only muons and hadrons reach the MU PMTs. The MU-layer

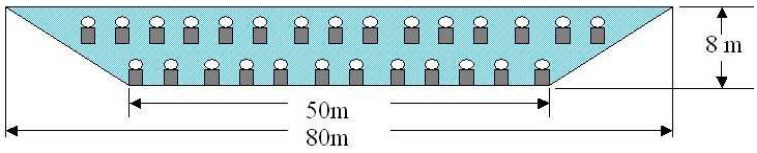

(a) Dimensions of the pond from [17]

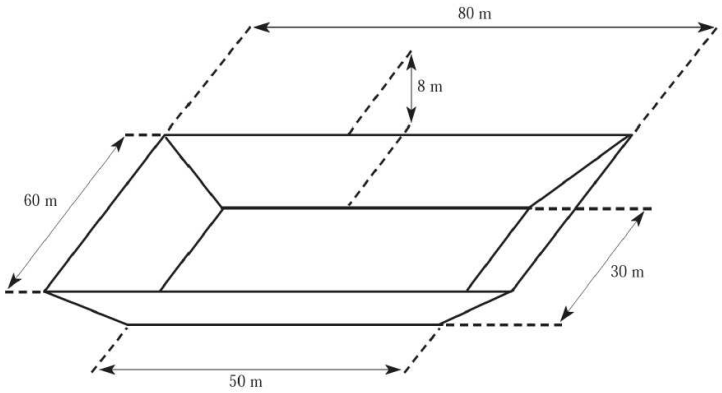

(b) Air Shower (AS) and Muon layers (MU) [18]

Figure 2.2: Schematics of the Milagro pond.

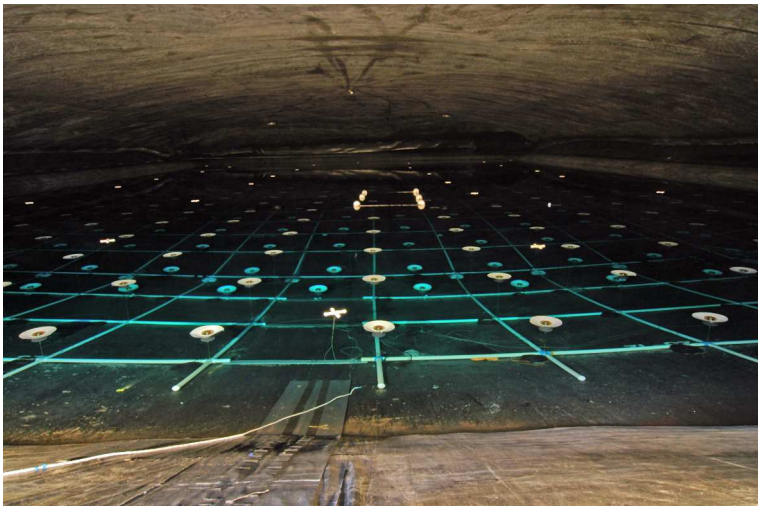

Figure 2.3: The Milagro pond with two layers of PMTs. The top layer is the AS-layer, used for direction reconstruction and timing. The bottom layer is the MU-layer used for γ-hadron separation. The water is low as we were draining the pond.

was therefore used in gamma-hadron separation. Muons as low as 1.2 GeV could reach the MU-layer.

Water Filtration

The detector relies on detecting Cerenkov light in water, so needs the water to be very clear, i.e. have a high attenuation length. In order to keep the pond clear the water was pumped to a building on-site and filtered. While the pump was online, it recirculated the water at 200 gallons per minute. The water passed through a series of filters: charcoal, 10 μm, 1 μm, carbon and finally a UV filter to kill any organisms. The attenuation length of the water was regularly checked and a test before the Milagro went offline found the attenuation length to be 17 m, for UV of wavelength 325 nm.

In early Milagro epochs (see sec. 2.5), aluminum baffles were placed on the PMTs in the pond. These corroded and significantly reduced the attenuation length in the pond. The aluminum baffles were removed and replaced with plastic baffles, then, after filtration, the pond attenuation length returned to previous levels. The outrigger tanks were not filtered and were left largely untouched after their installation. When the detector was dismantled in 2008, the water quality in the outriggers was found to have a high attenuation length.

2.1.2 PMTs

To collect the Cerenkov light emitted in the water, Milagro used photomultiplier tubes to detect and amplify the signal. The PMTs (fig. 2.4) were Hamamatsu

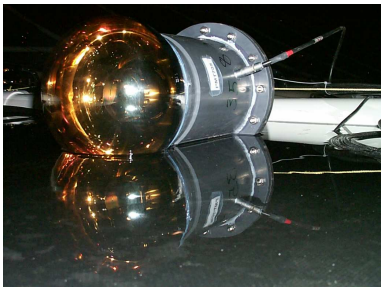

Figure 2.4: A Milagro PMT.

#R15912 SEL, had an 8" diameter and were surrounded by a conical polypropylene baffle with white interior and black exterior. The baffle simultaneously blocked light from the problematic single muon events (low altitude muons traveling across the length of the pond) and increased the light-collection area.

PMTs detect Cerenkov photons and output an amplified electrical signal. The electrical signal is provided by a cascade of photo-electrons (PEs); the number of which is a measure of the hit-size, or energy and number of Cerenkov photons, detected by the PMT. The high voltage supplied to the PMT and the signal read from the PMT both used the same RG-59 cable to reduce the wiring in the pond.

2.1.3 Outriggers

The outriggers extended the physical area of the detector from 5,000 m^2 to 40,000 m^2. The outrigger positions, with the pond, are shown in fig. 2.5. They were installed in increments, from 2001 to 2003, primarily to improve the core-location of EAS in data reconstruction. There were 175 outriggers, each containing a single PMT. Each outrigger was a 5,680 liter tank of water, measuring 2.4 m in diameter,

Figure 2.5: The Milagro detector: the pond with the positions of outriggers.

1 m in height and lined with a Tyvek light reflector. The PMTs in the tank were downward facing.

2.2 Extracting the Hit-Size and Hit-Time from each PMT using Milagro Electronics

This section describes how hit-times and sizes from 898 PMTs were extracted for each EAS and were selected to be digitized. The electronics used to extract these quantities is shown in figure 2.6.

2.2.1 Time Over Threshold Mechanism

PMTs were powered in groups of 16. Each group had its own Front End Board (FEB), to extract the hit-time and hit-size information, and to control the high

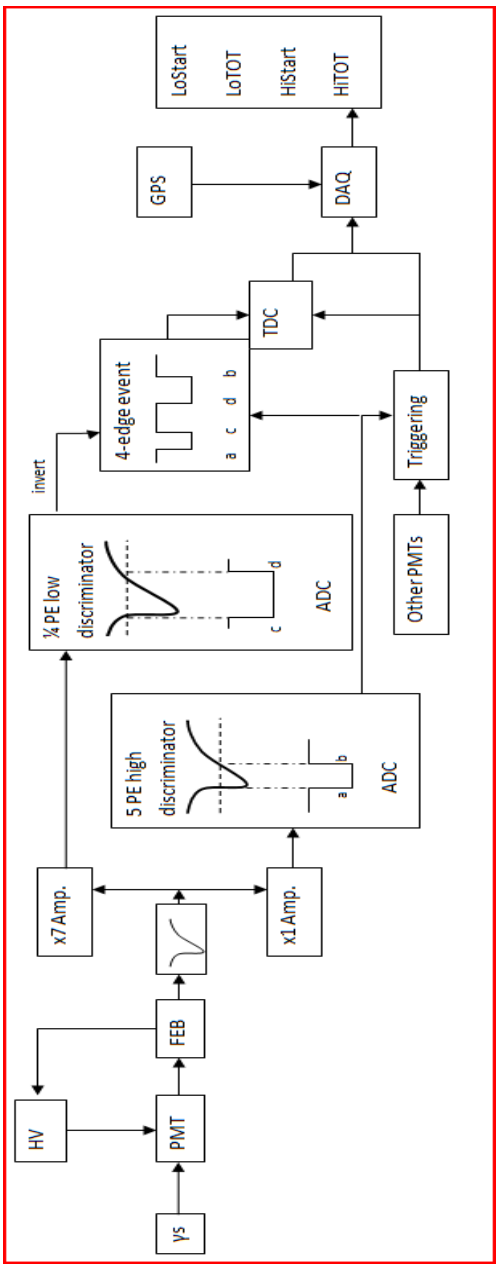

Figure 2.6: Milagro Electronics used to get hit-time and size in the TOT method.

voltage distribution to the 16 PMTs. To calculate the hit-size, that is the number of PEs, the time over threshold (TOT) method was used. The basic idea behind TOT is that the hit-size—the signal strength of the pulse from the PMT—is proportional to the time that the signal spends over some preset threshold.

The first stage in this process is reading the PMT raw signal. This is done with an RC circuit with a 100 ns time constant. The 100 ns was chosen to minimize late-light effects. If two pulses occur, from multiple Cerenkov photons, in a shorter duration than the time constant for the RC circuit the pulses will be indistinguishable and one large pulse will be seen. The voltage on the capacitor in the RC circuit is given by

$$V(t) = \frac{Q}{C} e^{-t/RC} \tag{2.1}$$

so the time over some threshold (TOT) is proportional to the log of the charge of all the PEs and is thus a measure of hit-size. The exact relations for each PMT are known from calibrated measurements.

The signal is read from the PMT with the FEB and split into two signals. The first signal, sent to a high-gain amplifier ($\times 7$), is required to pass a low discriminator threshold of 1/4 PE. The second signal has low amplification ($\times 1$) and is required to pass a high discriminator threshold of 5 PEs.

2.2.2 Time to Digital Converters

Each time an event crossed a threshold an edge of the form in fig. 2.7 was generated. This was digitized using a LeCroy FASTBUS Time to Digital Converter (TDC), which could record up to 16 edges per event, and was sent to the Data AcQuisition

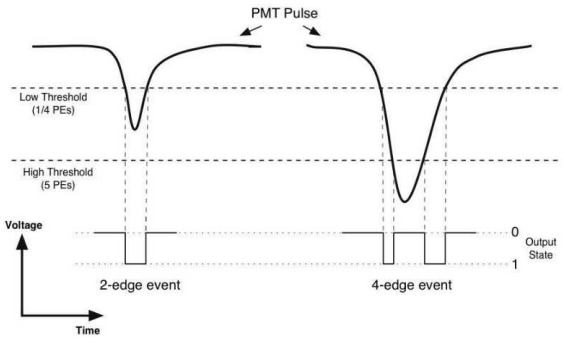

Figure 2.7: The time over threshold method (TOT): each time the PMT pulse crosses one of the thresholds an edge is generated. If the pulse crosses both the high and low thresholds four edges are generated, if only the low threshold is crossed only two are. Taken from [19].

system (DAQ). Pulses that cross only the low threshold digitally generate square wells, or 2-edged events, shown in fig. 2.7 and the events that cross both thresholds are the double square wells, or 4-edged events. For each event that crossed the discriminator threshold a fixed pulse of height 25 mV and duration 180 ns was sent to the trigger logic, with the pulse duration chosen based on shower geometry.

2.3 Milagro Trigger

The maximum event rate of the DAQ was 2000 Hz. The Milagro trigger was designed to keep the event rate below this ceiling.

2.3.1 Multiplicity Trigger

The original trigger, known as a multiplicity trigger, was purely using the AS-layer. A running total of the analog sum of PMT outputs was kept. If the output exceeded the preset threshold, of 60 AS PMTs hit within 180 ns—the pulse time sent to the trigger when PMT signals pass the discriminator—an event was triggered.

2.3.2 Single Muon Events

It is advantageous to reject low altitude (or high zenith angle) muons traveling across the pond at trigger level. A muon arriving at an altitude close to the angle of Cerenkov emission will produce horizontal light that may trigger many PMTs –just like an EAS. However, this light travels through the pond at c/n but the time profile of an EAS from near zenith has many particles and moves though the pond at particle velocity c. Using this profile information in successive triggering methods, the single muons have been rejected with 85% accuracy at the trigger level since March 2002.

2.3.3 Multiple Trigger Conditions with the VME Card

A Versa Module Europa (VME) card was implemented in Nov 2002, close to the beginning of epoch 7 (see sec. 2.5). This enabled the use of risetime in conjunction with multiple trigger conditions. The risetime was defined as the time interval between 10%-90% of the amplitude of an analog sum that triggered the detector.

Events that are unable to be fitted using the event reconstruction algorithm are characterized by longer risetimes, so can be thrown out at trigger level. For large

hits the risetime is longer, but the events are more likely to pass the reconstruction algorithm. Based on this, the following trigger conditions were selected. These lowered the energy threshold of recorded events, whilst keeping the event rate below the DAQ limit of 2000 Hz, and also cutting out a large number of single muon events. The trigger became:

- N_{AS} >20 & risetime<50 ns
- N_{AS} >53 & risetime<87.5 ns
- N_{AS} >74

2.3.4 Post-VME Card Multiplicity Triggering

In April 2006 (epoch 8 –see sec. 2.5) the VME card failed and the trigger was returned to a multiplicity trigger. However, the new multiplicity algorithm was able to cut out far more of the single muon events than the previous one. This was because for an EAS, the analog sum will rise faster than a low altitude single muon event, so this was included in the new algorithm.

2.4 Online Event Reconstruction

In the event reconstruction, the hit-times and hit-sizes from each PMT, for triggered events, are used to reconstruct the shower core position and subsequently the incident direction of the primary in the EAS. The principle behind shower reconstruction using PMT hit-times is shown is fig. 2.8. The accuracy of the positions of each PMT needed to be within ±0.03 m horizontally and 0.01 m vertically, so the

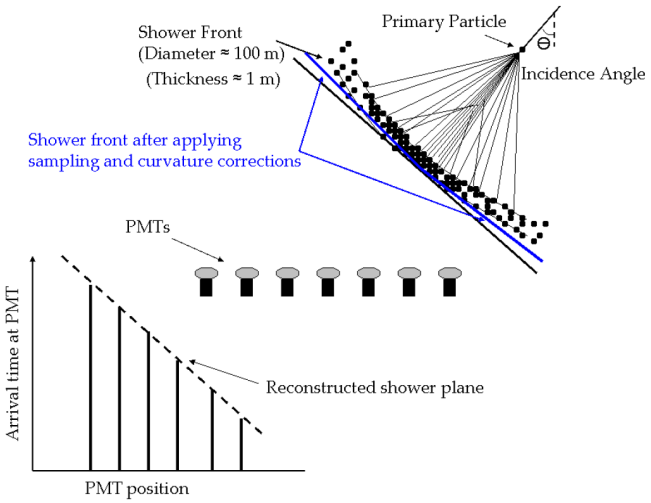

Figure 2.8: Conceptualization of primary direction reconstruction using an EAS with the water-Cerenkov technique.

resulting angular uncertainty in reconstruction was significantly smaller than the angular resolution and errors from other contributions. The event reconstruction proceeds as follows:

- Correct the hit-times of the PMTs for slewing (sec. 2.4.3) and the time to pass through the electronics.
- Find the location of the shower core (sec. 2.4.4).
- Correct for the curvature of the shower (sec. 2.4.5).
- Correct the measured arrival time due to sampling effects (sec. 2.4.6).
- Find the direction of the shower plane using the reconstruction algorithm

(sec. 2.4.7).

2.4.1 Data Acquisition System

The DAQ consisted of a master PC and several workers, which were on site. The DAQ was designed to convert a series of raw timing edges from the TDC—which contained hit-time and hit-size information—to physical arrival times and hit-sizes. From choices of raw timing edges the event time was the time at which the low/high threshold is first crossed, registered from a GPS clock. The high TOT threshold (HiTOT) and hit-time (HiStart) are preferred to that from the low threshold (LoTOT and LoStart) as pre or post pulsing of the PMT will not cross this threshold. This information was used to find the shower core and finally the primary direction, as described in the following sections.

2.4.2 Data Storage

The data was stored in two copies, at Los Alamos and the University of Maryland at a rate of approximately 5 GB a day. Data was split into Runs and SubRuns. Each SubRun contained about 5 minutes of data. Raw data, including TOT, the hit-times and the analog sum, were stored for the Moon and the Sun as well as the Crab Nebula, Mrk 421 and Mrk 301. To ensure the system was working correctly, or to troubleshoot, a member of the Milagro collaboration was always on call monitoring the system.

2.4.3 Timing Calibration Corrections

Once the raw hit-time was chosen from timing edges (LoStart or HiStart), there were two corrections applied to the hit-times of each PMT.

Electronic Timing Correction

The first correction was the signal travel time through the electronics. This was corrected by pulsed lasers with known arrival times in the pond. For a laser pulse calibration, the light was sent through optical fibers that carried the light to 30 diffusing balls that stayed in the pond. An optical switch allowed the light to be sent to any one of the diffusing balls which would then illuminate the pond and be detected by the PMTs. Based on the known arrival times in the pond of the laser light, new laser calibration constants, to correct for electronic timings, were produced for each PMT periodically.

Electronic Slewing Correction

The second correction occurred because analog PMT pulses have a finite risetime. This can be seen in the digitization of signals in fig. 2.7. Large pulses, that is pulses generated from more than one Cerenkov photon, crossed both the high and low thresholds before smaller pulses. Known as electronic slewing, this was corrected by individual calibration constants for each PMT that measured start time as a function of TOT for various pulse heights.

2.4.4 Core Location

The core location, which is the location a primary particle would hit if there were no interactions, was estimated using the center of photoelectron function:

$$x = \frac{\sum_{i=1}^{N} x_i \sqrt{PE_i}}{\sum_{i=1}^{N} \sqrt{PE_i}}$$
$$y = \frac{\sum_{i=1}^{N} y_i \sqrt{PE_i}}{\sum_{i=1}^{N} \sqrt{PE_i}} \tag{2.2}$$

The weighting of the number of photoelectrons was by square root rather than a linear weight so that fluctuations causing big hits on individual PMTs did not wholly dominate the fit. The hit-size of a PMT from individual charged particles showed large variations in tests, due to differing penetration depths of the particle in the water. The point on the surface of the PMT the particle hit was even more important in determining the hit-size, as the number of PEs produced was a strong function of the hit position.

Nothing further was needed if the core was on the pond for early epochs. However, this was unlikely as the showers have large areas and could easily trigger the detector whilst landing far off the pond. Hence, before the addition of the outriggers there were problems in core location; which in turn effected angular reconstruction. Before the outriggers were installed, any event off the pond was fixed to have a shower core 50 m from the center of the pond, in the direction of the center of photoelectrons.

After the addition of the outriggers, the above equation was used with only AS-layer PMTs if the core was determined to be on the pond; or only with OR PMTs if the core was off the pond. The choice of the core being on or off the pond

was made based on the ratio of AS-layer PMTs hit to outriggers hit.

A more sophisticated and accurate method was used in later Milagro epochs to find the shower core. This fitted the shower to a 2-D gaussian with a χ^2 minimization using both AS and OR PMTs.

2.4.5 Curvature Correction

A shower core is not planar as it hits the detector –it is parabolic. Using a fitting function on this well known shape is soluble, but requires too much computation time. Instead, we added a timing correction based on distance from the fitted core, which in effect flattened the shower.

Therefore, to successfully reconstruct the primary direction, the core of the shower is found and the curvature correction of $\sim$0.07 ns/m is applied, before the direction is reconstructed.

2.4.6 Sampling Correction

Each EAS, at detector level, was a pancake of high and low energy particles of different types that could trigger the detector. However, a trigger is a probabilistic event, so increases in likelihood where the density of particles is greater. The PMTs have a quantum efficiency (the ratio of primary PEs to Cerenkov photons) of 0.2-0.25. An event detected closer to the shower core (where the particle density is greater) is likely to be recorded earlier than an event further from the shower core. So, there was a correction applied to the hit-times for each PMT which was a function of core distance and hit-size.

2.4.7 Direction of Primary

We reconstruct the direction of the primary assuming that the shower is planar, (which was a good approximation after the curvature correction) and assuming that the direction of the primary is perpendicular to this plane. Then, the hit of the ith PMT at coordinates (x_i, y_i) is given by

$$T_i = Ax_i + By_i + T_0 \tag{2.3}$$

where A and B are constants to be determined, that describe the primary direction and T_0 is an overall time constant for the event.

This planar function is then fitted by a weighted χ^2 minimization, with 5 iterations. The weight is the number of PEs, where bigger PMT hits produce more PEs and hence a higher weight. The weights are assigned after study of the T_i distribution, which is not gaussian. If it was assumed to be gaussian some outlier events, usually from scattered light or noise, would distort the whole fit. Hence for the first iteration only PMTs with a large number of PEs are used. For each iteration the PE threshold is lowered until the 5th iteration, at which point an event is recorded, with the number of PMTs used in the final stage of the fit (N_{fit}), or the event is discarded as unphysical. From tests with simulated data, this angular reconstruction method fitted $\sim$90% of events to within 1°.

2.4.8 Gamma-Hadron Parameter

Milagro was designed primarily as a γ-ray detector. To distinguish between cosmic rays and γs, the the bottom layer of the pond (the MU-layer) was used to detect

muons. These are much more probable in cosmic rays than electromagnetic showers, and tend to appear in clumps from individual electromagnetic cascades within the whole EAS, as discussed in section 1.2.1. Primary γ-rays, on the other hand, give an electromagnetic EAS that is more uniform at detector level. This thesis is concerned only with cosmic rays but for further discussion of γ-hadron separation with Milagro see [20].

2.5 Epochs in Milagro

Data in Milagro is divided into nine epochs, which are defined in table 2.1. Post epoch 3, all the outriggers had been installed, which dramatically improved the performance of the detector. The other principal epoch to epoch changes were in the algorithms for the trigger, core fitting and direction reconstruction, which are discussed in the previous sections.

From table 2.1, we can see the proportion of dead PMTs varies through the course of Milagro's lifetime. The vast majority of data in this thesis is taken from the most stable and similar epochs of 7, 8 and 9. That is, epochs 7-9 had nearly identical numbers of live PMTs, and the reconstruction, core and triggering algorithms were similar. However, for instance, in epoch 6 there were a large number of dead PMTs (10%) in the AS-layer. This alters, among other things, triggering and angular reconstruction and any analysis must take these changes into account.

Many parameters, such as N_{fit}, are not stable between epochs and analyses of Milagro data between epochs need to bear this in mind.

Epoch	start date	days	% dead AS/MU/OR	trigger	fitter	core finder
1	07/19/00	131	5/5/-	multiplicity	AS	COM
2	12/10/00	382	5/5/-	multiplicity	AS	off pond
3	01/11/02	430	5/5/-	VME	AS	off pond
4	05/18/03	430	5/5/3	VME	AS	COM+OR
5	10/06/04	471	8/5/2	VME	AS/MU/OR	gauss
6	04/01/05	165	10/5/2	VME	AS/OR	gauss
7	09/20/05	174	2/4/4	VME	AS/OR	gauss
8	04/01/06	280	3/6/2	multiplicity	AS/OR	gauss
9		452		multiplicity	AS/OR	gauss

Table 2.1: Milagro epochs: note epoch 9 began with the advent of a new gamma hadron separator. COM is using eq. 2.2 as the core-finder.

2.6 Detector Variations

In addition to changes between epochs, the other major variations in Milagro were seasonal and weather-related variations. These included:

- Daily and seasonal atmospheric changes, including day-night effects. This changes the atmospheric overburden, effectively changing the atmospheric part of the calorimeter.

- Water, ice and snow on the cover, or ice under the cover. These all have various effects of changing the effective water level of the detector and can alter the energy threshold. Particles will produce Cerenkov light above the pond when there is water, snow and ice on the cover which will not be detected. In the case of ice under the cover the refractive index changes will alter the Cerenkov light's path through the pond.

- Air under the cover. After performing repairs, for a few days afterwards, until the weight of the cover again put it into contact with the pond there was air under the cover. The cover-water optical boundary is less reflective than the cover air boundary, so there was a significant increase of amount of light in the pond, hence an increased trigger rate for this short period. However, in Monte Carlo simulations of the detector (see sec. 3.6) the detector is best modeled with no air under the cover.

Chapter 3

Data Analysis Techniques

Once we have been able to reconstruct the primary directions of incident cosmic rays with Milagro, as described in the previous chapter, we can use this data to find signals from astrophysical sources. The coordinate systems that describe the directions of these primaries in cosmic-ray astrophysics are described in sec. 3.1. We wish to find the deficit of events from the signal region, which is a local sink near the Moon or the Sun. The detection of cosmic rays is not uniform in space and time so in order to see the deficit of events from the local direction of the Moon or Sun we must perform an estimate of background and subtract this from the signal. In section 3.2 we describe the method of estimating background and map-making with Milagro data. Once we have established how to estimate the background and subtracted it from the signal we must find the significance of any signal. This is described in sec. 3.3. The parameters that are used for evaluating and cutting Milagro data are described also, the quality cuts on data that are stable between epochs in sec. 3.4 and FRASOR, the Milagro energy parameter, in

sec. 3.5. Finally, in section 3.6 is a description of the Milagro simulated data sets that were used in the calibration of the Milagro detector. In this thesis they are used, in chapter 7, to desribe Milagro's effective area and point spread function in cosmic rays.

3.1 Celestial Coordinates

A celestial coordinate system is a projection on the imaginary celestial sphere that is centered on the Earth. There are several systems that differ based on their choice of poles (and hence equator) and may be stationary with respect to the distant stars, the Earth or other celestial objects of interest.

3.1.1 Local Coordinates

Local Celestial Coordinates are defined with respect to a particular point of interest on Earth; in this case the position of the Milagro detector. This coordinate system co-rotates with the Earth and is described by the altitude (zenith angle) and azimuth coordinates. An object directly overhead (at zenith), has an altitude of 0° and at this point all azimuthal angles are equivalent. The great sphere passing over the zenith and the poles is defined as 0° azimuth. For non-zero altitude, lines of constant altitude are concentric circles centered on zenith. The lines of constant azimuth are great circles. Further, the system is divided into two hemispheres. The visible hemisphere is above the horizon (the plane perpendicular to the zenith direction) and the non-visible hemisphere is below the horizon. This coordinate system is analogous to latitude and longitude on on maps of the globe, but with

the North pole at the position of Milagro.

3.1.2 Equatorial Coordinates

Equatorial coordinates are fixed with respect to the distant stars. The poles are the projections on the celestial sphere of the North and South poles of the Earth (the axis of rotation). The celestial equator is the projection of the Earth's equator onto the celestial sphere. Due to the slow movements over time of celestial bodies, particularly the precession of the Earth and the proper motion of nearby stars, an epoch is defined in which coordinates are measured. The current epoch is J2000 which is the positions of celestial bodies with respect to Earth at noon on January 1st 2000. The J refers to time measured in Julian date in which a year is 365.25 days and each day is 24 hours or 86,400 seconds.

The coordinates used are right ascension (RA/α–analogous to longitude) measured with respect to the vernal equinox of 2000 and declination (dec/δ–analogous to latitude) measured with respect to the north celestial pole, illustrated in fig. 3.1.

There is also a local coordinate system, a system that rotates with the Earth, which is of use with astronomical coordinates. In this system declination is unchanged, but RA is replaced by hour-angle (HA), which is related to RA by

$$\mathrm{HA} = \mathrm{LST} - \alpha \tag{3.1}$$

where LST is the local sidereal time, which measures the rotation of the Earth relative to the distant stars. In this coordinate system an object passing overhead will have a constant RA and dec, but its hour-angle varies.

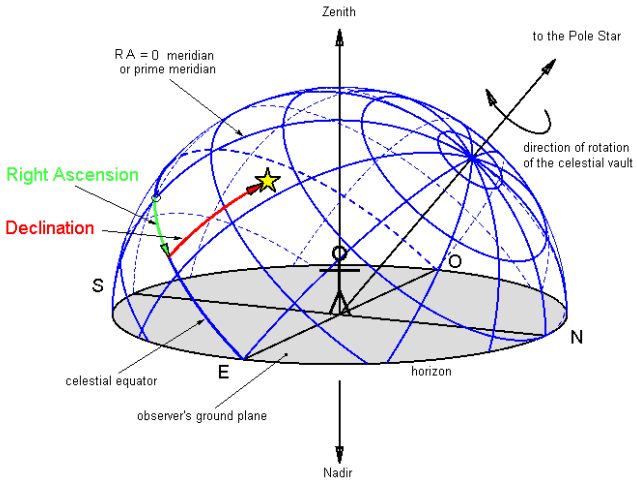

Figure 3.1: The celestial coordinate system with right ascension (RA/α) and declination (dec/δ), from [21].

3.2 Background Estimation with Milagro Direct Integration (MDI)

We now have event times and directions, and a coordinate system to map them in. In the search for astrophysical sources with a detector one cannot simply look at a signal map to find them –typical sources have signals that are smaller than fluctuations in the signal and the acceptance rate of ground-based detectors such as Milagro is strongly dependent on zenith angle and is not uniform in time. Therefore, a background estimate is needed for each point on the sky. Only then one may search for a source by looking at signal minus background in each bin.

As Milagro is a stationary detector, the sky passes overhead. Therefore, points on the sky with the same declination but earlier hour angle, will, at a later time,

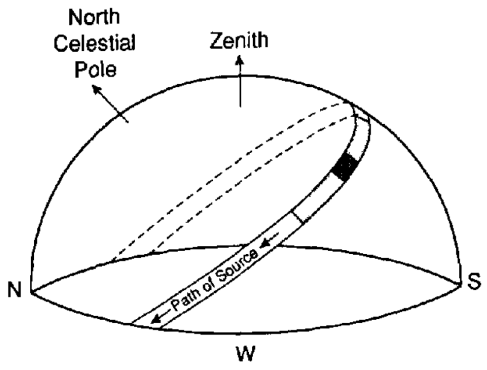

Figure 3.2: Path of a source moving across the sky, from [22].

be at the same local coordinates. A sketch of a source moving across the sky is shown in fig. 3.2. If there is no signal present, points with the same declination but similar HA will contain a similar number of events. This is the principle of background estimation –that signal maps for earlier and later times with the same declination are used as an estimate for the background at the present moment. Over time there is variability in trigger rate, due changes in the atmosphere. If the same band of declination is observed over a long period there will be large variations in the number of events observed.

Correct estimation of the background is crucial. If the background is overestimated a sink will be seen as too large and if the background is underestimated a sink may remain undetected. Typically, we search for sources rather than sinks, so this logic becomes reversed.

We build skymaps in $0.1^\circ \times 0.1^\circ$ bins in equatorial coordinates. The number of

background events in an (α, δ) bin from Milagro Direct Integration (MDI) is:

$$N(\alpha, \delta) = \iint \mathrm{Eff}(\mathrm{HA}(t), \delta)\, \mathrm{R}(t)\, \epsilon(\mathrm{HA}(t), \delta, t)\, \mathrm{d}t\, d\Omega \tag{3.2}$$

where Eff is the efficiency in hour angle and declination. It is found by counting all events appearing in each (HA, δ) bin for that integration period divided by the total number of events in that integration period. It is the probability that an event is in the solid angle bin $\mathrm{d}\Omega$. The event rate over a 24s period is $\mathrm{R}(t)$. This period is just less than the time it takes for the Earth to rotate 0.1°. The ϵ factor is to pick the correct background bin, if an event falls into an (α, δ) bin in sidereal time t then ϵ=1, otherwise ϵ=0.

After each integration period the efficiency map in local equatorial coordinates is converted into a sky map in equatorial (α, δ) coordinates, by multiplication by the event rate $\mathrm{R}(t)$. The integration period here is chosen to be two hours, which maximizes the number of events used to estimate background, whilst keeping the rate fluctuations small due to atmospheric and other time-related phenomena.

3.2.1 Region of Interest (ROI)

The Moon is a known event sink. Therefore, it needs to be excluded from the background estimate. As the Moon is tracked across the sky, a region of interest is set around the Moon and is reset to the new position of the Moon at the end of every integration period. When added to the background map, the events are then weighted by a factor of $\mathrm{ROI}_{all}/\mathrm{ROI}_{off}$, where ROI_{all} is all the events that appear for that integration period, and ROI_{off} are events outside the region of interest for that integration period.

3.3 Significance of a Measurement

Typically, in cosmic ray and γ-ray astronomy we are searching for unknown sources. In searching for a source we have some time collecting cosmic rays from the source direction, and some time collecting cosmic rays from the background. If this is the case we should include our signal in our estimate of the background, otherwise we overestimate the significance of the signal. This is the approach taken by Li and Ma [23]. The significance is given by:

$$S(N_{on}, N_{off}) = \sqrt{2}\left[N_{on}\log\left[\left(\frac{(1.+\alpha)}{\alpha}\right)\left(\frac{N_{on}}{(N_{on}+N_{off}/\alpha)}\right)\right] + N_{off}/\alpha\log\left[(1+\alpha)\frac{N_{off}/\alpha}{(N_{on}+N_{off}/\alpha)}\right]\right]^{1/2} \tag{3.3}$$

Where N_{on} is the number of signal counts in a bin, N_{off} is the background estimate for that bin and α is defined by the ratio of the time spent on-source to the time spent off-source –that is the time spent to accumulate the background.

However, in this thesis we are concerned with the Moon and Sun which are known sinks for cosmic rays. The ROI exclusion as part of the Milagro Direct Integration technique accounts for this.

3.3.1 Maximizing Significance with Boxcar Smoothing

Milagro maps are made in $0.1^\circ \times 0.1^\circ$ size bins, which is considerably smaller than the angular resolution of Milagro. The significance of a measurement is maximized by optimizing signal/$\sqrt{\text{background}}$, which corresponds to a larger circular bin of width $1.58\times$ the average point spread function width, or a 2.1° diameter. However, it is computationally more straightforward to use a square bin of approximately

equal area, with width 2.1°. This is hereafter referred to as boxcar smoothing, and significance maps are smoothed over an area of this size.

3.4 Stable Data Cuts between Epochs

Milagro has very distinct epochs of data collection, as described in sec. 2.5. When making quality cuts on the data, the meaning of these cuts may change from epoch to epoch. It is important to have parameters that can be applied across epochs. It should be noted that raw data is kept for only a few regions of the sky, so improvements such as the trigger mechanism and direction reconstruction algorithm cannot be applied retroactively to old data.

One useful quality parameter in Milagro data is N_{fit}, which is the number of PMTs used in the final stage of the direction reconstruction algorithm. Epochs 7-9, which concern us the most in this thesis, are relatively stable and there is little variation between them. In epoch 6 there were a large number of dead PMTs in the AS layer, which changed the effective N_{fit} cuts. Not until epoch 4 did Milagro have the full array of outriggers online, which also greatly impacted the effective N_{fit}.

To counter these stability effects for N_{fit} a 2-layer equivalent is defined, which is N_{fit} where only the AS and MU layers were available. For this thesis, when N_{fit} is referred to the parameter actually being described is the N_{fit} 2-layer equivalent.

3.5 The Milagro Energy Parameter

In an air shower array such as Milagro, the detector-atmosphere system behaves as a calorimeter, where a small fraction of the EAS reaches ground level. As a result, energies of individual EAS are hard to estimate. More energetic showers contain more particles, cover a larger area, and so will fire more PMTs. Tested extensively from Monte Carlo simulations of the detector response with energy, we have the FRASOR (or FRaction AS-layer OR-layer) parameter, which is correlated with energy. FRASOR is given by the fraction of AS-layer PMTs hit, plus the fraction of OR PMTs hit, so ranges from 0-2.

$$\text{FRASOR} = \frac{\text{\# AS PMTs hit}}{\text{\# live AS PMTs}} + \frac{\text{\# OR layer PMTs hit}}{\text{\# live OR PMTs}} \tag{3.4}$$

The parameter uses the number of hit PMTs rather than hit-size, as the hit-size is subject to large fluctuations as described in sec. 2.4.4, so is a better measure of shower energy. FRASOR is typically put into ten bins. The lowest 0.0<FRASOR<0.2 bin is poorly modeled, as it is particularly sensitive to instability in the energy threshold from weather variations, so is therefore ignored in most analyses. The very highest bins are also often ignored as they suffer from low statistics, and can also trigger the detector from far off the pond, which leads to poor angular reconstruction.

3.6 Milago Simulated Data

Clearly there are no TeV sources that we can control to calibrate the Milagro detector, or use to generate simulated data commonly referred to as Monte Carlo

methods. To do so we can simulate the EAS, using CORSIKA software [24] and the detector response, using GEANT4 [25]. This can describe many aspects of the detector, including the angular resolution and effective area.

CORSIKA (COsmic Ray SImulations for KAscade) takes a primary particle species at a given energy and propagates it in a particular direction. The particle is propagated through an atmosphere with the same composition as Earth's, thrown with a spectrum $dE/dN=E^{-2}$. The high-energy hadronic interaction model is QGSJet-II, whereas for low energies (<80 GeV) FLUKA v2005.6 was used.

GEANT4 (GEometry ANd Tracking 4) inputs the particles in a virtual Milagro detector, designed to recreate the detector response. The output of CORSIKA—the particles from showers that reach the ground—is the input of GEANT4. GEANT4 simulates all particle interactions that produce Cerenkov light in water. For each PMT GEANT4 outputs the number of Cerenkov photons, their arrival time and their detection direction on the photocathode as shown in fig. 3.3, which is needed as the QE of the PMT is a function of where the PMT is hit.

3.6.1 Calibration of Milagro Using Simulated Data

The simulated data are used in calibration tests, such as the choice of optimal pond depth, the effect of ice and air under the cover and designing good reconstruction algorithms. Also the simulated data are used to define the energy scale of the detector, by describing the effective area as a function of energy and zenith angle, which is described in detail in chapter 7.

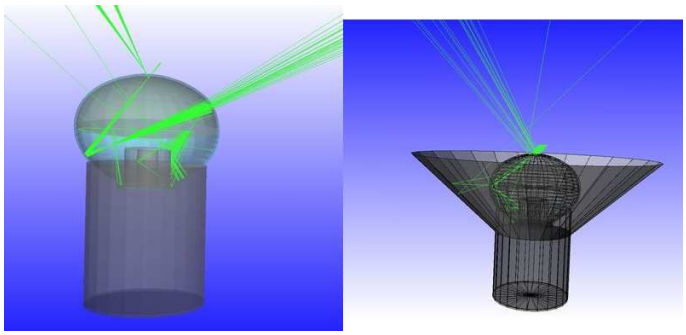

Figure 3.3: Simulation image of Cerenkov photons hitting PMTs with and without a baffle, courtesy of Vlasios Vasileiou.

3.6.2 Data Files

From the CORSIKA and GEANT4 simulations, we produce many Milagro simulated events; for instance 600,000 proton events that triggered the detector for epoch 9. In order to have a concentration of events close to the pond, CORSIKA showers are actually thrown linearly with distance, as opposed to an R^2 distribution, from the center of the Milagro pond, over an area of 1000 m. The events, when analyzed, are then reweighted by the true (rather than reconstructed) distance of the event from the center of the pond [26]. A huge number of events thrown do not trigger Milagro, approximately 50 for every triggered event. To account for these, each event is randomly assigned a weight of zero or 50, which can be used in calculating the effective area, where the total number of thrown events are needed. To improve the statistics for high energy events, the showers are thrown with unphysical spectra indicies of -2.0. Events can then be re-weighted by energy to produce more realistic spectra [26].

Chapter 4

Antiprotons and their Moon Shadow in TeV Cosmic Rays

As cosmic rays propagate through the galactic magnetic field they collide with the interstellar gas and dust, and as a result produce antiprotons. Therefore, there is a natural component of antiprotons in the cosmic-ray flux incident on Earth. One method of detecting this antiproton component is using the antiproton shadow of the Moon. The cosmic-ray particle shadow of the Moon was proposed by Clark in 1957 [27] and first observed by the Cygnus experiment in 1991 [28]. Some cosmic rays will hit the Moon on their path to Earth and so will be missing from the signal. In other words, for VHE CR the Moon is a sink on the sky. At TeV energies, cosmic rays will be deflected on the order of a degree by the geomagnetic field, so the particle shadow of the Moon is deflected to the west of the nominal Moon position. An antiproton shadow would be deflected to the east, as oppositely charged particles are deflected in opposite directions by magnetic fields.

Measurements of the antiproton flux are of great interest, as deviations from the expected TeV flux due to collisions (spallation) would lead to new physics, such antiproton production from dark matter annihilation in the galactic halo or the existence of large-scale antimatter structures.

Section 4.1 of this chapter outlines the expected flux of antiprotons at Earth as predicted by spallation (collisions), including a discussion of cosmic-ray propagation models. The deviation from secondary flux is described in section 4.2. In section 4.3 we describe the Moon shadow in cosmic rays and its applications. This section also contains recent observations and $\bar{p}/p$ flux upper limits from searches for the antiproton shadow. Finally, in section 4.4, we describe other antiproton observations and expectations of the antiproton flux at TeV energies.

4.1 Secondary Antiprotons from Spallation

Whatever their origin, the propagation of cosmic rays through the galactic magnetic field and can be modeled by diffusion. The cosmic rays bounce off Alfvén waves, which are magnetic irregularities in the field moving at galactic wind velocity V=100 km s^{-1}. As the particles propagate, they experience diffusive reacceleration from the Alfvén waves and lose energy via ionization as well as adiabatic and coulomb losses. Cosmic-ray diffusion has been modeled by GALPROP [29] and a second group [30]. The GALPROP propagation equation is:

$$\begin{aligned}\frac{\partial\psi(\vec{r},p,t)}{\partial t} &= q(\vec{r},p,t) + \vec{\nabla}\cdot(D_{xx}\vec{\nabla}\psi - \vec{V}\psi) \\ &= \frac{\partial}{\partial p}p^2 D_{pp}\frac{\partial}{\partial p}\frac{1}{p}\psi - \frac{\partial}{\partial p}\left[\dot{p}\psi - \frac{p}{3}(\vec{\nabla}\cdot\vec{V})\psi\right] - \frac{1}{\tau_{frag}}\psi - \frac{1}{\tau_{rad}}\psi \qquad (4.1)\end{aligned}$$

where $\psi(\vec{r}, p, t)$ is the cosmic-ray density per unit of total particle momentum $\vec{p}$ at position $\vec{r}$. The spatial diffusion coefficient is given by D, the $\nabla \cdot V$ term describes convection, the D_{pp} term describes reacceleration and is related to the spatial diffusion coefficient by $D_{pp}D \ \alpha \ p^2$. The momentum gain and loss is given by $\dot{p}$. The source term is given by q which includes creation, decay and annihilation by spallation. Finally, τ_{frag} and τ_{rad} are the characteristic times of fragmentation and radioactive decay, respectively.

The equation is solved at steady state by approximating the geometry of the galaxy as a thin disc in which particle creation and annihilation takes place, and a larger cylinder over which the particles can diffuse. The parameters of the model are fixed by reproduction of the B/C ratio in cosmic rays and other secondary/primary ratios measured at Earth.

We can describe the diffusion coefficient D, in terms of the particle rigidity R (momentum/charge):

$$D = D_0(v/c)R^{-\delta} \tag{4.2}$$

where δ is some spectral index arising from scattering from the random magnetic boundaries during particle propagation. This equation predicts that particles of a higher rigidity are more likely to escape the galaxy.

Antiprotons occur naturally in these models. The overwhelming majority of antiproton creation occurs when a primary cosmic-ray proton collides with a hydrogen atom in the ISM, with a smaller but significant contribution from cosmic-ray protons colliding with ISM helium. As products of spallation antiprotons have an energy spectrum which behaves like (secondary flux)/(primary flux)$\sim$ $\mathrm{E}^{-\delta}$. With

a typical δ-value of 0.6, and assuming interaction cross-sections scale with energy, a crude estimate of the $\bar{p}/p$ ratio at 1 TeV is 10^{-5} to 10^{-4} from purely secondary $\bar{p}$ production.

4.2 Other Sources of Antiprotons in Cosmic Rays

Other than the secondary contributions from collisions in the flux of antiprotons at Earth, there are several possible theories that add to the flux. These arise from both astrophysical explanations and beyond the standard model physics. Ruling out the contributions from evaporation of primordial black holes—which would only give a significant contribution to the flux at GeV energies [31]—there are two main potential primary antiproton sources at TeV from exotic contributions and also a proposed primary astrophysical $\bar{p}$ flux source.

4.2.1 Anti-Helium

Little contribution is expected from anti-elements heavier than antiprotons. From what we know of the composition of the ISM and cosmic-ray propagation, for our purposes we may assume that the entire cosmic-ray antiparticle flux on Earth is composed of antiprotons. At GeV energies, where antiprotons have been detected, AMS found an upper limit of the anti-helium/helium ratio of 10^{-6} [32], confirming the lack of anti-helium in cosmic rays.

4.2.2 Old Supernova Remnants

Motivated by PAMELA's observed excess in positrons [33], models have been suggested that positrons produced and accelerated in pulsar magnetospheres provide an astrophysical explanation for this excess [34], which would leave the antiproton flux unchanged. Blasi and Serpico, proposed a model [35] where positrons are produced before acceleration in old supernova remnants, and then accelerated with the other cosmic rays. As the mechanism is now hadronic, this model also predicts an increase in the $\bar{p}/p$ ratio at multi-GeV energies, and a $\bar{p}/p$ ratio of $4.5{\times}10^{-4}$ at 1 TeV, which is a considerable enhancement above their background estimate at this energy of about $3{\times}\ 10-5$.

4.2.3 Extra-Galactic Antimatter

The observed particle-antiparticle asymmetry in the universe has been a matter of debate for decades. Anti-galaxies—galaxies composed entirely of antiparticles—would add a significant component to the flux of $\bar{p}$ at TeV energies. The proton component of cosmic rays would remain galactic but the antiprotons would receive a significant contribution from extra-galactic sources. Assuming a standard cosmic-ray propagation model, the mean lifetime of a cosmic ray in the galaxy behaves as $\mathrm{E}^{-\delta}$. So the $\bar{p}/p$ ratio would increase with energy by E^{δ}, as the protons from mostly galactic sources leave the galaxy –whereas the antiprotons are mostly from extra-galactic sources that overcame the galactic wind to enter our galaxy. A model of such primary sources of $\bar{p}$ is described in [36], and see also the review [37] and the references therein.

4.2.4 WIMP Dark Matter Annihilation

The matter content of the universe has long been known to be composed mostly of non-baryonic components, known as dark matter (DM). Determining the nature of DM is one of the principal goals of physics at the beginning of the 21st century. Weakly Interacting Massive Particles (WIMPs) are a premier candidate for DM. Their annihilation in the Milky Way galactic halo would produce antiprotons, adding a primary component to the TeV antiproton flux.

WIMPS from supersymmetry

The supersymmetric extension to the standard model provides an ideal WIMP candidate in neutralinos –which are combinations of super-partners of the Higgs and gauge bosons. These are proposed as the lightest supersymmetric particle and in annihilations could produce antiprotons.

In [38] an improvement of the secondary calculation of [30] is presented along with a scenario where the WIMPs annihilate to a W^+W^- pair, based on the 2009 PAMELA data [39]. Other models are provided in [40; 41], including a heavy 10 TeV WIMP which enhances the antiproton flux considerably at TeV –at 1 TeV the $\bar{p}/p$ ratio from this WIMP annihilation is modeled to be $7{\times}10^{-3}$.

WIMPS from Kaluza Klein particles

The lightest Kaluza Klein particles [42; 43; 44] are from models with compactified universal extra dimensions and are also candidates for the lightest supersymmetric particle. They are WIMP DM candidates and their annihilation would add to the

$\bar{p}$ flux. These models are examined in [41].

4.3 The Particle Moon Shadow

The cosmic-ray Moon shadow has been observed by AS arrays [28; 45; 46], neutrino detectors [47] and muon detectors [48; 49; 50; 51; 52].

As the position of the cosmic-ray Moon shadow depends upon the paths of the particles through the geomagnetic field, the position of the shadow is energy-dependent. The Earth-Moon system can be considered as a spectrometer; particles with a higher magnetic rigidity will be deflected less than particles of a lower rigidity.

Cosmic rays of 10 TeV are barely deflected and any shadow observed generated from particles at this energy would be centered on the Moon's nominal position. At very low energies particles may not be able to penetrate the geomagnetic field. The exact cutoff depends on the zenith angle –so the relative position of the Moon and Milagro. At the TeV energies that concern us in the thesis, the particles are deflected on the order of a degree.

4.3.1 Geomagnetic Field Models

The deflection of a cosmic ray on its path to earth depends on its rigidity and the magnetic field it traverses. The geomagnetic field is most simply approximated by a dipole, with the South pole close to Earth's geographic North pole. Choosing a coordinate system so the z-axis is along the dipole axis, the B-field is given in

cartesian coordinate by:

$$B_x = \frac{3Mxz}{r^5}$$
$$B_y = \frac{3Myz}{r^5}$$
$$B_z = \frac{M\left(3z^2 - r^2\right)}{r^5} \tag{4.3}$$

where M is the dipole strength, $8.1{\times}10^{15}$ Tm^3, and the North pole is modeled at 79.54° S, 108.43° E.

Earth's true field, close to the surface, can be expanded in terms of harmonic coefficients, given by the International Geomagnetic Reference Field (IGRF) [53]. These are calculated in the geocentric, geographic, coordinate system. As the field changes slowly with time, the model coefficients are published every five years and the coefficients can be calculated at any intermediate time by linear interpolation. The magnetic field on Earth's surface calculated with this model is shown in fig. 4.1. This model is computationally intensive, therefore, in a Monte Carlo simulation of the Moon shadow in chapter 7, we adopt the dipole model of the geomagnetic field.

More sophisticated models are available for modeling the field accurately as far out as the current sheet. At this point the Earth's field, known as the magnetosphere, is buffeted by the solar wind which makes the model highly time-dependent. One such model is the Tsyganenko model [54], shown in fig. 4.2. The real magnetosphere extends on average 12 $R_\oplus$ sunwards with the tail extending to 100-200 $R_\oplus$ in the opposite direction and 20-25 $R_\oplus$ perpendicular to the Earth-Sun direction. However at distances of 10-20 $R_\oplus$ the field strength is approximately nT and the gyroradius of a 1 TeV proton is $\sim$20 AU, whereas close to the Earth's surface,

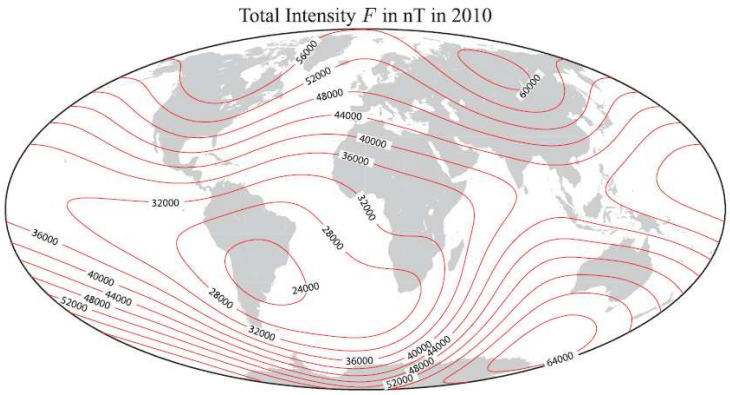

Figure 4.1: The 2010 IGRF field magnitude at the surface of the Earth, taken from [53].

where the field is ∼0.5 G, the gyroradius is approximately 10 $R_{\oplus}$. For reference, the Moon sits at ∼60 $R_{\oplus}$. Therefore at TeV energies the structure of this part of the field is not important.

It should be noted that the Moon is slightly magnetic and has its own field, but is so weak it can be ignored here.

4.3.2 Absolute Pointing Direction

The accuracy of the Milagro pointing direction was established using the Crab Nebula, a supernova with a pulsar wind nebula, which is used as a standard astrophysical source. Any Milagro pointing error would come from timing biases in the PMTs from either slewing, the time the signal takes to pass through the electronics or the locations of the PMTs themselves used in reconstruction. An epoch by epoch analysis was performed using the position of the Crab nebula. No

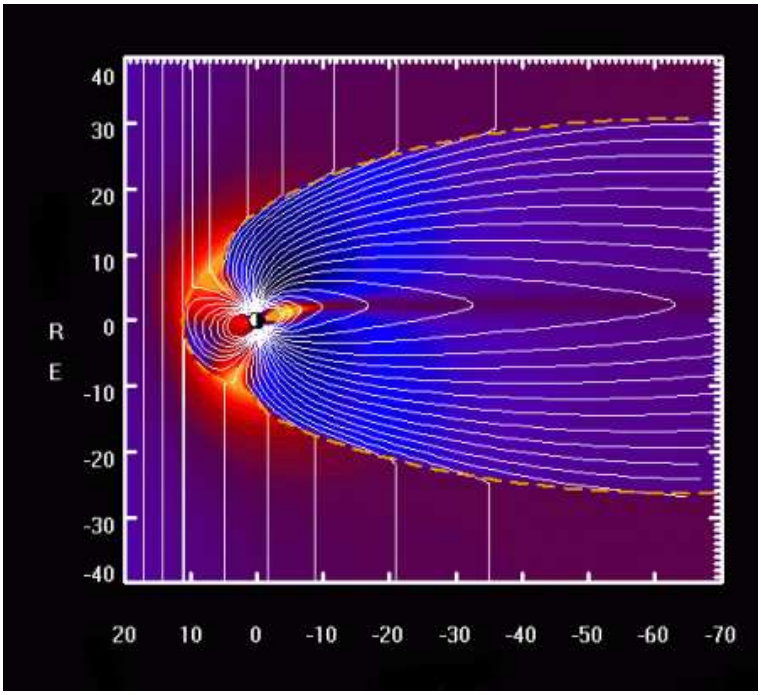

Figure 4.2: A slice of the magnetosphere, as buffeted by the solar wind; in a map with distance units of the radius of the Earth R_E. The solar wind flows from left to right, buffeting the magnetosphere and dragging it out with a long tail. Taken from [55].

pointing error was found. Two other sources seen by Milagro, Mrk 421 and MGRO J1908+06 were used as a check and no error in the pointing accuracy was found. That is, the zenith alignment of Milagro is accurate to 0.1° or less.

This has two implications for the Moon shadow. The first is that we are looking in the right place when referring to the nominal position of the Moon. The second is that the Moon shadow could be used as a further check on the pointing direction of Milagro. This could be accomplished using high energy Moon shadows, that do not undergo a large deflection due to the geomagnetic field. To look at high energy Moon shadows one would look at high FRASOR bins (the Milagro energy parameter) and compare the position to the Moon Monte Carlo shadow position. That analysis is not performed in this thesis. Instead we look at lower energy particles to see how sensitive the shadow position is to the Milagro energy scale.

4.3.3 Point Spread Function

The Milagro point spread function (PSF), a measure of the angular resolution, has been well studied for γ-rays. A full description of the Milagro PSF in cosmic rays is given in sec. 7.5. Agreement between the shapes of the Moon shadow in data and in Monte Carlo can be seen as a confirmation of the Milagro PSF in cosmic rays. However, a detailed analysis of the cosmic-ray PSF using the Moon shadow is not performed in this thesis, and is instead determined from simulations of the detector response to hadron-initiated EAS. The PSF is instead used in the energy calibration analysis of chapter 8.

4.3.4 Energy Calibration

The Earth-Moon system is a spectrometer for cosmic rays. The deflection of a particles is dependent on its rigidity, so, for a given charge, particles of lower energies will be deflected more than those with higher energies. Therefore, the position of the Moon shadow is energy-dependent and it may be possible to calibrate the energy scale of the detector using the shadow. This is the basis of chapter 8.

4.3.5 The γ-ray Moon Shadow

The Moon also casts a shadow in γ-rays, which appears at the nominal Moon position, smeared out by the Milagro point spread function. However γ-rays appear as approximately 10^{-4} of Milagro triggers. Whilst it is possible to use Milagro γ-hadron separation to cut out large amounts of cosmic rays the reverse is not true, and attempting to cut out γ-rays would cut large amounts of cosmic rays from data. If we were able to see the antiproton shadow at the 10^{-4}-10^{-3} level then the γ-ray Moon shadow would become important. Here, however, this is not the case, so the γ-ray Moon shadow is not considered further.

4.3.6 Previous Observations

As mentioned in the introduction, the Moon shadow has been observed by many previous experiments. A full list of these is shown in table. 4.1, along with observed antiproton/proton ratio upper limits, the significance of the shadow observation and the approximate energy.

Table 4.1: A summary of notable experiments that have observed the Moon Shadow; with particle type, shadow depth in σ and approximate energy, as well as antiproton limit.

Experiment	Type	depth (σ)	energy	$\bar{p}$/p limit
Tibet ASγ [45]	array	43	3 TeV	0.07 90% CL
IceCube [47]	neutrino	5	TeV	
L3+C [48]	muon	9.4		0.11 90% CL
MACRO [49]	muon	6.5	TeV	0.52 68% CL
Soudan 2 [50]	muon	5	TeV	
Cygnus [28]	proton	4.9	20 TeV	
CASA [46]	proton	4.7	100 TeV	
Bust [51]	muon	3		
ARGO-YBJ[56]	array	22	1.4 TeV	0.05 90% CL
			5 TeV	0.06 90% CL
HEGRA[57]	array		50 TeV	
GRAPES-3[58]	array	5		
MINOS[52]	muon			

4.4 Antiproton Observations

There has been a large amount of recent interest in antiproton flux measurements in cosmic rays, since PAMELA found an excess in positrons, whilst finding no excess in antiprotons, at GeV energies [33]. This result challenged propagation models of cosmic rays at these energies and raises the possibility of new physics, particularly in finding DM models which produce positrons but not large amounts of antiprotons. Excesses in $\bar{p}$ flux above those expected from secondary antiprotons could be explained by dark matter in the galactic halo, or anti-galaxies, or some other exotic idea yet to be discovered.

It is therefore of great interest to establish the flux of antiprotons in the TeV region of the spectrum. The $\bar{p}/p$ parameter space is shown in fig. 4.3. As can be seen from the figure there is a wealth of models and data in the GeV region, with many detections of antiprotons in cosmic rays, and the highest detection from PAMELA at 180 GeV [59]. In the next few years, assuming AMS-02 achieves its expected sensitivity [60], these measurements will be extended to the TeV region. Today, however, the TeV region is more barren, with a few scattered data points, and the best constraints on the $\bar{p}/p$ ratio come from Moon shadow studies with arrays.

4.4.1 Satellite Observations from PAMELA

PAMELA –a Payload for Antimatter Matter Exploration and Lightnuclei Astrophysics, is a satellite experiment, which has been operational since July 2006. Designed for detection of all cosmic-ray species, it contains a magnetic spectrometer

with silicon tracker planes, an electromagnetic imaging calorimeter, a shower tail catcher scintillator. It also contains an anticoincidence system which is used to reject particles which do not pass cleanly through the acceptance of the spectrometer. The spectrometer with tracker plates behaves much like the Milagro-atmosphere system, but with all energy of particles deposited in the calorimeter.

Of interest to this thesis is that PAMELA has been able to extend the detection energy of antiprotons in cosmic rays up to 180 GeV, fueling a new generation of models for VHE antiproton flux.

4.4.2 Balloon Experiments

Balloon experiments such as CAPRICE, BESS, HEAT and the SMS operate similar detection techniques to PAMELA; some kind of scintillator (or other system to produce Cerenkov light such as a pure gas) to track particles and a calorimeter to measure energy. The experiments are sent to high enough altitudes where they can detect primary particles.

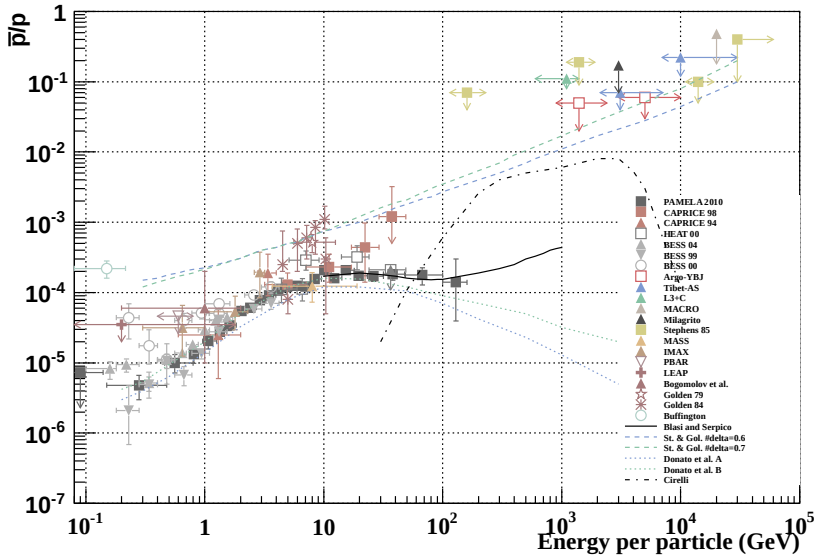

Figure 4.3: $\bar{p}/p$ ratios from various experiments and models. Wino DM annihilation plus secondary $\bar{p}$ from Donato et al, where the B and A curves are the upper and lower limits of the model respectively [38], antiprotons from secondary plus old SNR from Blasi and Serpico, [35], anti-galaxy contributions from Stephens and Golden with δ=0.6 and 0.7, [37], WIMP DM from Cirelli et al.[40], and data from PAMELA [59], Bess[61; 62],Caprice [63; 64], Heat [65], Tibet-ASγ[45], ARGO-YBJ [66], MASS[67], IMAX [68], PBAR, [69], LEAP [70], Bogomolov et al. [71], Golden [72; 73], Buffington et al. [74].

Chapter 5

The Heliospheric Magnetic Field

This chapter discusses the heliospheric magnetic field and how it influences the Sun's shadow in cosmic rays, specifically during cycle 23 and paying particular attention to solar minimum. Also in this chapter is a brief description of previous observations of the Sun's shadow in cosmic rays, in section 5.6. The Sun's shadow in cosmic rays, like the Moon's, is deflected by the geomagnetic field. Unlike the Moon, however, the Sun has a strong field of its own. In fact, the Sun's magnetic field (hereafter referred to as the HMF) is the dominant magnetic field in the solar system and can deflect VHE CR by a significant amount.

5.1 The Sun's Shadow in VHE CR

Cosmic rays that pass close to the Sun may, or may not, hit it. As the Sun has its own magnetic field, whether a particle hits the Sun (the surface of the photosphere), or not is dependent not only on the energy of the particle and its

incident direction, but the stage of the Sun in its 11-year magnetic cycle. If a particle is able to make it to the surface of the Sun it will give rise to a deficit of particles observed at Earth, or a cosmic-ray Sun shadow.

The density in the corona is many orders of magnitude less than the photosphere so we model the Sun as a solid sphere extending to the photosphere with some magnetic field.

Particles that do not make it to the photosphere are deflected away from the Sun by the HMF. Over the time scale for the particle to traverse the HMF on its way to Earth the magnetic field lines are static. Particles for this field configuration may be deflected away from Milagro –but these do not give rise to a shadow. Liouville's theorem of the conservation of phase-space volume means that for every particle deflected out of the path of Milagro there will be another deflected into the path of Milagro by the magnetic field. Hence, only particles that hit the Sun give rise to a shadow.

5.2 Solar Cycles

There are two main cycles that describe the Sun's behavior. The first is the solar magnetic cycle, which governs the magnetic field of the Sun. The second is the Carrington rotations which is the rotation of the Sun on its own axis.

5.2.1 The Solar Magnetic Cycle

The solar magnetic cycle is the (on-average) 11-year magnetic cycle, during which the magnetic poles of the Sun reverse polarity. The cause of the pole reversal is not

completely understood. The Sun rotates more slowly on its own axis at the poles than at the equator. This differential rotation rate causes magnetic field loops to become twisted, which is thought to be a driving force in the field reversal.

The Hale cycle is known as the full 2×11 year cycle in which the magnetic field flips twice, returning to its original polarity.

5.2.2 The Coronal Field through the Cycle

Close to solar minimum, the coronal field is thought to be mostly dipolar with the magnetic poles closest to the rotational poles in a similar configuration to the Earth.

Closer to maximum the field becomes increasingly multipolar, and the poles at maximum become almost equatorial, before a dramatic pole flip occurs. Coronal holes, which at minimum live at the poles, become larger and are more frequently found towards the equator. Moreover, Coronal Mass Ejections (CMEs) become more common. These fantastic events hugely distort the magnetic field as the solar wind strips a large amount of particles from the corona into the heliosphere. Also at maximum very powerful magnetic flux loops on the surface become more common -in fact, these are the origins of sunspots. Sunspots come in pairs and are the points of connection of these closed ∼kG magnetic loops on the photosphere. Typically the magnetic field on the surface of the Sun is on the order of ∼gauss, so solar activity can totally undermine any attempt at modeling the large-scale magnetic field that does not include these frequent events. Diagrams of the coronal field though the solar cycle are shown in fig. 5.1.

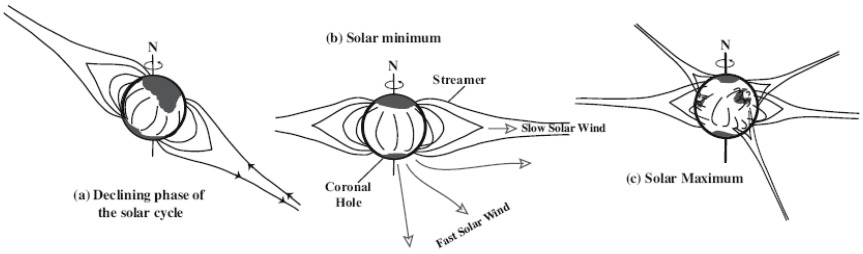

Figure 5.1: The Coronal field through the solar cycle. Taken from [75].

5.2.3 Carrington Rotations

A Carrington rotation is defined as the time the Sun takes to revolve equatorially on its own axis. It is defined synoptically –the rotation rate is that as viewed from Earth and, as the solar rotation rate is dependent on heliographic latitude. A Carrington rotation is about 27 days, but may vary, therefore the Carrington rotation has been standardized to 27.3 days, to allow comparisons between rotations.

5.2.4 Solar Cycle 23

Solar cycle 23 began in 1996 and ended in 2008 (for a detailed review of solar cycle 23 see [76]). At the beginning and end of the magnetic cycle, the Sun is always in the quiet phase. Solar maximum, when the Sun switched magnetic polarities, occurred in 2001 just as Milagro was beginning operation, and cycle 24 began just after Milagro stopped taking data. As with all solar cycles, cycle 23 was not symmetric, the solar maximum was closer to the previous minimum, rather than in the middle of the cycle.

From observations of previous cycles, cycle 23 was expected to be more active than it was, but in most ways was considered a normal cycle. However, the end of cycle 23 (after Milagro stopped taking data) has been an especially quiet period [77].

5.2.5 Sunspots

There are two widely used tracers of solar activity. The sunspot number (SSN) has been recorded since Galileo Galilei made the first observations of sunspots in the seventeenth century. They have shown a clear correlation with the solar cycle, and increase in number at solar maximum. Over many decades of observations, they are observed in their fewest numbers at minimum phase. The so-called butterfly diagram is the other common tracer of solar activity and shows correlation between the number of sunspots appearing at a heliographic latitude with time. The sunspots appear in two bands, above and below the equator, at 30° heliographic latitude at the beginning of each cycle. As the cycle progresses they drift towards the equator but at solar minimum the cycles may overlap, with new bands appearing before the previous cycle's band has disappeared. These are both shown in figure 5.2.

5.3 Space Coordinates

In space physics, which deals with satellites and field models (rather than the various astronomical coordinate systems, which are 2-D projections on a sphere), 3-D coordinates are needed.

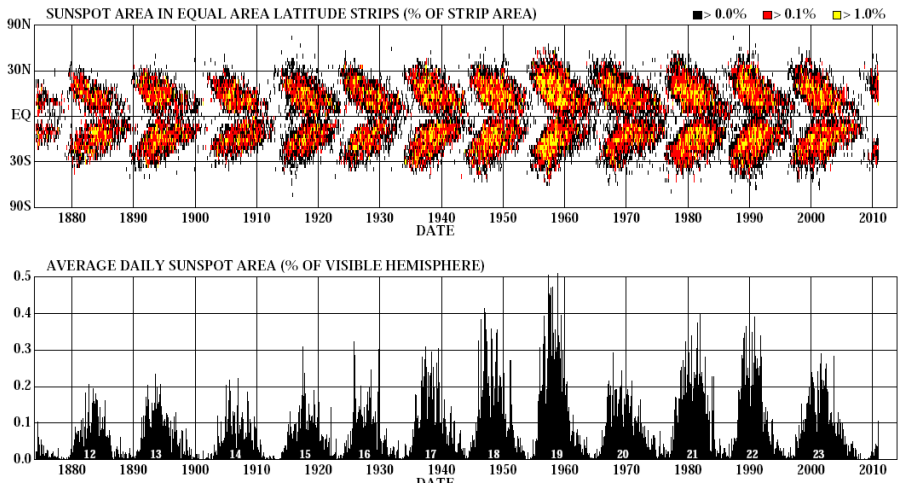

Figure 5.2: Sunspot number and sunspot number by heliographic latitude, from 1880 to 2010. The NOAA sunspot number is compiled by the US National Oceanic and Atmospheric Administration. The numbers are the monthly averages (SSN). Taken from [78].

5.3.1 HEEQ coordinates

Heliocentric Earth EQuatorial (HEEQ) coordinates have the x-axis oriented along the intersection between the solar equator and the the solar central meridian (as seen from Earth) and the z-axis is along the North pole of the Sun's rotation axis.

This system is aligned with the Sun's rotation axis so is a convenient coordinate system in which to describe the Heliospheric Magnetic Field (HMF) –either the Parker Spiral or the Fisk Field. Details of the transformation from HEEQ coordinates to RA and dec are provided in [79].

5.3.2 Carrington Coordinates

Carrington Coordinates are the same as the HEEQ coordinates, except they co-rotate with the Sun as per the Carrington rotation. Therefore they are ideal coordinates for Solar observations. The data from the Wilson Solar Observatory is given in these coordinates.

The relation between Carrington and HEEQ coordinates is best described in a spherical polar coordinate system where the zenith angle azimuthal angle and radius have the usual relations with cartesian coordinates, choosing θ to be zero along the z-axis, and ϕ to be zero along the x-axis.

The relation between ϕ_{Carr} and ϕ_{HEEQ} is:

$$\phi_{Carr} = \phi_{HEEQ} + L_0; \tag{5.1}$$

Where L_0 is some azimuthal angle that rotates with the Sun and can be considered as the helio equivalent of hour angle.

5.4 Heliospheric Magnetic Field

In December 1994, at 94 AU from the Sun, NASA's Voyager 1 crossed the termination shock, the first boundary between the Heliosphere and the Local Interstellar medium. Inside this region, known as the Heliosphere, many of the properties—including the magnetic field—are determined by the Sun.

To explain the structure of the HMF in 1958 Eugene Parker proposed the controversial idea of the solar wind, a supersonic stream of plasma originating in the corona that shoots outwards all the way to the termination shock and beyond.

5.4.1 The Parker Spiral

The solar wind begins in the upper corona—the outer atmosphere of the Sun—and carries with it a hot plasma of particles into the heliosphere. The open magnetic field lines are frozen into the plasma and are dragged into the heliosphere by the solar wind. The solar wind has velocities of tens of km/s, so with the rotation of the Sun the field lines are dragged out from the surface of the Sun in a spiral arrangement. This is known as the Parker Spiral, and is shown out to 1 AU in fig. 5.3. The magnetic field is given by:

$$B_R = B_0 \left(\frac{r_0}{r}\right)^2$$

$$B_\theta = 0$$

$$B_\phi = \left(\frac{B_0 r_0^2}{r V_R}\right) [(\omega - \Omega) \sin\theta]$$

where r_0 is the solar radius, V_R is the velocity of the solar wind, typically $\sim$400 km/s, ω is the rotation rate of the Sun, and Ω is the differential rotation rate of

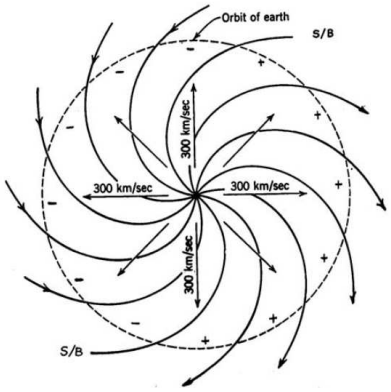

Figure 5.3: The Parker spiral out to 1 AU, note the field is nearly at 45° at the Earth distance. Taken from [80].

the Sun, as measured between the poles and the equator.

5.4.2 The Fisk field

Prior to Ulysses, launched in 1990, the solar magnetic field and the solar wind had never been measured far out of the planetary plane, so the behavior of both were largely unknown at high heliographic latitudes [76]. Ulysses found a faster solar wind at high latitudes and the Parker spiral was found to be inconsistent with these speeds. A new model was proposed by Fisk, that included the high-latitude fast-winds [81]. It reduces to the Parker Spiral when the angle between

the dipole-axis and the rotation axis β=0.

$$
\begin{aligned}
B_R &= B_0 \left(\frac{r_0}{r}\right)^2 \\
B_\theta &= \left(\frac{B_0 r_0^2}{r V_R}\right) \omega \sin\beta \sin\left(\phi + \frac{\Omega r}{V_R} - \phi_0\right) \\
B_\phi &= \left(\frac{B_0 r_0^2}{r V_R}\right) \left[\omega \left(\cos\beta \sin\theta + \sin\beta \cos\theta \left(\phi + \frac{\Omega r}{V_R} - \phi_0\right)\right) - \Omega \sin\theta\right]
\end{aligned} \tag{5.2}
$$

5.5 Coronal Magnetic field

Despite some recent measurements [82], direct measurement of the coronal magnetic field is difficult, due to the low particle density (10^{-9} cm^{-3}) in the corona. To build models of the coronal field two main approaches are taken. In the first, a full magneto-hydrodynamic simulation of the plasma field in this region is performed. However, this is computationally intensive, and is not performed here. The approach we follow is to extrapolate photospheric observations into the corona. With this method it is possible to resolve fine structure, but the time dependence in the model comes from a series of static configurations in which the input parameters are varied with time.

5.5.1 Wilcox Solar Observatory Magnetograms

Daily magnetograms of the photosphere are taken by several experiments. They use stokes vectors from Zeeman splitting of atoms in observations of the photosphere. The Wilcox Solar Observatory (WSO) [83] takes daily magnetograms in terms of a multipolar expansion, in Carrington coordinates [84]. The data is directly published to be used in the Potential Field Source Surface Model, or PFSS.

The observations are made as line-of-sight measurements but from observational evidence the magnetic field is radial at the photosphere, and a correction for this is described in [85]. The WSO provides the magnetogram results with this correction.

5.5.2 The Potential Field Source Surface Model

Surface models were initially developed by [86; 87], and later refined by [88] and [89].

The PFSS model is a multipolar expansion of the coronal magnetic field that is valid between the photosphere and some imaginary surface, known as the source surface, at which point the magnetic field is entirely radial and beyond which there are no open magnetic field loops. The currents in the corona are neglected, to allow unique solutions of the potential in closed form.

The parameters of the model are the Laplace multipolar expansion coefficients and the position of the source surface R_s, which is normally fixed at 2.5 $R_\odot$ but in some models permitted to vary between 2.5-3.25 $R_\odot$.

The concept of the PFSS model is shown in fig. 5.4. Inside the source surface is multipolar field, where closed field loops protrude from the photosphere. All field lines that extend past the source surface are open, and at the surface all field lines are entirely radial. Beyond the source surface, the HMF is then described by either the Parker spiral or a Fisk field. For a full review of the HMF and the coronal field see [76].

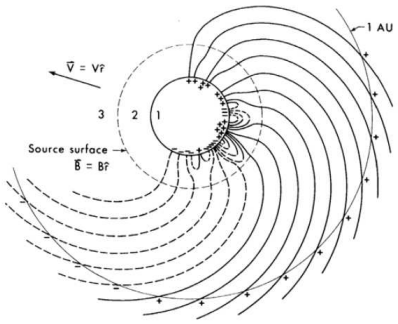

Figure 5.4: The PFSS model. Taken from [87].

5.5.3 The Heliospheric Current Sheet

The Sun's magnetic polarities are separated beyond the source surface by the heliospheric current sheet (HCS). Above and below the current sheet, the magnetic field lines are in opposite directions, if above the HCS they are inwards, then below the HCS they are outwards. For the cosmic rays that navigate these magnetic fields on their way to Earth from the direction of Sun, their deflection direction is governed by which side of the current sheet they are. As the solar rotation axis is not aligned with the magnetic axis, the HCS is not flat in the plane of the solar system. Rather, the HCS takes the form of a "ballerina skirt" as shown in figure 5.5.

The Earth passes though both polarities as the "ballerina skirt" fluctuations rise above and below the Earth's orbital plane. It is therefore possible to look at the solar shadow in VHE CR when the Earth is above and below the HCS, and observe the opposite directions of the shadow deflection caused by the HMF. This was recently performed by the ARBO-B collaboration in [90], but such an analysis

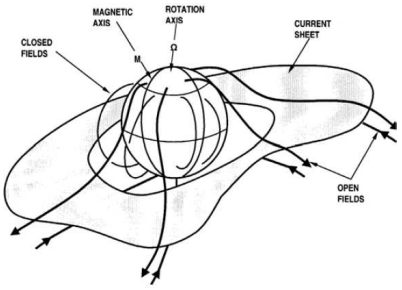

Figure 5.5: The heliospheric current sheet. Taken from [76].

is not performed in this thesis.

5.6 Observations of the Sun's Shadow in Cosmic Rays

Many of the same experiments that have observed the Moon shadow (table 4.1), have observed the solar shadow. A list of these experiments, the significance of the solar shadow observed, and the approximate energy of the observation are given in table 5.1.

Table 5.1: A summary of notable experiments that have observed the Sun Shadow; with particle type and shadow depth in σ as well as approximate energy.

Experiment	Type	depth (σ)	energy
Tibet ASγ [91]	array	5.8	10 TeV
Tibet ASγ[92]	array	12	10 TeV
MACRO [49]	muon	4.6	20 TeV
CASA [46]	proton	4.8	100 TeV
ARGO-B[90]	array	43.6	5 TeV
MINOS[52]	muon		

Chapter 6

Moon and Sun Maps in Data

The Moon and Sun are sinks in VHE CR. The goal of this chapter is to see this deficit of events from the Moon and Sun direction with Milagro. The detection of cosmic rays is not uniform in space and time, so in order to see the deficit of events from the direction of the Moon or Sun, we must perform an estimate of background and subtract this from the signal. In chapter 3, we saw how to take the raw primary direction and event times, as measured by Milagro, and use that to estimate the background, as well as the astronomical coordinate systems in which to do so. In this chapter we use these tools to make maps of the cosmic-ray flux from the directions of the Moon and Sun by making signal minus background skymaps in coordinate systems centered on these bodies. The Milagro data maps for the Moon and Sun in this chapter are made covering epochs 7-9, a period of approximately 2.5 years, from Fall 2005 to the end of Milagro's operation in Spring 2008. In this period 126 million events passed cuts within 5° of the Moon with an average 12600 events/0.1 square degree bin.

6.1 Moon-maps

The Moon-maps are made for all of epochs 7, 8 and 9 covering a period of 907 days from 20th September 2005 to 15th March 2008. The background is estimated using direct integration (MDI) as described in sec. 3.2, with two hours of data before and after source transit used to estimate the background. The maps are recentered on the Moon every 5 minutes. In this time the Moon moves $\sim 0.05^\circ$ in RA and less in dec, so with map bins of extent $0.1^\circ \times 0.1^\circ$ the center of the Moon will remain in the same bin for these 5 minute periods.

6.1.1 Quality Data Cuts and Map Making Parameters

Quality cuts on the data were $N_{fit}>40$ and zenith angle $\theta<60^\circ$, and all maps were made with ROI=3° with 2.1° boxcar smoothing.

N_{fit} Cut

Cuts on N_{fit} are correlated with energy, so low N_{fit} cuts include more lower energy particles. However, N_{fit} also has significant impact on angular resolution, with lower N_{fit} cuts leading to poorer angular resolution. The trade-off between good angular resolution, and keeping as many events as possible leads to the choice of $N_{fit}>40$.

Zenith Angle Cut

Typically, a cut of $\theta<45^\circ$ is used when analyzing Milagro data. A relaxed zenith angle cut of $\theta<60^\circ$ was chosen here as to get as much data from near the Moon as

possible as well as stopping an effect that caused the maps to be cut off approximately 8° below the Moon with tighter zenith cuts.

Region of Interest Background Choice

The Moon is excluded from the background estimation, using the region of interest exclusion (ROI), described in section 3.2. As the Moon is a sink on the sky, if the region of interest does not contain all the shadowed events the background will be slightly overestimated –that is the Moon being a sink for cosmic rays, the background number of events per 0.1 square degree bin is underestimated. The Moon moves $\sim 0.5°$ in one hour and the shadow extends to approximately 3° (see sec. 4.3), so in a two hour integration period a 3° region of interest is the smallest area that can be excluded so the Moon does not effect background estimation. Despite there being a small leakage of the shadow into the background estimation region this has no effect, due to the large integration time of two hours. Choosing a larger or slightly smaller ROI has a negligible effect and is not visible.

Significance Map Smoothing

The significance maps shown in this thesis are boxcar smoothed over an area of 2.1 square degrees, as described in sec. 3.3.1.

6.1.2 Moon Transit

The Moon orbits the Earth in approximately 27.3 days, completing nearly 33 transits for epochs 7-9. For the early Milagro/Milagrito data, the Moon orbit was

between $\pm 18.5^\circ$ but for epoch 7 and beyond the limits are approximately $\pm 28^\circ$ as shown in figure 6.1.

6.1.3 Coordinate System

There are many ways of projecting a sphere onto a plane. The astronomical equatorial system described in section 3.1 is an equal area projection with each ($\alpha \cos\delta$, δ) bin containing an equal area. However, the Moon is a transient source that moves across the sky in RA and dec, so the maps are made in particle minus Moon coordinates with the nominal Moon position at the origin.

In this case, the best choice of coordinates is not obvious. An equal-area type coordinate system of the form $((\alpha_p - \alpha_m)\cos\delta_m,\ \delta_p - \delta_m)$, where p denotes particles and m denotes the Moon, does not actually preserve area as the jacobian is $\cos\delta_m$. Coordinates of the form $(\alpha_p \cos\delta_p - \alpha_m \cos\delta_m,\ \delta_p - \delta_m)$ do preserve area, but do not preserve the relative positions of events with time.

It would seem that the $(\alpha_p \cos\delta_p - \alpha_m \cos\delta_m,\ \delta_p - \delta_m)$ coordinates are the best choice. However, there are additional complications that arise from the MDI background estimate. This coordinate system shifts the data along the negative RA-axis for positive $\delta_p - \delta_m$ and along the positive RA-axis for negative $\delta_p - \delta_m$. This leads to a distorted background using Milagro Direct Integration. There is also an edge effect associated with the ROI source exclusion. For that reason we adopt $(\alpha_p - \alpha_m,\ \delta_p - \delta_m)$ coordinates.

In this coordinate system the background estimate is excellent over the whole sky, as the effect of variable bin-size in the signal map is mimicked exactly in the

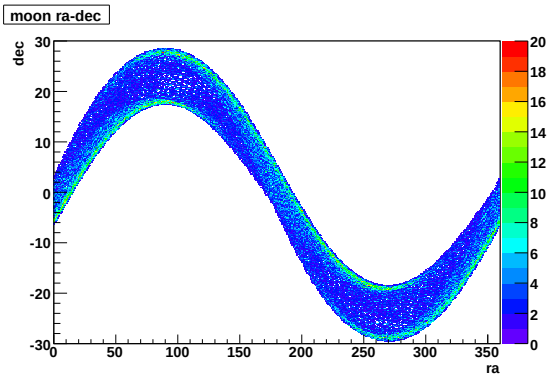

(a) RA-dec for the Moon over the period of the entire Milagro dataset.

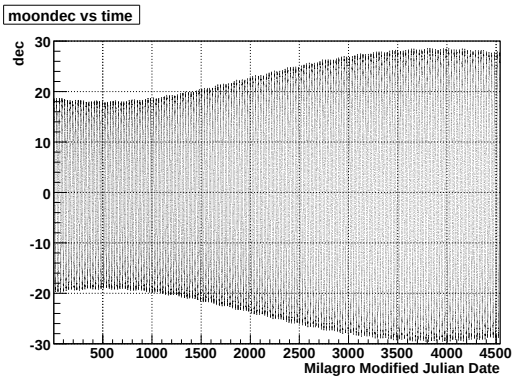

(b) Moon dec against time. Epoch 7 begins at date 3634, and epoch 9 ends at date 4541, where the Moon orbits at dec $\pm 28°$ in this period

Figure 6.1: The Moon in RA and dec over time. The dates are given in Milagro Modified Julian Date, which is julian date-2450000.5. The Moon does not orbit between constant declinations unlike the Sun. For Milagrito (the precursor of Milagro) analysis the Moon was $\sim \pm 18.5°$, but for the epoch 7-9 analysis the Moon orbits at $\sim \pm 28°$

background map. With this choice of coordinate system we opt for excellent background estimation over equal-area preservation and relative direction preservation.

Rejected Alternative Approaches

An alternative approach would be to use an azimuthal equal-area projection which preserves both area and the relative positions with time as the Moon moves. This would be implemented by periodic alignment of the coordinate system along the direction of deflection of the cosmic rays. Cosmic rays at low energies deflect in many directions, but above a threshold energy—which is dependent on the relative positions of the Moon and Milagro—the deflection of the cosmic rays is along a single direction, assuming the Earth's magnetic field is a dipole.

In this approach, the background could be estimated using two methods. In the first, a series of fake Moons are simulated at an identical RA to the real Moon. The signals at the fake Moon positions are then used to estimate the background at the real Moon position.

In the second, known as time sloshing, for each position in the signal map many positions at the same local coordinates but at a different time are used to estimate the background. This is the same principle as the MDI background, as the signal passes overhead a point with the same local coordinates, but at a different time is equivalent to a different RA. Both these methods, especially using the geomagnetically aligned coordinates, were tested and found to be poor at estimating background for the Moon.

6.1.4 Significance Maps

The unsmoothed signal minus background map, or excess-map, with cuts on $N_{fit} > 40$, zenith angle$<60°$, with a ROI=3° exclusion is shown in fig. 6.2. Remarkably, the sink is so deep that one can observe the Moon shadow clearly without smoothing.

The smoothed map of significances, as defined in section 3.3, calculated with 2.1° boxcar smoothing is shown in figure 6.3. A very deep and clear shadow is seen to a depth of greater than 60σ –the most significant object on the sky yet seen with an EAS array.

6.1.5 The Number of Shadowed Particles

Cosmic rays are incident on the Moon isotropically to a high degree. When an incident particle hits the Moon it becomes shadowed, and will not be observed by the detector. The combination of the Milagro point spread function (PSF) and the geomagnetic field spreads out the remaining unshadowed events. The Moon takes up an angular size of about 0.21 of a square degree, so we would expect the total number of events shadowed to be the total number of background events in the shadowed Moon position in a region of this size.

The actual effective geometrical area taken up by the Moon is found from a Monte Carlo integration over the same period as the data, as described in sec. 7.7.2. If there were no PSF or geomagnetic field the Moon-map would be a sharp circle, with some distortion from the coordinate system, at the nominal Moon position. The map would be missing exactly the number of events explained above.

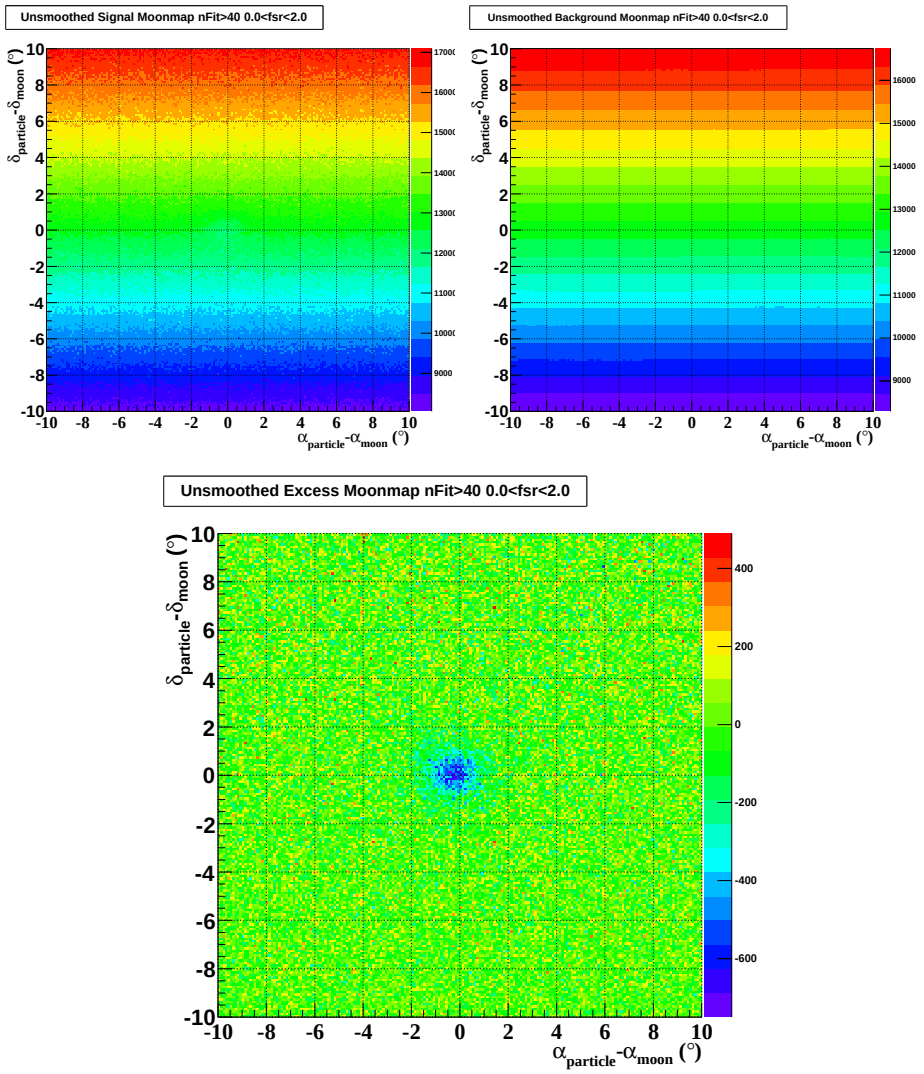

Figure 6.2: Displayed are the signal events from the region of the Moon (top left), the background calculated using Milagro direct integration (top right) and the excess-map of signal minus background (lower portion). The data is from Sep 05-Mar 08 cut on N_{fit}>40 and θ<60° with no smoothing.

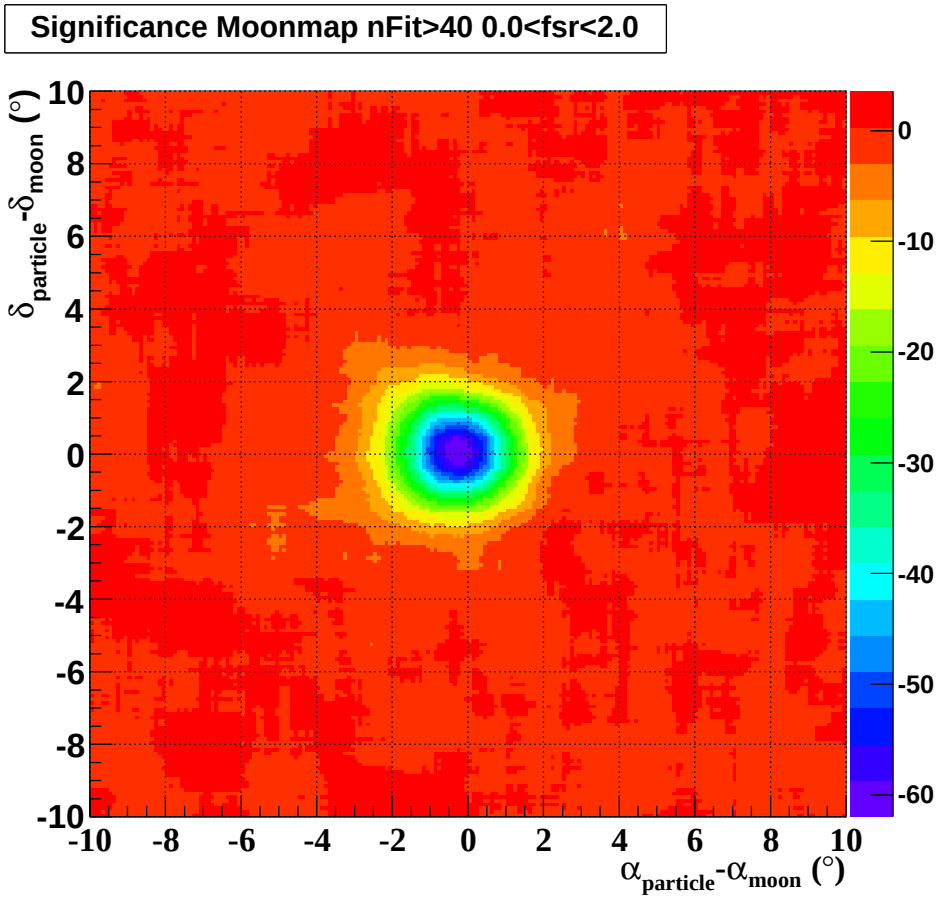

Figure 6.3: Moon-map significances from Sep 05-Mar 08, with cut of N_{fit}>40 and θ<60° and boxcar smoothed over 2.1°.

6.1.6 Integrated Fractional Deficit

Integrating outwards from the nominal (or fitted) Moon position, one would expect to recover the total number of shadowed events that have been smeared out by the PSF and geomagnetic field.

In figure 6.4 we show the fraction of shadowed events as a function of radial distance from the fitted (see sec. 6.4) Moon position. The plot is made from signal minus background integrated outwards to include all events within the radius in steps of 0.1° and is shown in figure 6.4. The error bars are determined by the total number of events in signal and background in the area included so they increase with radius from the center of the shadow.

6.1.7 Differential Fractional Deficit

In the integrated deficit plots consecutive bins are correlated. To gain uncorrelated plots, other than a small correlation from the calculation of the number of shadowed events, one can look at the differential fractional deficit –in which the signal minus background is plotted within annuli of increasing radius from either the nominal or fitted source position. Alternatively, one can use the fractional deficit density, which has no correlation and is sign-flipped as the Moon is a sink. This is the summed excess for the annulus but divided by the area of each annulus. Looking at the differential deficit plots, the shadow does not seem to extend beyond 3°. The number of sigma from zero distribution is consistent with this, showing a clear non-random behavior from the full set of events, but consistent with no excess farther than 3° (see figures 6.5 and 6.6). The plot is consistent with all shadowed events

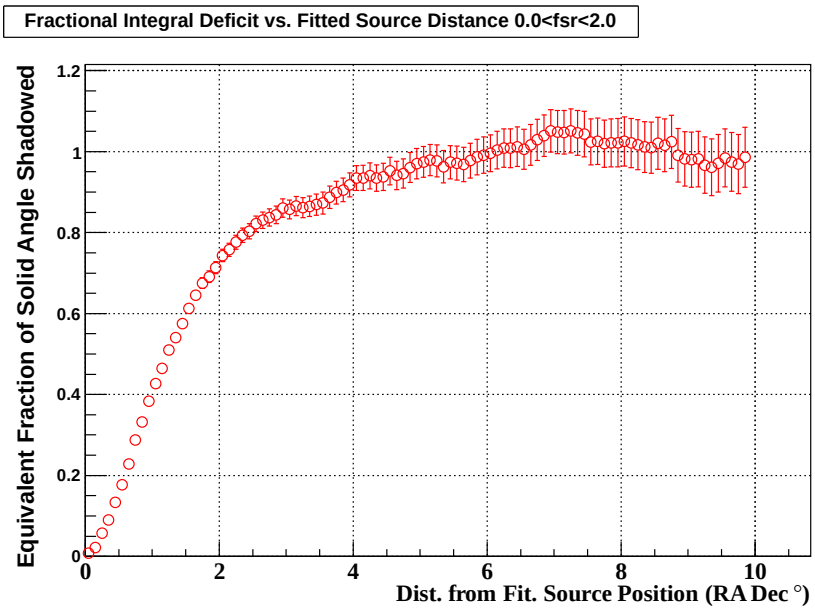

Figure 6.4: Integrated fractional deficit map for the Moon in data. Note there is nothing forcing the curve to asymptote to or plateau at 1. A value of 1 means all the events shadowed by an area the geometrical size of the Moon have been recovered.

recovered at 3° validating the choice of ROI=3°

As with the integrated maps, the annuli are found relative to the fitted shadow position, as described in sec. 6.4.

6.2 Consistency of Background Estimation

As a check of the background determination, found from the MDI technique, we introduce a fake Moon that co-moves with the real Moon –but is displaced in RA by 90°. The plots are shown in figures 6.7 and 6.8. The integrated deficit plot and differential deficit plots are both consistent with statistical fluctuations in the absence of a sink. The distribution of significances for the whole sky is also included and is consistent with a gaussian, width one, centered on zero as expected. Though we use a fake Moon, as the map is co-moving the real Moon will appear at $-90°$ so the region around the real Moon is excluded from the all-sky distribution of significance.

6.3 Energy Parameter binned Moon-maps

The Moon-maps in 10 FRASOR bins—the Milagro energy parameter (see sec. 3.5)—are shown in figures 6.9, 6.10 and 6.11. As we increase FRASOR the angular extent of the shadow appears to decrease in RA and dec. Also the shadow in RA for 0.0<FRASOR<0.2, 0.2<FRASOR<0.4 and 0.4<FRASOR<0.6 is to the left of zero, corresponding to a Moon shadow shifted to the west. For higher FRASOR bins the shadow appears to be consistent with the nominal position of the Moon. In decli-

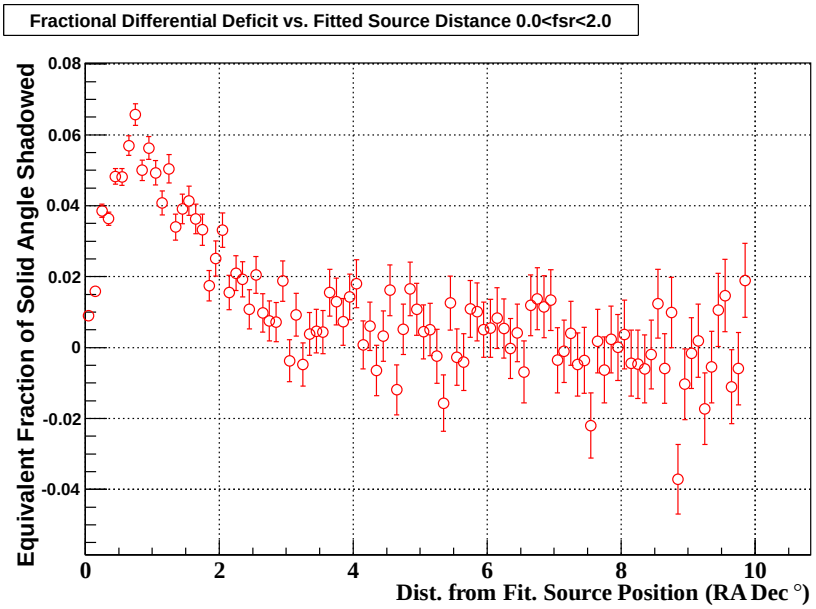

(a) Differential fractional deficit in 0.1°

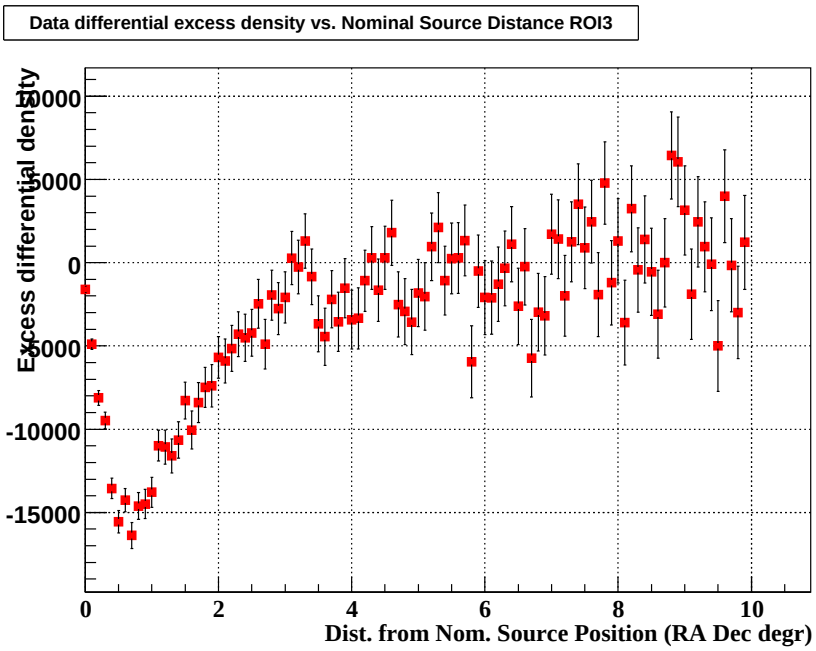

(b) Differential excess density deficit in events/0.1 square degree

Figure 6.5: Differential deficits for the Moon in data, with cuts N_{fit}>40 and θ<60°.

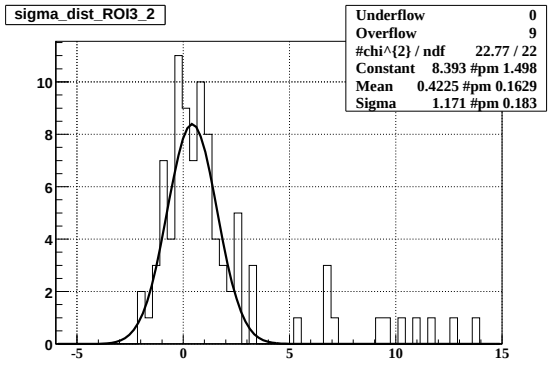

(a) Distribution number of sigmas from zero from the differential density, 0-10°.

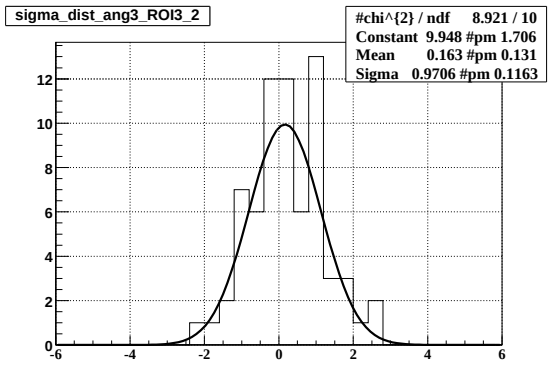

(b) Excluding the shadow region: distribution of number of sigmas from zero of the differential density 3-10°

Figure 6.6: Distributions of sigmas of the differential density of the Moon, from fig. 6.5.

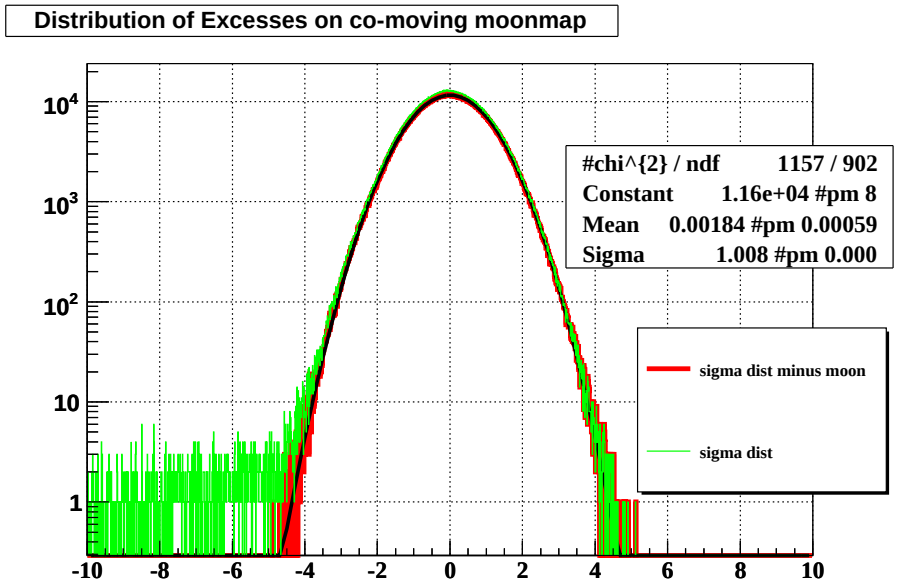

Figure 6.7: Distribution of significances for the fake Moon on the full sky, with cuts N_{fit}>40 and θ<60°. The fit is in black. Subtracting a region around the real Moon of 3° centered on the Moon leaves a fit that is consistent with a gaussian, width one, centered on zero.

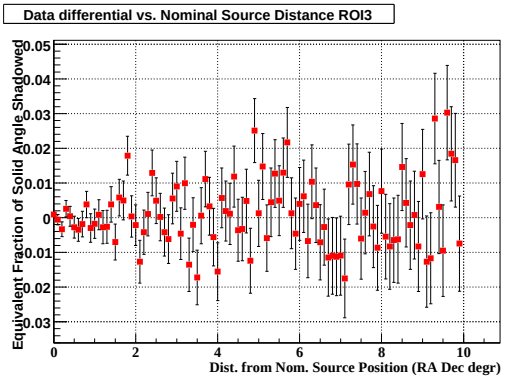

(a) Differential fractional deficit in 0.1° annuli for the fake Moon

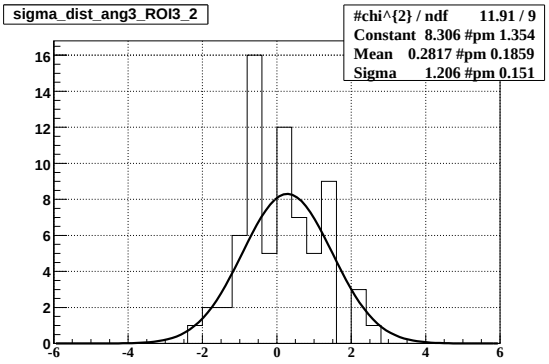

(b) Distribution of number of sigmas from zero from the differential fractional deficit, 0-10°, for the fake Moon

Figure 6.8: Distribution of significances for the fake Moon. Cuts are N_{fit}>40 and θ<60°.

nation, the shadow appears to be largely centered on zero. We would expect the geomagnetic deflection to decrease with increasing energy. As energy is correlated with FRASOR, the shadow positions in higher FRASOR bins should be closer to the nominal Moon position, which is what is observed.

We would expect to see a similar effect on the width of the shadow. However, this has two contributions. The first effect is that the low FRASOR bins have poor angular resolution, which widens the shadows. The second effect is the broadening of the shadow due to geomagnetic deflection. This effect is governed by the effective area response of the detector with energy, which is described in sec. 7.4.

6.4 A 2-D Gaussian is a good fit to the Moon Shadow

In the unsmoothed excess-maps, the particle shadow is modeled, as a function of RA α and dec δ, by a 2-D gaussian of the form:

$$f(\alpha,\delta;A,\alpha_0,\delta_0,\sigma_\alpha,\sigma_\delta) = \frac{A}{2\pi\left(\sigma_\alpha^2+\sigma_\delta^2\right)}\exp\left[-\frac{1}{2}\left(\frac{(\alpha-\alpha_0)^2}{\sigma_\alpha^2}+\frac{(\delta-\delta_0)^2}{\sigma_\delta^2}\right)\right] \tag{6.1}$$

where A is the particle shadow depth, α_0, δ_0 and σ_α, σ_δ are the locations and widths along the RA and dec axes respectively in particle minus moon coordinates. This function is a good fit to the observed Moon shadow. The excess-map with N_{fit}>40 and zenith angle<60° for the period of epochs 7-9, with the fit is shown in fig. 6.12. The 2-D gaussian fitting function appears to match the data both in position and depth. The residual map (of the data minus the fit), the significance map of

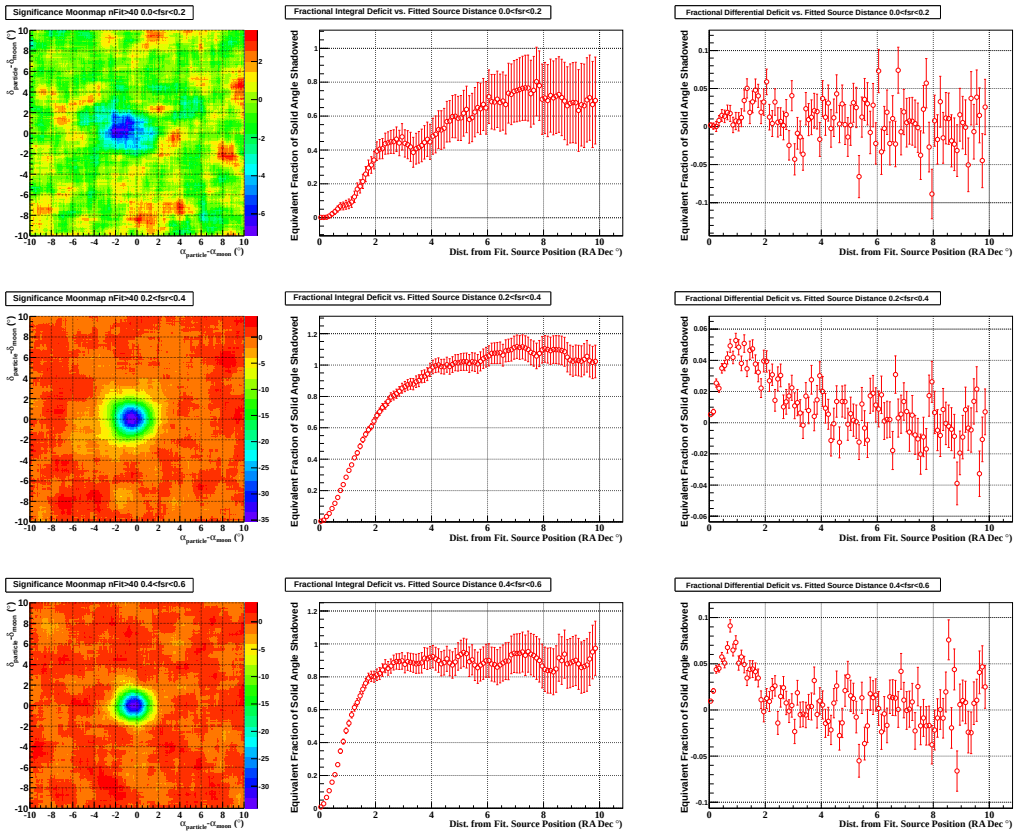

Figure 6.9: Moon-maps for data in the lowest 3 FRASOR bins. Top 0.0<FRASOR<0.2, middle 0.2<FRASOR<0.4 and bottom 0.4<FRASOR<0.6, with cuts N_{fit}>40 and θ<60°. The significance maps are boxcar smoothed over 2.1°.

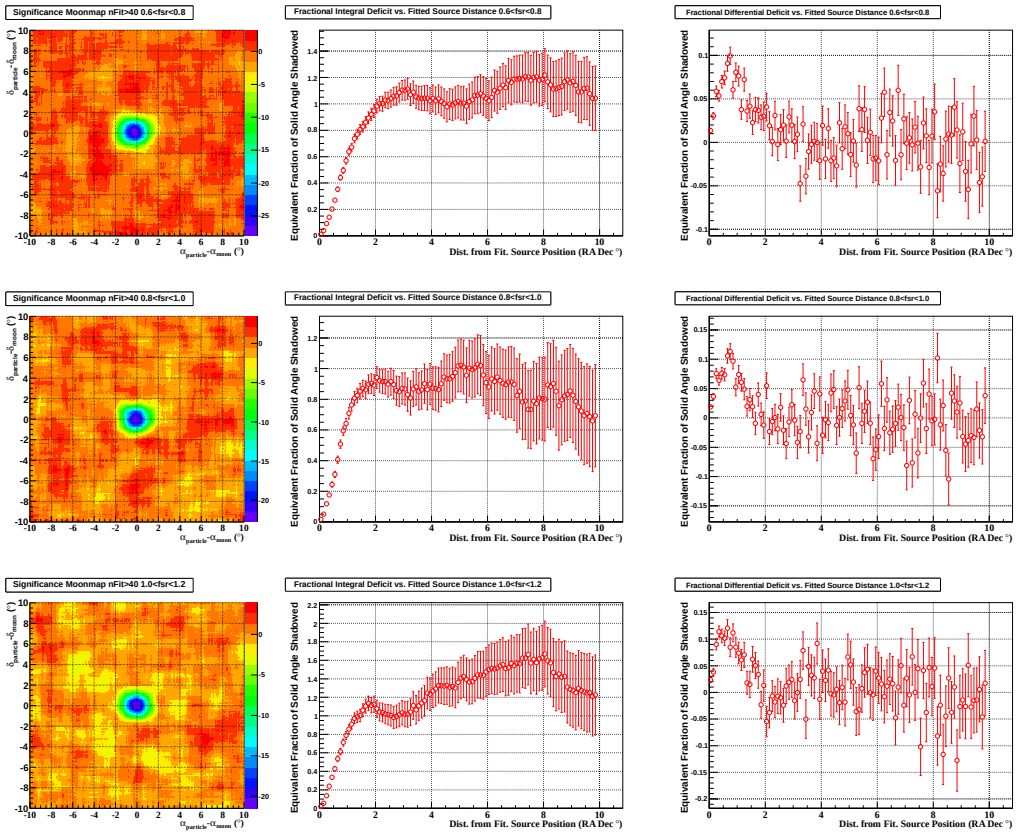

Figure 6.10: Moon-maps for data in the middle 3 FRASOR bins. Top 0.6<FRASOR<0.8, middle 0.8<FRASOR<1.0 and bottom 1.0<FRASOR<1.2, with cuts N_{fit}>40 and θ<60°. The significance maps are boxcar smoothed over 2.1°.

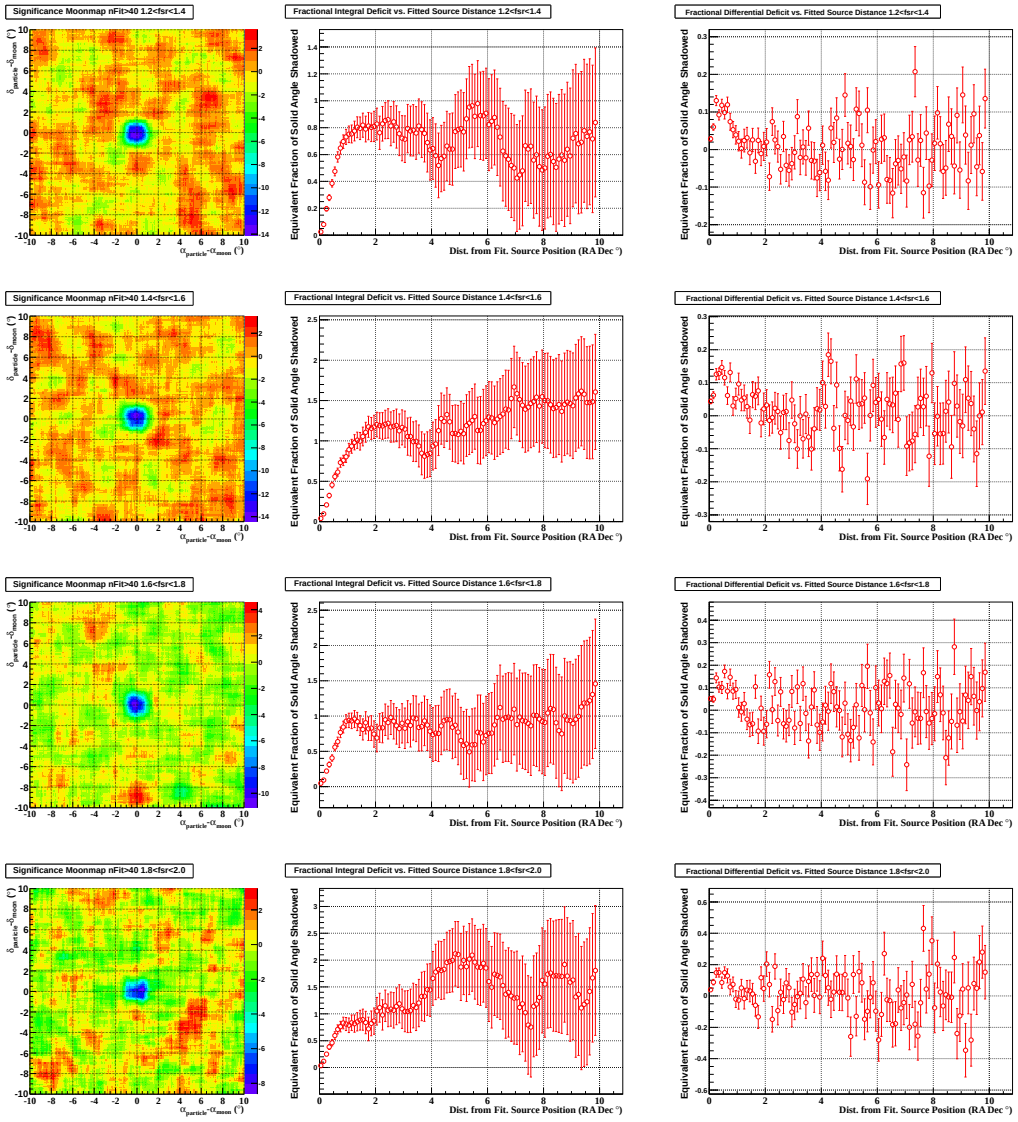

Figure 6.11: Moon-maps for data in the highest 4 FRASOR bins. Top 1.2<FRASOR<1.4, second 1.4<FRASOR<1.6, third 1.6<FRASOR<1.8 and bottom 1.8<FRASOR<2.0, with cuts N_{fit}>40 and θ<60°. The significance maps are boxcar smoothed over 2.1°.

residuals, and the distribution of significances of residuals fit to a 1-D gaussian function are also shown. Except for a slight non-zero residual average these are consistent with random fluctuations around the correct model. The Moon shadow does indeed seem to be well modeled by a 2-D gaussian. The fit parameters of eq. 6.1, in FRASOR are shown in fig. 6.13.

6.4.1 Asymmetry of the Moon Shadow

The 2-D gaussian fit function is symmetrical along RA, but the deflection of particles is not symmetric –it is biased along the direction of RA by the geomagnetic field. To assess the level of asymmetry in the shadow, compared to the symmetric fitting function, we project the Moon shadow excess-map along the RA direction. As a check, we also project the excess-map along the dec direction. These are shown in figure 6.14. We see a slight asymmetry in the data along RA, as expected, but this asymmetry is small and shows only a small deviation from the 2-D gaussian fit. Along dec the the data is symmetric, and the 2-D gaussian matches the data well.

6.5 Sun-maps

The Sun transits the celestial sphere along the ecliptic, which is inclined at 23° to the celestial equator, and completes ∼2.5 transits in epochs 7-9. In this period 104 million events passed cuts within 5° of the Sun and there were an average of 10400 events/0.1 square degree.

As discussed in chapter 5, unlike the Moon, the Sun has its own magnetic field

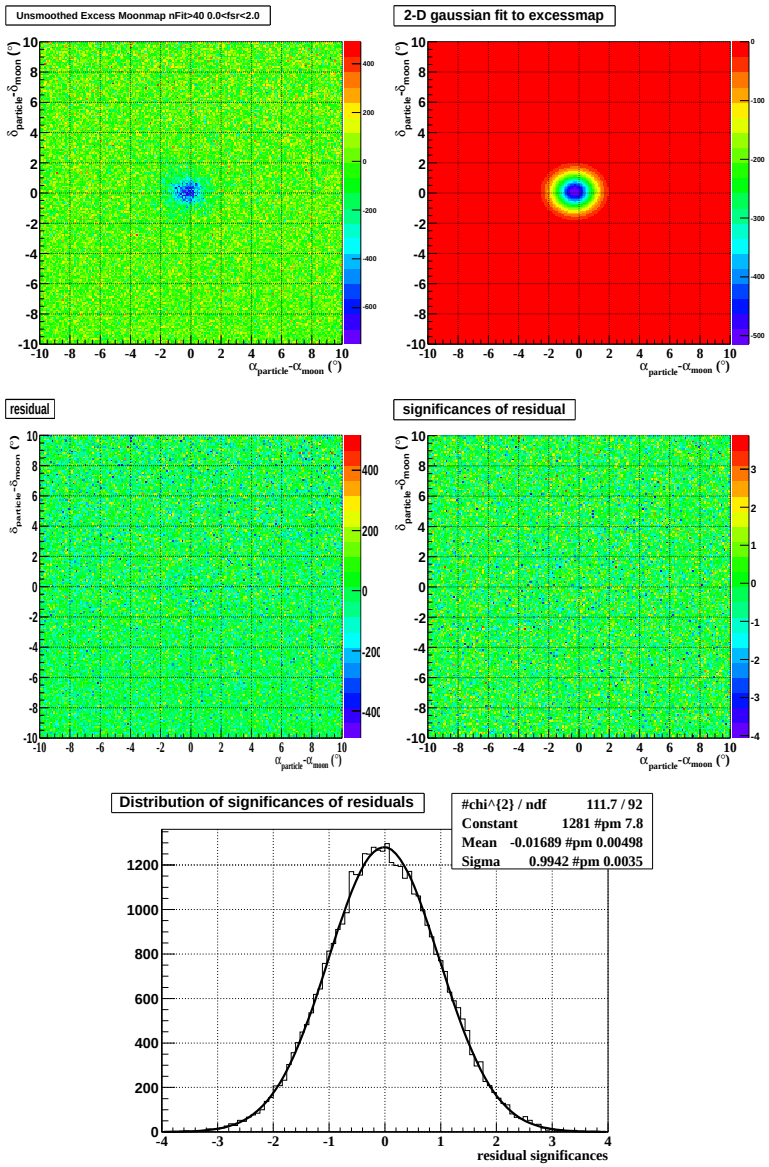

Figure 6.12: The excess-map of the Moon in 0.1°×0.1° bins with N_{fit}>40 and zenith angle<60°, then fit to eq. 6.1, with the residuals. The final plot is distribution of residuals, limited to the region -3°<RA<0° -3°<dec<-3° fit to a 1-D gaussian.

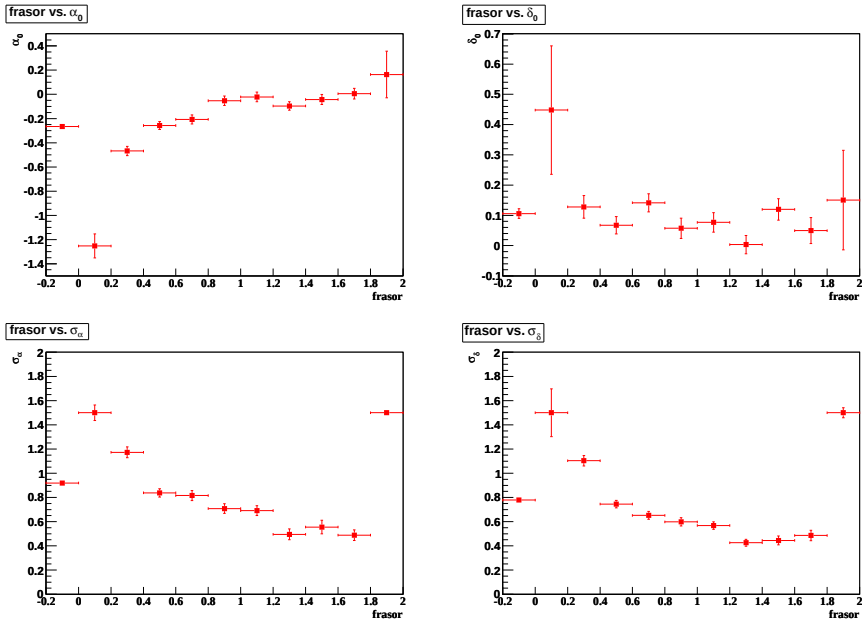

Figure 6.13: The parameters of a 2-D gaussian fit to the Moon shadow, in increasing FRASOR bins. The negative bin is the full set of events with no FRASOR cut.

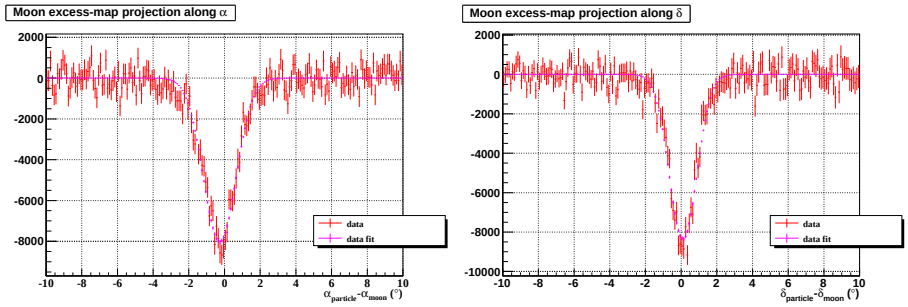

Figure 6.14: Projection of the Moon shadow in data along RA and dec compared to the 2-D gaussian fit, in a slice of width 2°, centered on the nominal Moon position.

that varies over its 2×11 year solar cycle. During the solar cycle the Sun increases in activity and its local magnetic field is expected to become highly non-dipolar. From this point, known as solar maximum, the activity of the Sun decreases and the local field of the Sun returns to a dipole-like state (opposite in polarity to 11 years before) of low activity. Solar cycle 23 ended in Spring 2008, coinciding with the end of the Milagro data set. In fact Milagro and Milagrito (the Milagro precursor) cover nearly the entire 11-year cycle. The first (Milagrito) analysis was done close to solar minimum and a clear solar shadow was observed. Epochs 7, 8 and 9 are closer to solar minimum and again a clear solar shadow is observed. In figures 6.15 and 6.16 we show the Sun-map significance and excess-maps for epochs 7-9 with cuts on N_{fit}>40 and zenith angle<60° with ROI=3°, boxcar smoothed to 2.1°. In these maps the solar shadow is clearly seen before smoothing and after smoothing is observed to a depth of about 35σ.

6.5.1 Integrated and Differential Fractional Deficit Plots for the Sun

Figure 6.17 shows the integrated and differential fractional deficits and figure 6.18 shows the distribution of sigmas from zero for the differential plot. The distribution of sigmas from zero for the differential plot greater than 2°from the fitted Sun position, in fig. 6.18, is consistent with noise, which indicates that the shadow does not extend much farther than 2°. Note that the integral fractional deficit for the Sun at 3° plateaus to about 0.7 rather than to 1. This is expected, as in contrast to the Moon, the Sun has a magnetic field. If (for instance) the Sun's

field is dipolar then particles below a certain energy will not be able to hit the Sun at the equator. Particles with energies such that a trajectory towards the Sun but are deflected away will not contribute to the shadow. From Liouville's theorem of conservation of phase space volume for every particle deflected away from the Sun another will be deflected towards Milagro in its place, if cosmic rays are incident on the Sun isotropically. Some other particle of the same energy will now be deflected into the Sun direction and make up for the particle that was deflected away. To reiterate there are some lower energy particles that would be shadowed by the Moon, but not the Sun as a consequence of its magnetic field.

6.5.2 Consistency of Background Estimation for the Sun

As for the Moon, we test a fake co-moving Sun displaced in RA as shown in figures 6.19 and 6.20. As discussed above for the Moon, the fake Sun is consistent with noise and the distribution of all-sky significances is consistent with a gaussian of mean zero and width one.

6.5.3 Sun-maps in Energy Parameter bins

The Sun-maps are also presented in FRASOR bins in figures 6.21, 6.22 and 6.23. The fit parameters of eq. 6.1, in FRASOR are shown in fig. 6.24.

The Sun shows much of the same behavior as the Moon. As we increase FRASOR the width of the shadow appears to decrease in RA and dec. Again the shadow in RA for 0.0<FRASOR<0.2, 0.2<FRASOR<0.4 and 0.4<FRASOR<0.6 is to the left of zero, corresponding to a Sun shadow shifted to the west. This is probably again

due to the effect of the geomagnetic field, as opposed to the HMF or the coronal field. Also, the shadow in the dec-direction appears to be largely centered on zero. For higher FRASOR bins, the shadow appears to be consistent with the nominal position of the Sun. We would expect the geomagnetic deflection to decrease with increasing energy. As energy is correlated with FRASOR, the shadow positions in higher FRASOR bins should be closer to the nominal Sun position, which is what is observed.

Like the Moon, we would expect to see a similar effect on the width of the Sun shadow, with broadening at low FRASOR bins and due to the geomagnetic deflection, which is what is seen.

Looking at the integrated fractional deficit plots we see an increase in the total fraction shadowed as we increase FRASOR. With no cut on FRASOR we find about 0.7 of particles that would be shadowed by the geometrical area of the Sun are recovered at 10°. However for low FRASOR bins this fraction is much less, with nearly no particles shadowed for the lowest FRASOR bin and 0.2 of the geometrical area of the Sun shadowed for 0.2<FRASOR<0.4. For high FRASOR bins nearly all events are recovered. These results are consistent with how we expect particles to be shadowed. Low energy particles, which are more likely to be in lower FRASOR bins, are deflected away from the Sun by its magnetic field so do not reach the photosphere, and hence are not shadowed. High energy particles, so particles more likely to be in higher FRASOR bins, are less likely to be deflected away from the Sun by its magnetic field so are more likely to be shadowed. This demonstrates that we have a clear sensitivity to the HMF and particularly the Sun's coronal field.

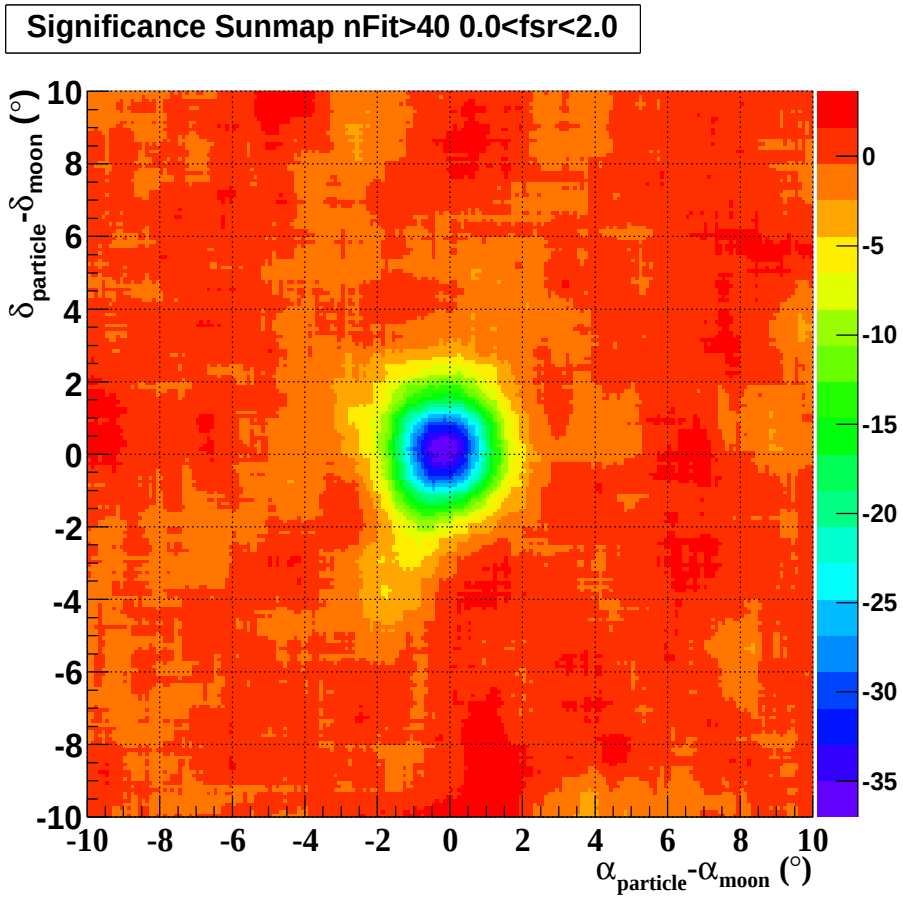

Figure 6.15: Milagro Direct Integration Sun-map significances from Sep 05-Mar 08 cut on N_{fit}>40 and theta<60° with boxcar smoothing over 2.1°.

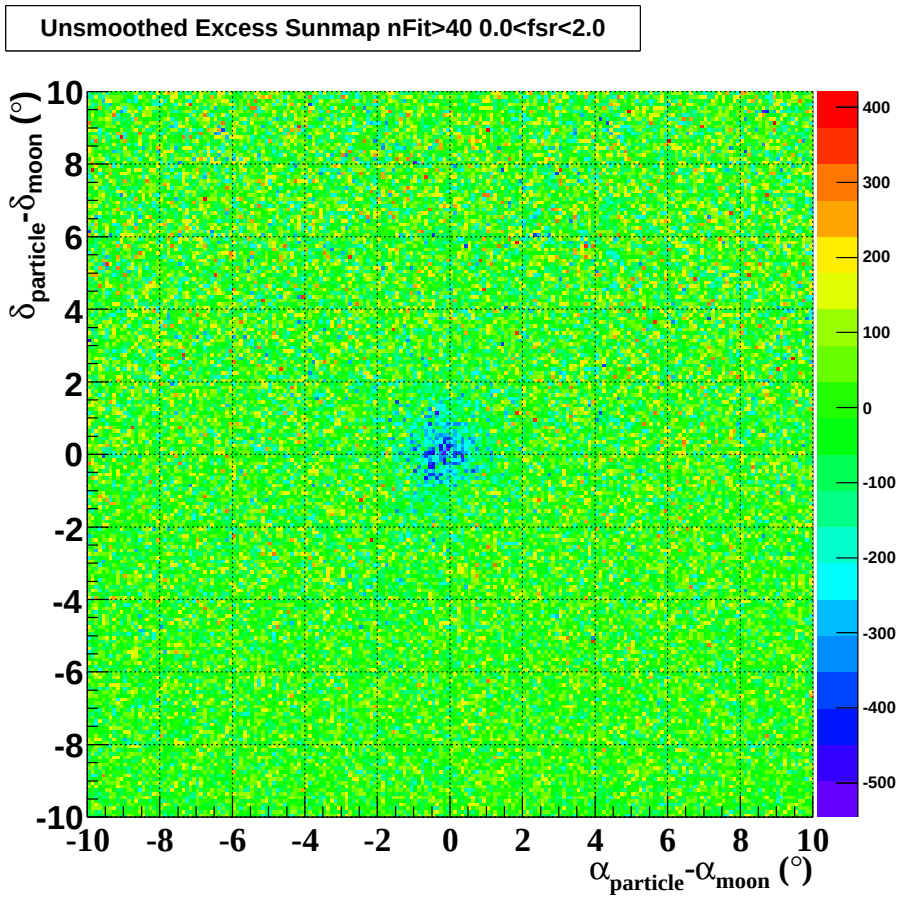

Figure 6.16: Milagro Direct Integration Sun-map excesses from Sep 05-Mar 08 cut on N_{fit}>40 and theta<60° unsmoothed.

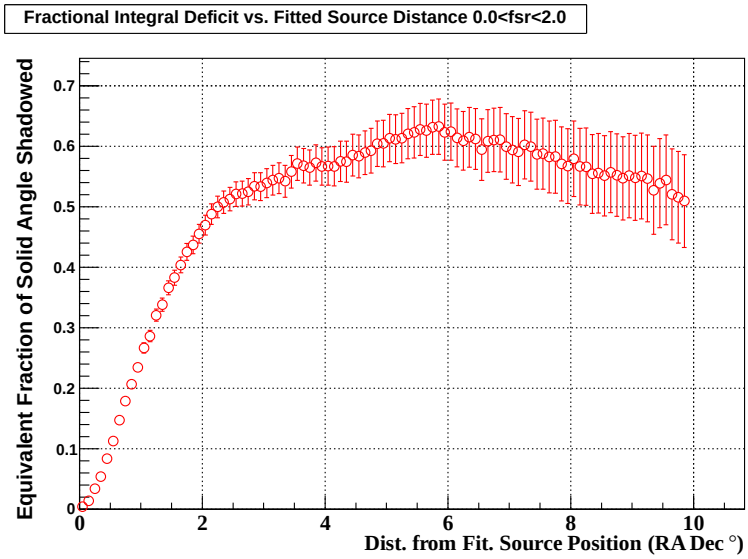

(a) integrated fractional deficit

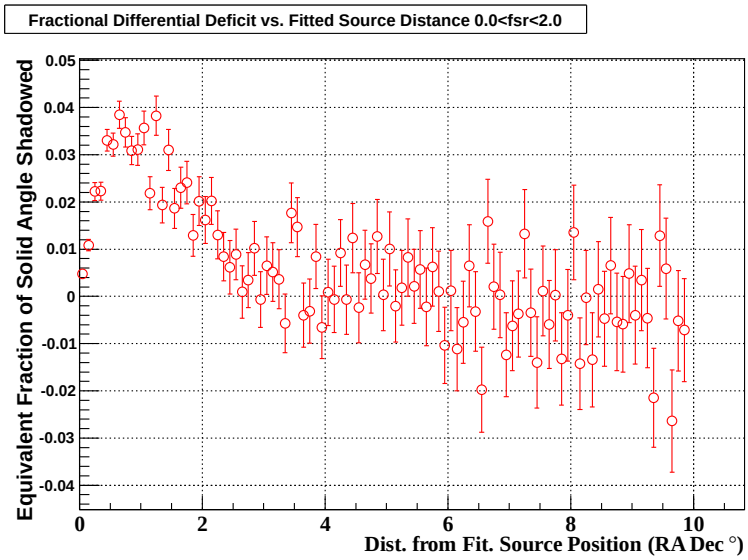

(b) differential fractional deficit

Figure 6.17: Differential and integrated deficits for Sun-maps for epochs 7-9, cuts are N_{fit}>40 and theta<60°.

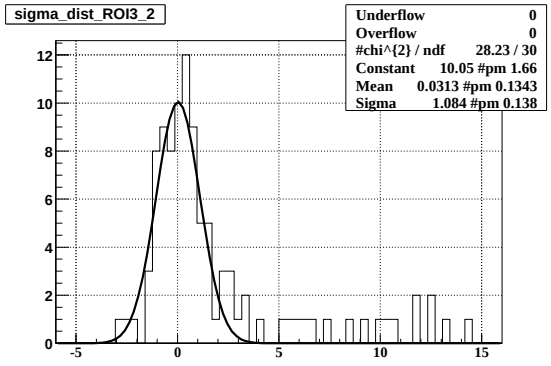

(a) distribution of number of sigmas from zero –all angles

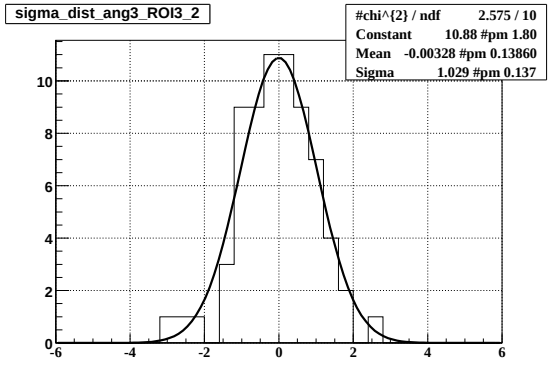

(b) distribution of number of sigmas from zero –angles> 2°

Figure 6.18: Distribution of significances for Sun-maps for epochs 7-9 from fig. 6.17. Cuts are N_{fit}>40 and theta<60°.

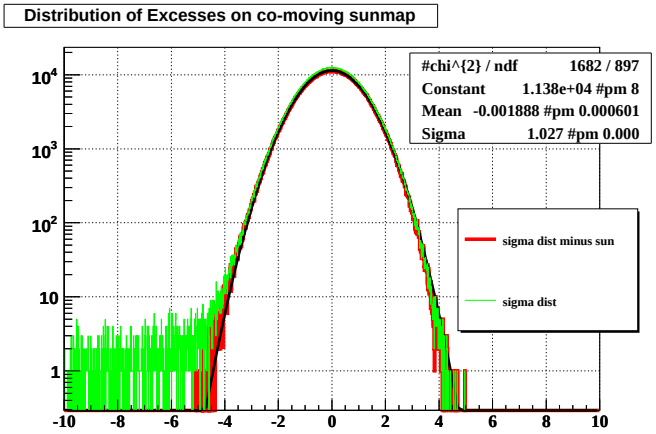

(a) Significance distribution for the fake Sun. The fit is in black. Subtracting a region around the real Sun of 3° centered on the Sun leaves a fit that is consistent with a gaussian, width 1 centered on zero.

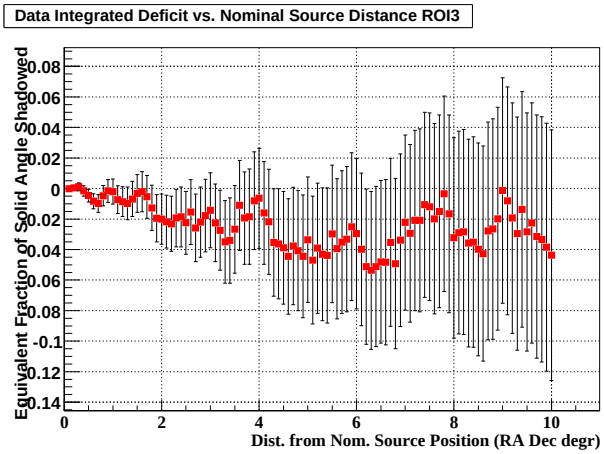

(b) integrated fractional deficit in 0.1° for fake Sun

Figure 6.19: Fake Sun plots for co-moving fake Sun displaced by 90° RA and integral deficit. Cuts are N_{fit}>40 and theta<60°.

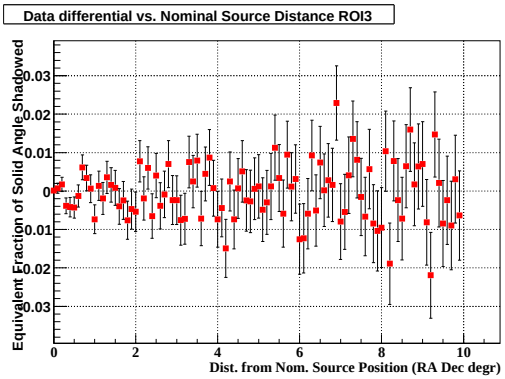

(a) differential fractional deficit in 0.1° for fake Sun

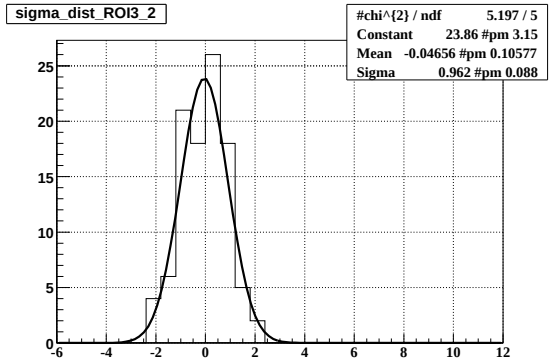

(b) distribution number of sigmas from zero all data for the fake Sun

Figure 6.20: Differential deficit and distribution of sigmas from Sun-maps in fig. 6.19. Cuts are N_{fit}>40 and theta<60°.

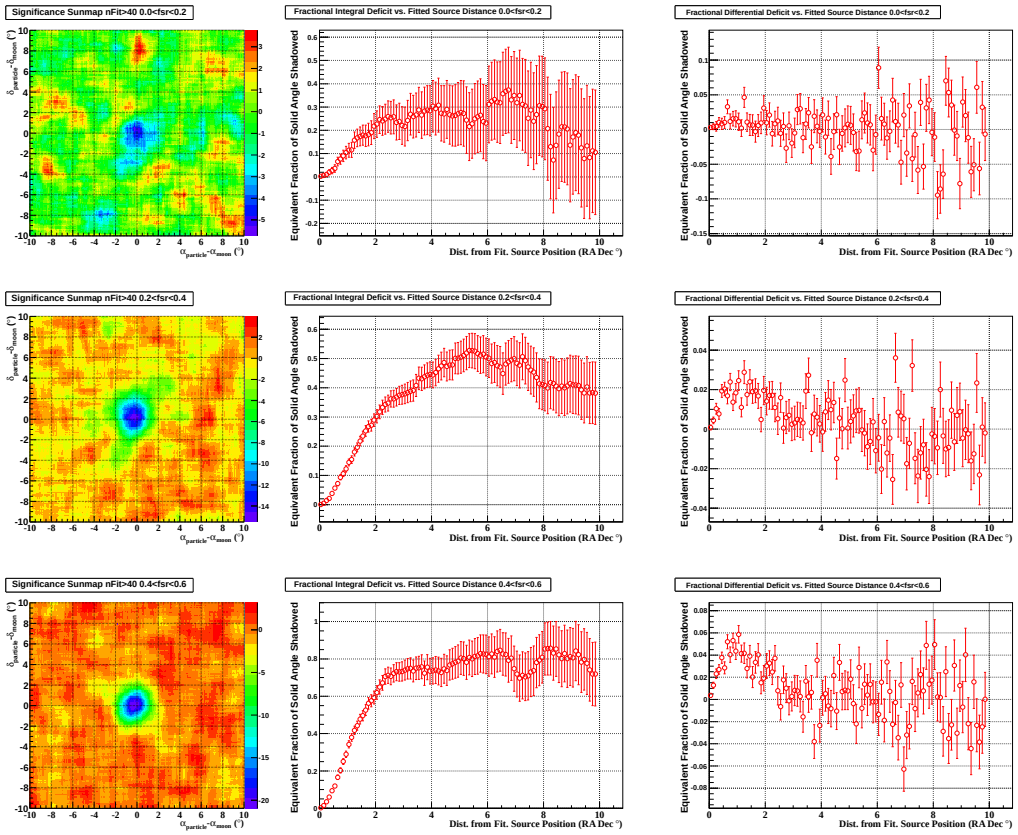

Figure 6.21: Sun-maps for data in the lowest 3 FRASOR bins. Top 0.0<FRASOR<0.2, middle 0.2<FRASOR<0.4 and bottom 0.4<FRASOR<0.6, with cuts N_{fit}>40 and θ<60°. The significance maps are boxcar smoothed over 2.1°.

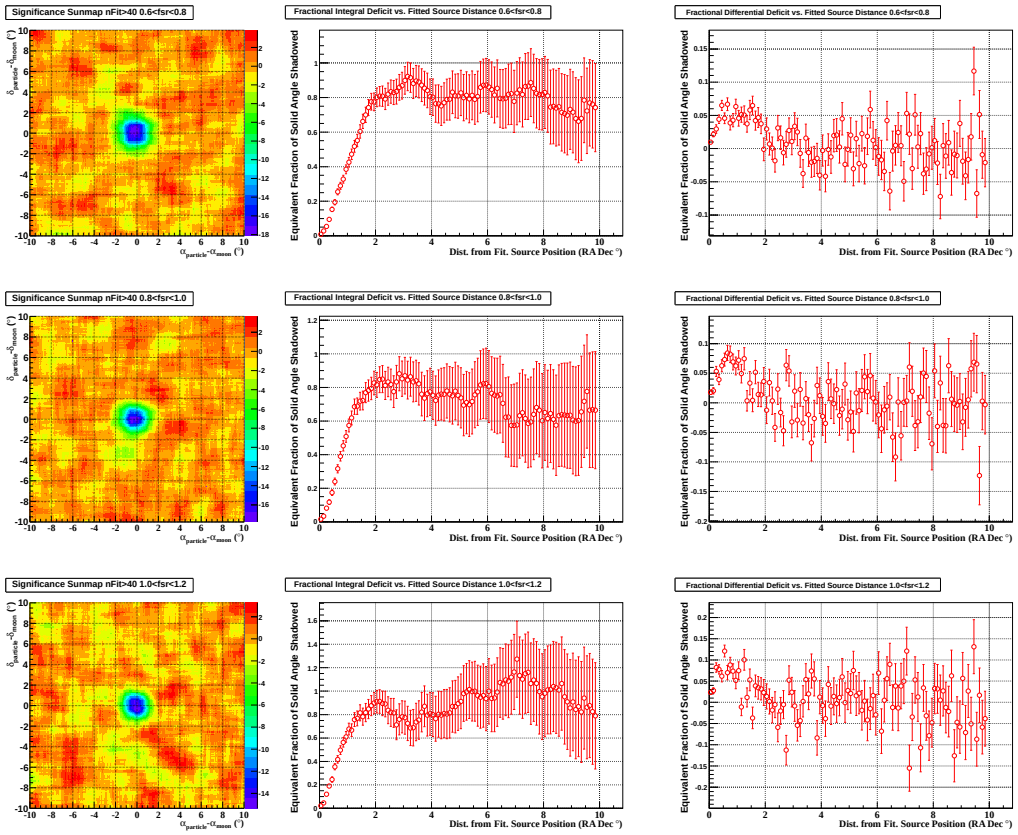

Figure 6.22: Sun-maps for data in the middle 3 FRASOR bins. Top 0.6<FRASOR<0.8, middle 0.8<FRASOR<1.0 and bottom 1.0<FRASOR<1.2, with cuts N_{fit}>40 and θ<60°. The significance maps are boxcar smoothed over 2.1°.

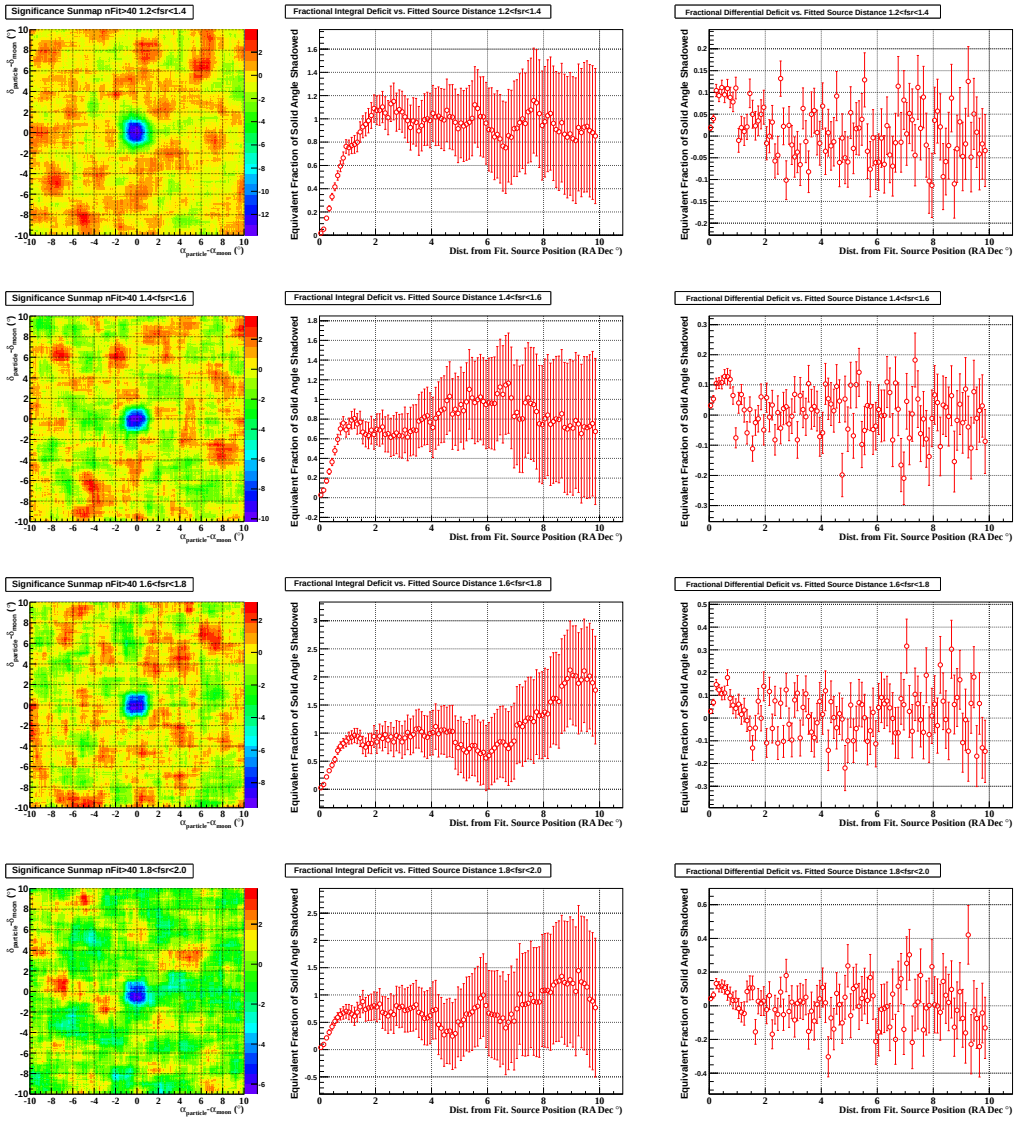

Figure 6.23: Sun-maps for data in the highest 4 FRASOR bins. Top 1.2<FRASOR<1.4, second 1.4<FRASOR<1.6, third 1.6<FRASOR<1.8 and bottom 1.8<FRASOR<2.0, with cuts N_{fit}>40 and θ<60°. The significance maps are boxcar smoothed over 2.1°.

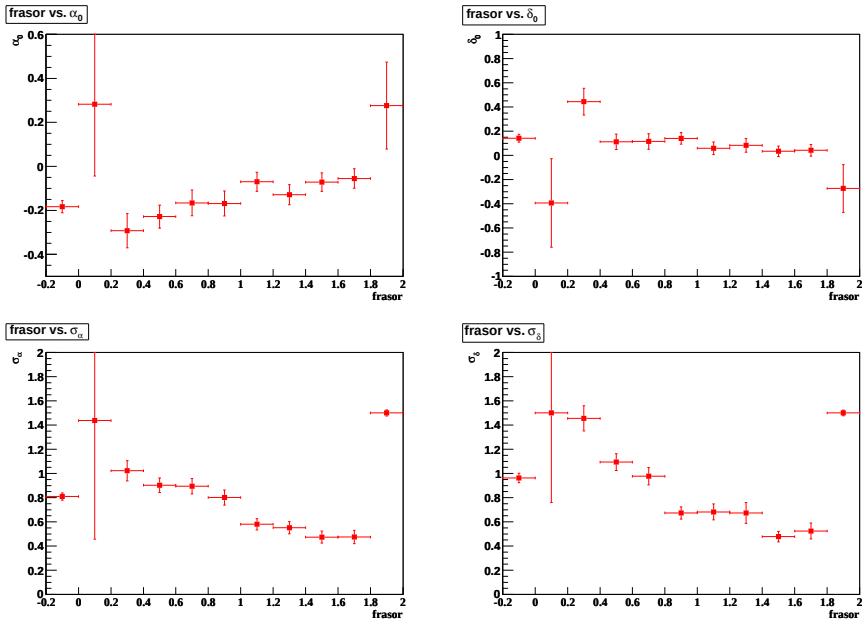

Figure 6.24: The parameters of a 2-D gaussian fit to the Sun shadow, in increasing FRASOR bins. The negative bin is the full set of events with no FRASOR cut.

Chapter 7

Moon and Sun Monte Carlo

This chapter describes the Monte Carlo simulation used for modeling the cosmic-ray Moon or Sun shadow that is observed by Milagro.

This Monte Carlo, in principle, can be used to perform an energy calibration of Milagro, it can aid in placing an upper limit on the $\bar{p}/p$ flux ratio and can be adapted to probe the coronal field of the Sun.

The Moon Monte Carlo (MC) has three sets of inputs. The first is the spectral index and flux of each species being simulated and is used to choose particle type and energy (see sec. 7.1). Both the second and third inputs are found from Milagro simulated data files of the the Milagro response to cosmic rays. From these we find the detector effective area (see sec. 7.4) and the angular resolution (see sec. 7.5) for each simulated particle.

Given the energy, time (and hence the Moon/Sun position), species and magnetic field model (see sec. 4.3.1), we can track a particle through the geomagnetic field and see if a particle is shadowed by the Moon or Sun (see sec. 7.2). The true

direction of the particle is smeared with the Milagro angular resolution to determine the detected direction. The shadowed and unshadowed particles are then put into two skymaps with effective area weighting. The map of shadowed particles is an excess skymap centered on the Moon and equivalent to the excess-maps in the data. In total 1.3×10^{10} particles are tracked, over the 907 days of the period of epochs 7-9 –which is the same period as the Moon shadow data maps.

7.1 Primary Spectra

The primary spectrum for each species is used to determine the fraction of each simulated species and the energy spectrum of the particles in that species.

Cosmic rays detected by Milagro are primarily composed of protons and helium. The fluxes and spectral indices of protons and helium in this Monte Carlo are taken from JACEE measurements [93]. However, there are heavier elements, such as carbon, oxygen, neon, magnesium, silicon and iron. The fluxes of these at TeV have measured by the ATIC-2 experiment [94]. Other elements that have not been measured are approximated by the effects of increasing the flux of measured elements of similar weight.

A single power law fit is imposed on the ATIC-2 data of each species to find the fluxes at 1 TeV and the differential spectral indices, as shown in fig. 7.1. The results of the fit are displayed in table 7.1. For species i, the fit takes the form $F_{0,i}E^{-\alpha_i}\ E^{2.75}$ where F_0 is the flux at 1 TeV.

Other experiments have measured the cosmic-ray primary spectra for protons and helium [95; 96; 97] and heavy elements [98]. The spectra used in this MC are

species	flux $(m^2 s.sr.TeV)^{-1}$	spectral index	fraction	flux factor	additional species
protons	0.111	2.80	0.452		
helium	0.081	2.68	0.267		
carbon	0.013	2.59	0.037	1.2	B
oxygen	0.024	2.60	0.071	1.4	N,F
neon	0.006	2.59	0.017	1.33	Na
magnesium	0.009	2.65	0.030	1.25	Al
silicon	0.010	2.65	0.032	1.37	P,S
iron	0.031	2.62	0.093	1.5	Cl,Mn

Table 7.1: Fractions with spectra from various species. Protons and helium are from JACEE, the heavy species are from ATIC-2 fits from fig. 7.1.

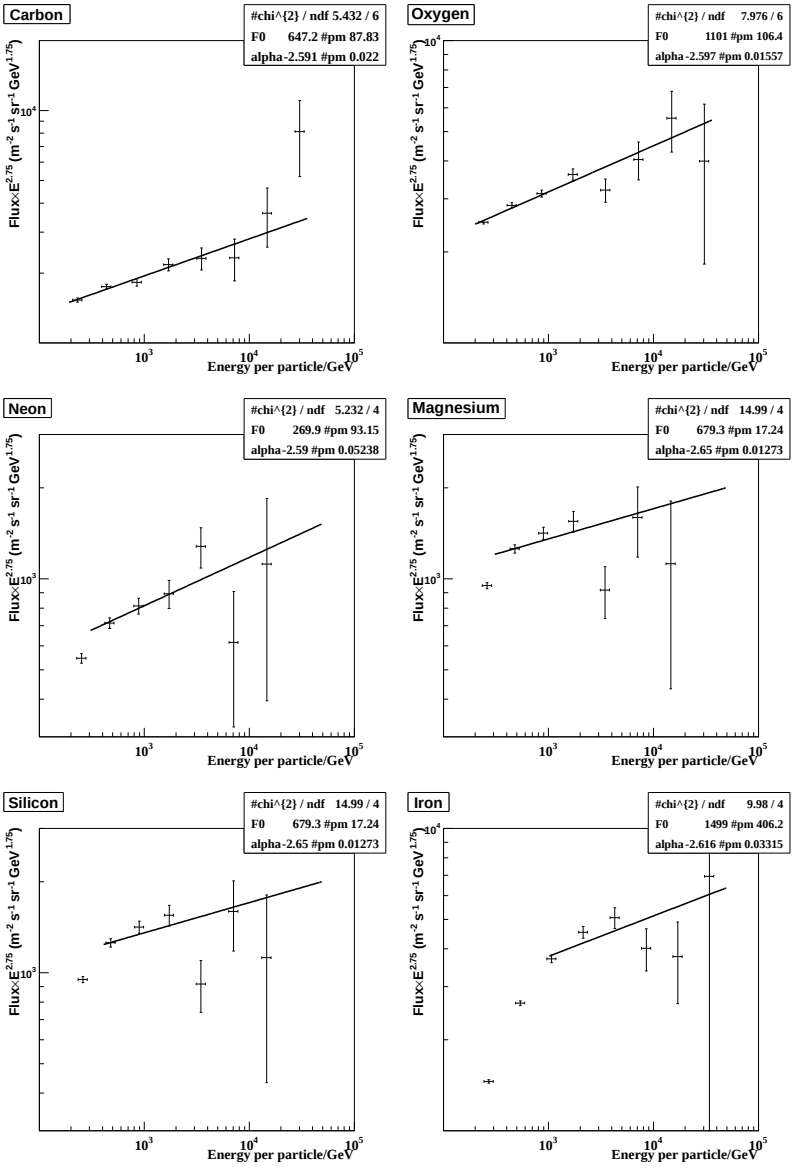

Figure 7.1: ATIC-2 fluxes with power law fit for heavy species. The data is taken from the ATIC collaboration in [94]. The flux is found at GeV and then rescaled to the TeV scale by an additional factor of $0.001^{\alpha-1}$.

consistent with these measurements.

7.2 Tracking the Particles

At each time step in the MC the position of the Moon or Sun is calculated. For the 907 days of Epochs 7-9 particles are thrown in 10 s intervals. At each interval 41×41 particle tracks are simulated leading to a total of 1.3×10^{10} simulated particles. In order to ensure the particles hit Milagro, we reverse the charge of the particle and track them backwards towards the Moon or Sun.

7.2.1 Initializing the Particles

Using the fluxes and spectral indices, at each time step in the simulation species i is randomly chosen with probability:

$$f_i = \frac{F_i}{\alpha_i - 1}\left(\frac{e_0}{E_0}\right)^{1-\alpha_i} \tag{7.1}$$

where α_i and F_i are the differential spectral index and flux of species i respectively, e_0 is taken to be 0.1 TeV and is the minimum energy of particles thrown as used in eq. 7.2 and E_0 the energy scale of the flux, here chosen to be 1 TeV. The probabilities are normalized by $\Sigma\ f_i$=1.

To find the species and energy two random numbers x_1, $x_2 \in$[0,1], taken from the gsl version 1.12 library, are chosen, where x_1 is used to choose the species as described in the previous section and x_2 its energy. The energy is

$$E = \frac{e_0}{x_2^{1/(1-\alpha_i)}} \tag{7.2}$$

where e_0 is again the minimum energy of the primaries, chosen to be 0.1 TeV. The choice of e_0 is based on the effective area of Milagro with the the cut $N_{fit} > 40$. Using primary spectra from e_0=0.05 TeV were found to give the same results within statistics, but at the cost of much more computing time.

Once the species and energy are chosen, particles are arrayed on a 41×41 grid of total size 20°× 20° and then fired towards the Moon in a geomagnetic coordinate system (see sec. 4.3.1). It should be noted that a second approach could be taken here; one that would track the same number of particles. Every 0.006 s, a new particle, with a new energy and of a new species could be generated and fired towards the Moon. However, this created large fluctuations from effective area variations, so the approach of firing a grid of particles of identical energy and species every 10 s was adopted.

Each of the 1681 particles on the grid is of the same species and energy, but the direction is varied slightly from the nominal Moon direction to eliminate edge effects. The particle at the (ith, jth) position points in the θ_i, ϕ_j direction in geomagnetic coordinates:

$$\begin{aligned} \theta_i &= \theta + (i + x)0.5^\circ - 10^\circ \\ \phi_j &= \phi + ((j + x)0.5^\circ - 10^\circ)/\cos(\theta) \end{aligned} \tag{7.3}$$

where θ and ϕ are the geomagnetic coordinates of the Moon and x is a gsl random number $x \in$[-0.5,0.5].

7.2.2 Choosing the step length

A particle is tracked numerically solving the differential equation of motion

$$\frac{d\vec{v}}{dt} = \frac{q}{\gamma m}\vec{v} \times \vec{B} \tag{7.4}$$

The accuracy of the the solution is determined by the numerical algorithm used and the step size. In propagating the particle, the trajectory would be perfectly described with an infinite number of steps. However, we wish to accurately describe the trajectory with a finite computing time. The error introduced by a finite step size is a function of the product of force and step size, and since all other parameters are fixed this is a product of B and step size.

We therefore solved for step time Δt by restricting:

$$|\vec{B}_{initial} + \vec{B}_{final}||\vec{\Delta r}| \tag{7.5}$$

to lie between limits of 0.5 Tm$<\vec{B} \cdot \vec{r}<$0.6 Tm. The maximum time step was also set to 0.001 s. These limits were found from tests with the MC to optimize computational time whilst retaining accuracy.

7.2.3 Modified Stoermer method

At each time step the displacement, velocity and acceleration are used to find the particle position. A standard method for this kind of numerical integration in dynamics is the Stoermer method, modified by Henrici [99], which averages the velocity and acceleration between two displacements. However, in this case we have magnetic fields so velocity is not independent of acceleration. A modified method was therefore used in this simulation.

The total time step Δt between one step and the next is divided into 20 sub-steps of size h=Δt/20. The initial displacement $\vec{\Delta}^0$ in terms of the initial position and velocity vectors, $\vec{y^0}$ and $\vec{v^0}$ is $\vec{\Delta}^0 \equiv h\,[\vec{v}^0 + 1/2h\vec{a}\,(\vec{y}^0, \vec{v}^0)]$. We then take the 20 time sub-steps:

$$\vec{y}^k = \vec{y}^{k-1} + \vec{\Delta}^{k-1} \tag{7.6}$$

$$\vec{v}^k = \vec{\Delta}^{k-1}/h + 1/2h\vec{a}\left(\vec{y}^{k-1}, \vec{v}^{k-1}\right) \tag{7.7}$$

$$\vec{\Delta}^k = \vec{\Delta}^{k-1} + h^2\vec{a}\left(\vec{y}^k, \vec{v}^k\right) \tag{7.8}$$

The final velocity, after time Δt, is then $\vec{v}^{20} = \left(\vec{\Delta}^{19} + \vec{\Delta}^{20}\right)/2h$.

7.2.4 Outcomes of tracking

There are three possible outcomes of tracking the particle:

- The particle may reverse direction and hit the Earth. These particles coming from the Moon direction would be deflected away by the geomagnetic field and would not reach Milagro.
- It may get trapped in the field and time out after a total propagation time of 4 s. Light reaches the Moon in $\sim$1.3 s, so particles that have been traveling for more than 4s are assumed to have been trapped in the field.
- The particle may reach the Moon distance from the Earth.

If the particle reaches the Moon distance it is kept, all other outcomes are discarded; these particles would not reach Milagro. The initial trajectory direction is the true arrival direction –not the direction measured by Milagro. The Milagro

Point Spread Function (PSF) is then used to simulate the arrival direction that would be measured by Milagro (see sec. 7.5).

A particle that reaches the Moon distance may or may not have hit the Moon. Only particles that do not hit the Moon will be detected by Milagro. The remaining particles are shadowed. Both sets of particles are weighted by the effective area (see sec. 7.4) and recorded in two separate Moon-maps. In fact, to save computational time, particles with zero effective area are discarded before tracking.

7.2.5 Comparison with an Independently Developed Monte Carlo

This Monte Carlo originally developed by Allen Mincer was compared to an independent version developed Bob Ellsworth in [100]. After agreeing on the positions of the Moon and Milagro in their coordinate systems, protons were fired at the Moon. The differences in RA and dec were found upon arrival at the Moon distance. At 100 GeV the difference was $0.009^\circ \pm 0.007^\circ$ in RA and $0.009^\circ \pm 0.01^\circ$ in dec and at 1 TeV the difference was $0.01^\circ \pm 0.06^\circ$ in RA and $0.03^\circ \pm 0.04^\circ$ in dec. As the two Monte Carlos were independently developed we consider this a reasonable check of the methods.

7.3 Milagro Simulated Data

Both the effective area and point spread function were found using Milagro simulated data sets. For this Monte Carlo the simulated data used was with no air

under the cover, during epoch 9. Simulated data files for epochs 7 and 8 were tested and no significant difference was found. The Milagro simulated data is described in sec. 3.6.

7.4 Effective Area

The effective area models Milagro's response to each species of cosmic rays, and is a strong function of both energy and zenith angle. Since this determines the likelihood of a particle shower to be detected by Milagro it is used to weight the skymaps centered on the Moon after the particles have been tracked.

The effective area is determined from simulations by

$$A_{\text{eff}}(E,\theta) = \frac{N_{trig}(E,\theta)}{N_{throw}(E,\theta)} A_{throw} \tag{7.9}$$

where $N_{trig}(E,\theta)$ and $N_{throw}(E,\theta)$ are the number of events triggering, and initially thrown, respectively, in a given energy and reconstructed zenith angle bin.

The energy was binned logarithmically, with 5 bins for each decade in energy. The reconstructed zenith angle was in bins of 3°. The bin sizes were chosen to include the finest binning possible, whilst keeping enough statistics to model the strong dependence of effective area on both zenith angle and energy. The proton effective area for six 10° zenith angle bins is shown in fig. 7.2 and the same binning for the remaining heavy species in fig. 7.3.

7.4.1 Binning in frasor

Each event has a probability of falling into any given bin of FRASOR, reconstructed zenith angle and energy. However this probability fsr_{wt} is simply

$$\mathrm{fsr}_{wt}(\mathrm{fsr}, E, \theta) = \frac{N_{trig}(\mathrm{fsr}, E, \theta)}{N_{total}(E, \theta)} \tag{7.10}$$

where N_{total} is the total number of events passing the overall zenith and N_{fit} cut

$$N_{total} = \iiint N_{trig}\,(\mathrm{fsr}, E, \theta)\ \mathrm{d}(\mathrm{fsr}) \tag{7.11}$$

When the Moon MC Moon-maps are being made, each particle then comes with this additional weight, which is cumulatively multiplicative with the effective area weight.

7.5 Milagro Point Spread Function

The particles that are tracked to the Moon distance, when they leave on their path to the Moon, point in their true arrival direction. This is not the direction measured by Milagro. To find the reconstructed particle direction we need to model the Milagro point spread function (PSF), which differs based on the species, energy and zenith angle of the particle.

The Milagro PSF is modeled by Δ_{ang}; the difference between reconstructed and true direction using the Milagro simulated data.

$$\Delta_{ang} = |\Omega_{true} - \Omega_{recon}| \tag{7.12}$$

The distribution of Δ_{ang} is well described by a double radial gaussian of the form

$$F\,(\Delta_{ang}) = A\ \Delta_{ang}\left(e^{\left(-\Delta^2_{ang}/2\sigma_1^2\right)} + R\ e^{\left(-\Delta^2_{ang}/2\sigma_2^2\right)}\right) \tag{7.13}$$

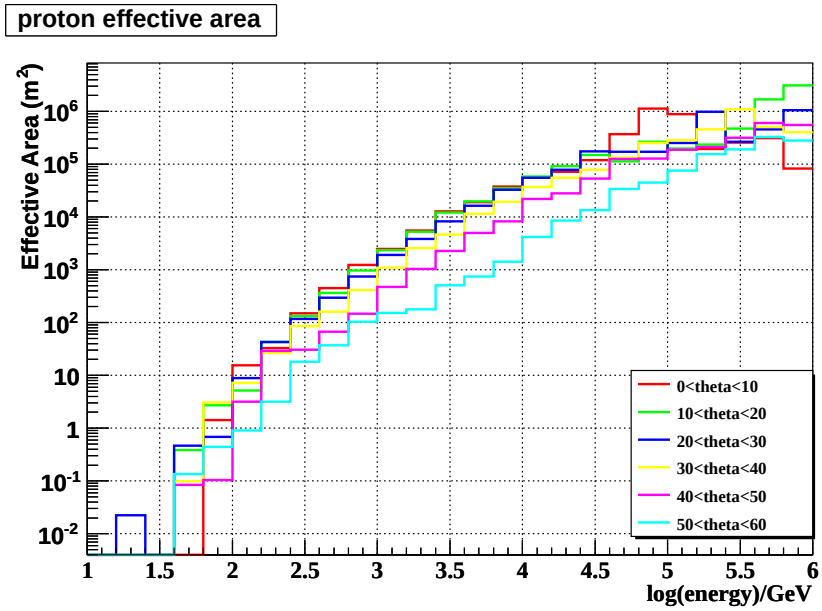

Figure 7.2: Milagro effective area with standard cuts for protons with N_{fit}>40 for different zenith angle cuts.

After cuts in energy, reconstructed zenith angle, and reweighting in the Milagro simulated data, the Δ_{ang} distribution is fit to $F(\Delta_{ang})$. The four fit parameters A, R, σ_1 and σ_2 fully describe the PSF for those cuts. The data is binned in 3 log(energy) bins per decade of energy and 15° true zenith angle bins. If the uncertainty on A, σ_1 or σ_2 is more than 10% or on R is more than 50% the data is added to the next bin and the fit is done again until the fit parameters are good. This iterative process is done first in energy bins, then true zenith angle bins. The F(Δ_{ang}) fit with standard data cuts for all species shown in fig. 7.4.

To simulate the Milagro reconstructed direction for a given particle in the Moon MC we need the energy, true zenith angle, FRASOR and three gsl random numbers

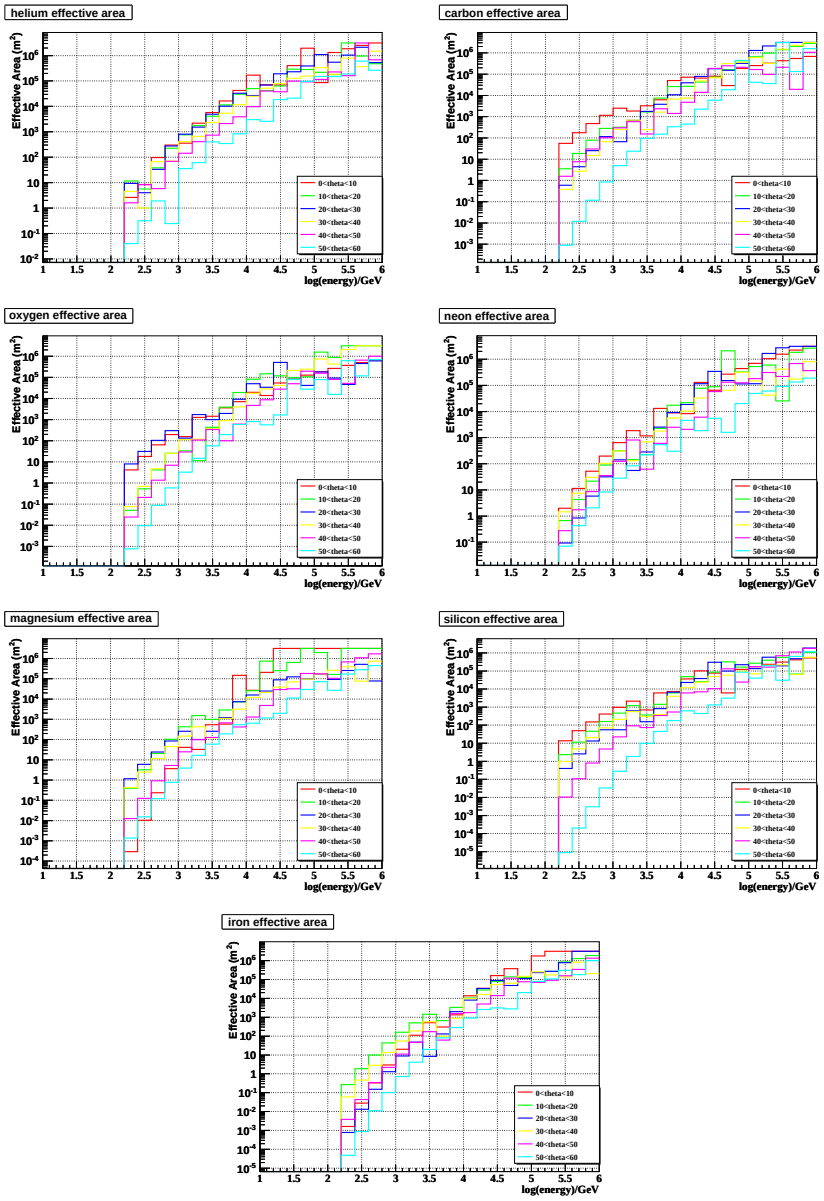

Figure 7.3: Milagro effective area with standard cuts N_{fit}>40 for different zenith angle cuts and species.

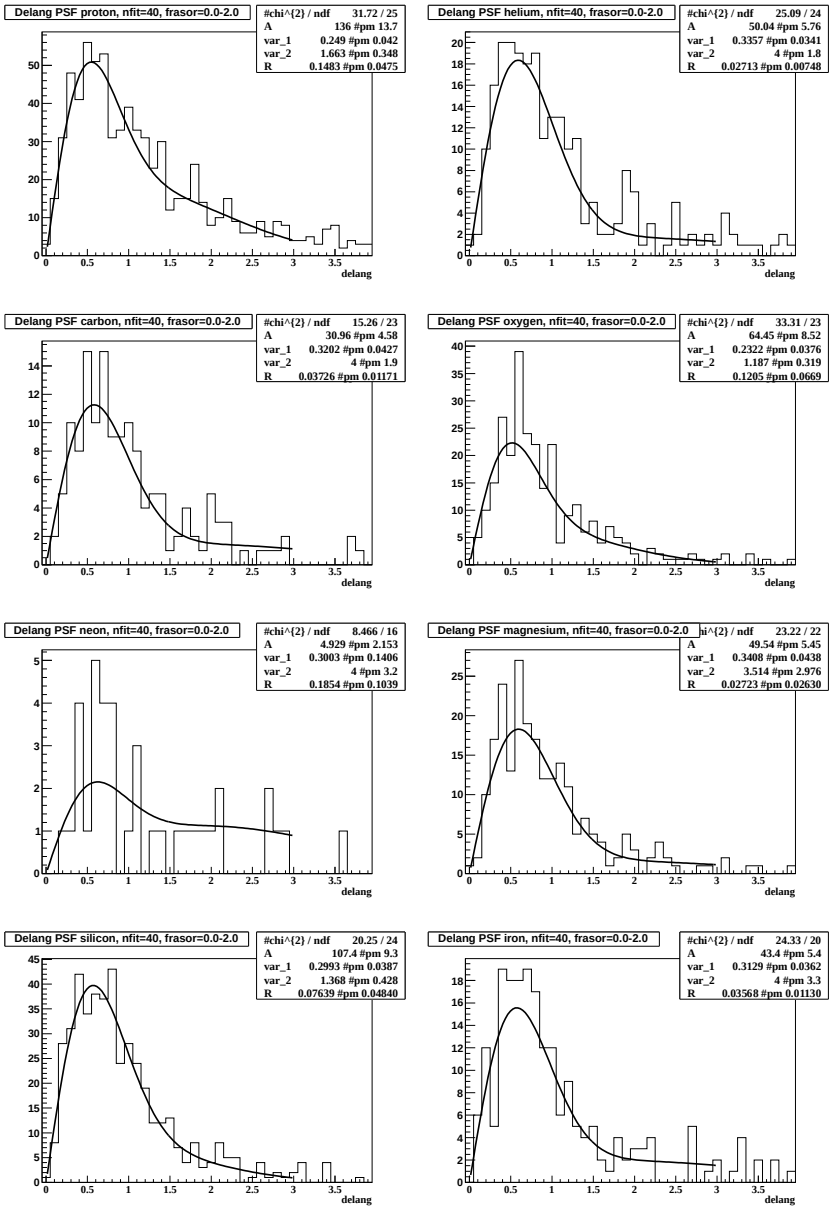

Figure 7.4: The Δ_{ang} distribution, fit to radial double gaussian for all species with N_{fit}>40 and zenith angle<60° cuts. The fit parameters displayed are amplitude, variance and the ratio of the amplitudes of the two radial gaussians.

x_1, x_2, x_3 $\in$[0,1]. From the energy, true zenith angle and FRASOR we get the fit parameters from $F(\Delta_{ang})$ for that bin. The function $F(\Delta_{ang})$ is comprised of two radial gaussians, a narrower dominant gaussian and a second minor gaussian with a longer tail. The integral is equal to

$$\int_0^\infty F\left(\Delta_{ang}\right)\,\mathrm{d}\Delta_{ang} \;=\; A\sigma_1^2 + R\sigma_2^2 \tag{7.14}$$

so the first random number can choose between the two gaussians. If $x_1 < \sigma_1^2/\left(\sigma_1^2 + R\sigma_2^2\right)$ then we choose the first gaussian, otherwise we choose the second. The integral of $\Delta_{ang}e^{\left(-\Delta^2/2\sigma_1^2\right)}$ may be evaluated directly so with a second random number one can find

$$\Delta_{ang,0} = \sigma\sqrt{\left(-2\log\left(1-x_2\right)\right)} \tag{7.15}$$

Where $\Delta_{ang,0}$ is the size of the displacement in the 2-D plane. The final random number then assigns $\Delta_{ang,0}$ along the geomagnetic axes

$$\begin{aligned}\Delta_{ang,\alpha} &= \Delta_{ang,0}\;\cos\left(2\pi\;x_3\right)\\ \Delta_{ang,\delta} &= \Delta_{ang,0}\;\sin\left(2\pi\;x_3\right)\end{aligned} \tag{7.16}$$

Then the reconstructed angles are given by

$$\begin{aligned}\alpha_{recon} &= \alpha_{true} + \Delta_{ang,\alpha}/\cos(\delta_{true})\\ \delta_{recon} &= \delta_{true} + \Delta_{ang,\delta}\end{aligned} \tag{7.17}$$

7.6 Uncertainties

There are systematic uncertainties associated with spectra and flux—which are correlated—and also with the effective area and angular resolution. Additionally,

there is a systematic uncertainty from the FRASOR-weight for each particle in a FRASOR bin, which is correlated with the effective area uncertainty.

The Moon-maps are actually made in a way that differs slightly from the method described above. After tracking particles, events that reached the Moon distance are recorded in a data file. What is kept is the species, energy, whether the particle hit the Moon, true particle direction in geomagnetic coordinates, time and random number iteration. Particles are also kept for lower energy scales for an use in calibration. This collection of data allows variation of parameters to generate new Moon-maps whilst saving on computing time. Therefore, in the data files the random number iteration is included, which keeps track of all the information about a particle. In total, for each 10 s time step there are 2+41×41×4 gsl random numbers. The first two are for the energy and species, then for each of the 41×41 particles on the grid there is a random number to vary the direction, and three for angular resolution. Even when events are discarded before tracking, the full set of random number iterations are calculated to allow keeping identical events for systematic studies.

7.6.1 Uncertainties from Spectra and Flux

To find the uncertainties from spectra and flux, the uncertainties in the fits $\sigma(\alpha)$ and $\sigma(F_0)$ in fig. 7.1 are varied with gaussian statistics

$$\begin{aligned} \alpha' &= \alpha + N\sigma(\alpha) \\ F_0' &= F_0 + N\sigma(F_0) \end{aligned} \tag{7.18}$$

where N$\in[-\infty, \infty]$ is found from gaussian distribution.

Using ten distinct sets of α' and F_0' we produce ten new Moon-maps. Both the energy of the particle and species are functions of the flux and spectra. Therefore each species is re-weighted in the Moon-maps by a new fraction, spectra_{wt}, simultaneously as the energy is re-weighted by energy_{wt} using the spectral indices:

$$\begin{aligned} \text{spectra}_{wt} &= f_i / f_{i,0} \\ \text{energy}_{wt} &= E^{\alpha_{i,0} - \alpha_i} \end{aligned} \tag{7.19}$$

where f_i is the fraction of species i from eq. 7.1 with the new and original spectra and fluxes respectively, $\alpha_{i,0}$ is the original spectral index of species i, α_i is the new spectral index of species i and E is the energy. These weights are cumulatively multiplicative with the effective area when filling Moon-maps.

7.6.2 Uncertainties from effective area and frasor-weight

For the effective area and FRASOR-weight uncertainties, if effective area is given by eq. 7.9, then the binomial error is of the form np(1-p), so the uncertainty is

$$\sigma\left(A_{eff}\left(E,\theta\right)\right) = \frac{A_{eff}\left(E,\theta\right)}{A_{throw}}\left(1 - \frac{A_{eff}\left(E,\theta\right)}{A_{throw}}\right) A_{eff}\left(E,\theta\right) \tag{7.20}$$

The uncertainty in the FRASOR weighting takes the same np(1-p) form

$$\sigma\left(\text{fsr}_{wt}\left(\text{fsr},E,\theta\right)\right) = \frac{N_{trig}\left(\text{fsr},E,\theta\right)}{N_{total}}\left(1 - \frac{N_{trig}\left(\text{fsr},E,\theta\right)}{N_{total}}\right) N_{trig}\left(\text{fsr},E,\theta\right) \tag{7.21}$$

These 1-σ uncertainties are gaussian varied using a random number for each bin to produce a new effective area and FRASOR-weight.

$$\begin{aligned} A'_{eff} &= A_{eff} + N\sigma\left(A_{eff}\right) \\ \text{fsr}'_{wt} &= \text{fsr}_{wt} + N\sigma\left(\text{fsr}_{wt}\right) \end{aligned} \tag{7.22}$$

where N is a number from a gaussian distribution. The same Moon-maps are then reproduced ten times with ten pairs of new effective area and FRASOR-weight.

7.6.3 Statistical Uncertainty

The gsl random number package will produce the same string of random numbers for a given seed. The statistical error Moon-maps can then be found using a different random number seed. Due to the large computing time necessary, three maps in total are generated to test the spread due to using a different random number. The number of particles in these maps were chosen to ensure that the statistical uncertainties were small compared to other errors. Note that the number of events in the statistical runs, i.e. every 10 s, does not have to be the same as the event totals for the other uncertainties. As long as the random number iteration is tracked, the statistical uncertainties are decoupled from the systematic uncertainties, which would remain the same order if the number of events was increased by a factor of ten.

7.7 Moon centered Skymaps with the Moon Monte Carlo

The Moon Monte Carlo map, which is the equivalent of an excess-map in data is shown in figure 7.5. The map is unsmoothed, with no FRASOR cut and N_{fit}>40. It shares similar features to the data excess-map, but it should be noted that the Moon Monte Carlo is designed to reproduce the shape and position of the Moon

shadow, but not the event rate of Milagro, so the total number of missing events, the absolute event depth of the shadow and the excess events do not match the data.

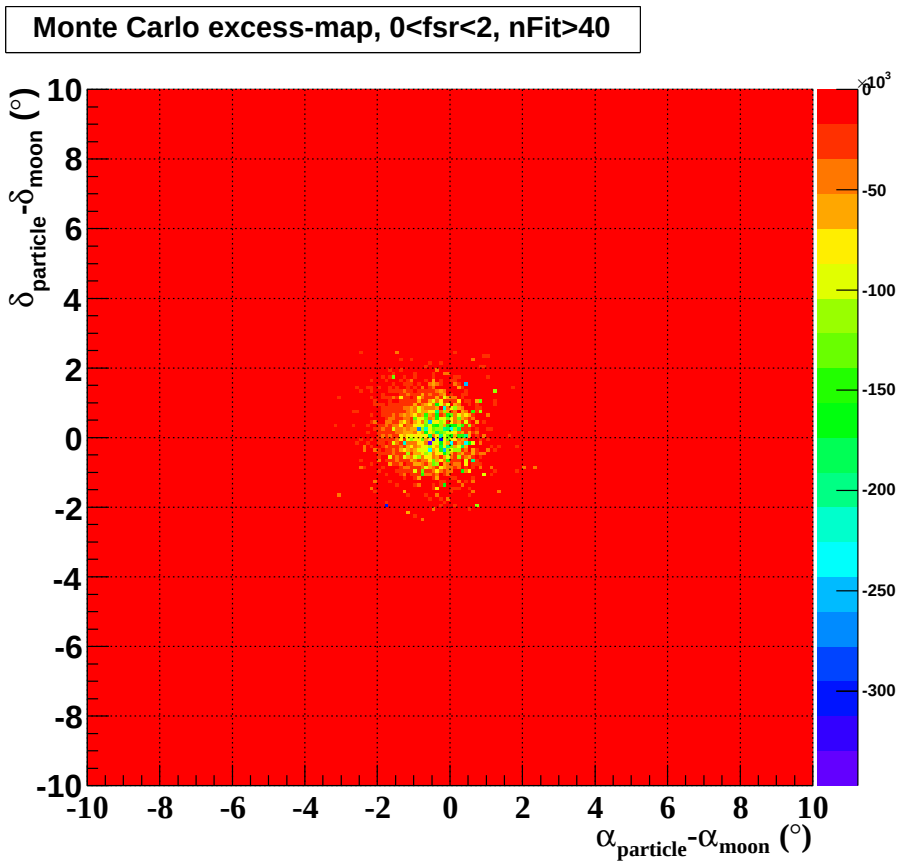

Figure 7.5: Moon Monte Carlo excess-map with no FRASOR cut, N_{fit}>40 zenith angle>60° cuts.

7.7.1 Integrated and Differential Fractional Deficits

The integrated and differential fractional deficit plots, in RA, dec, particle minus Moon coordinates, are shown in fig. 7.6. The plots are centered on the fitted Moon shadow position, where the Moon shadow is fitted to a 2-D gaussian, as described in sec. 6.4. In both plots a value of one on the y-axis represents recovering all shadowed particles. The integrated plot is not required to have an asymptote of one as points on both the differential and integrated plots are weighted by a multiplicative geometric factor described in the next section.

The integrated plot error bars are correlated from point to point and the differential error bars are not. For the Moon MC the integrated plot is found from the summing effective area weighted map of shadow particles. All particles within circular area with radius indicated on the x-axis are counted, in steps of 0.1° beginning at 0.05° where 0.1° is the resolution of the Moon-maps in data. This is then divided by the total number of shadowed particles and multiplied by the factor shown above. The differential plots are found from the annuli rather than area.

7.7.2 Moon Geometrical Factor

This geometrical factor, 0.234 is calculated in the Moon MC and represents the effective geometrical area of the Moon in RA-dec coordinates, integrated over the same period of time as the Moon MC and data. It can be considered as the fraction of 1° square the Moon takes up on average over the period of the Moon MC, with a slight distortion from the coordinate system used.

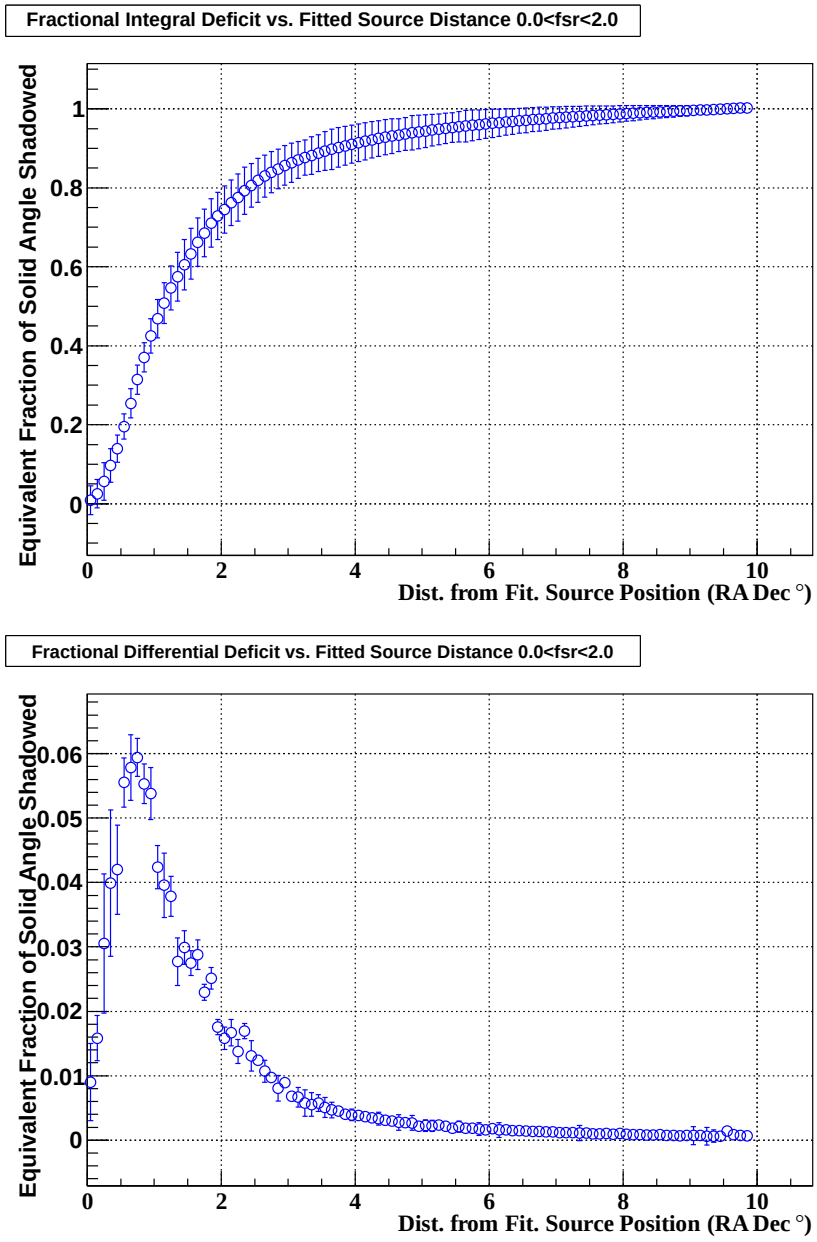

Figure 7.6: Integrated and differential fractional deficit plots of the Moon for N_{fit}>40 zenith angle>60° cuts.

The factor is:

$$\text{factor} = \frac{\text{total \# shadowed particles}}{\text{\# shadowed} + \text{unshadowed particles in central } 1^\circ \text{ square}} \tag{7.23}$$

The factor is calculated with the magnetic field turned off, but retaining the PSF. The Moon shadow is deflected by the magnetic field, and the effective area is a strong function of zenith angle, so the geometrical area of the true shadow differs from the geometrical factor. Even after angular smearing from the PSF the Moon shadow is deflected to a higher dec on average. This corresponds, on average to higher zenith angles. Therefore, we expect the integrated fractional deficit plots to plateau slightly above 1.

7.7.3 The frasor binned Moon MC

In figures 7.7, 7.8 and 7.9 are the FRASOR binned plots for the Moon MC, of the unsmoothed excess-maps alongside the integral and differential fractional deficits. The plots show the same general trend as the data shadows, and it should be noted that FRASOR$>$ 1.4 bins have extremely low statistics, so have difficulty in fitting a 2-D gaussian.

7.7.4 2-D Gaussian fit Parameters in frasor bins

The fit parameters of eq. 6.1 for ten FRASOR bins are shown in fig. 7.10. We expect the magnetic deflection of cosmic rays to be primarily along RA, which is indeed the case. We also have larger deflections for lower FRASOR bins as expected. Along dec the position of the shadow is not consistent with zero, but is smaller than the

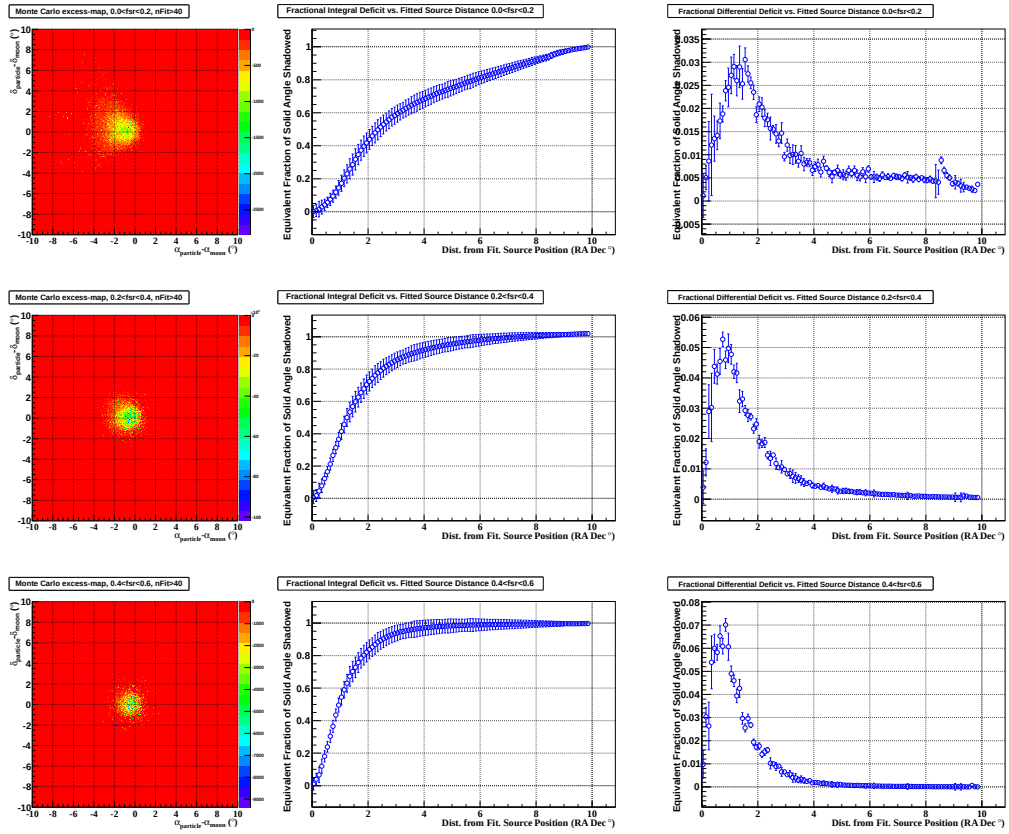

Figure 7.7: Moon-maps for MC in the lowest 3 FRASOR bins. Top 0.0<FRASOR<0.2, middle 0.2<FRASOR<0.4 and bottom 0.4<FRASOR<0.6, with cuts N_{fit}>40 and θ<60°. Note the lowest FRASOR bin differential deficit doesn't quite average at zero at 10°. This is because some of the low energy particles have, after smearing the arrival direction with the PSF, been deflected beyond 10°.

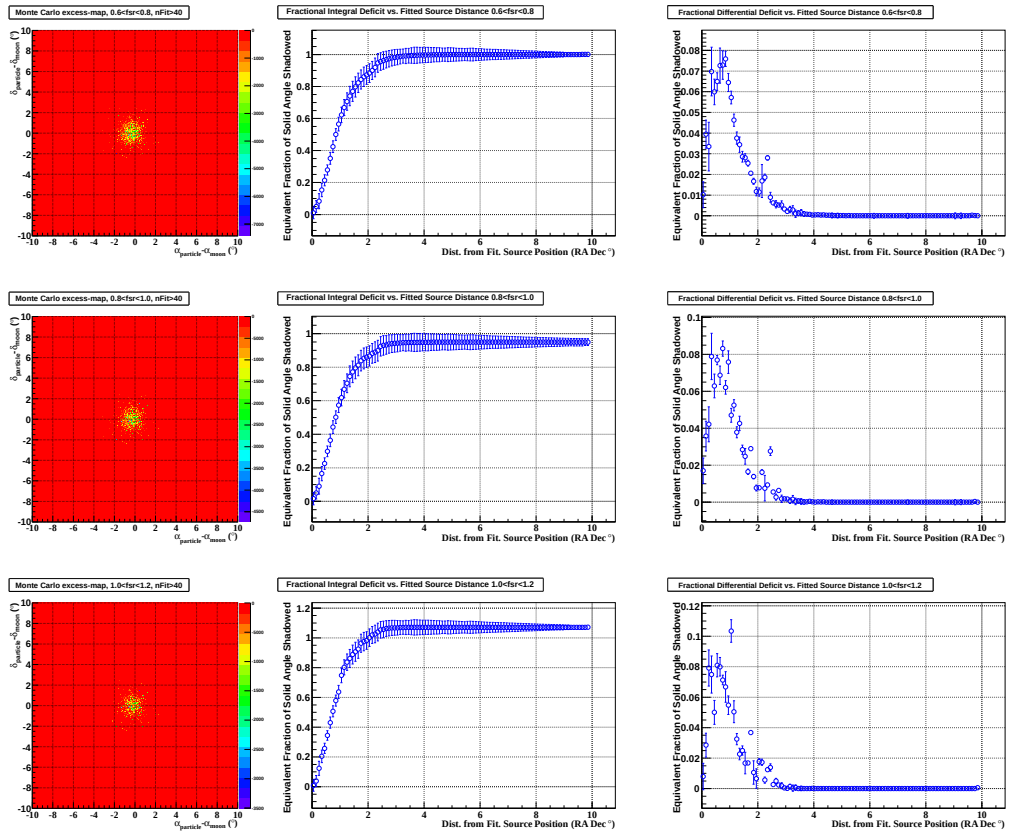

Figure 7.8: Moon-maps for MC in the middle 3 FRASOR bins. Top 0.6<FRASOR<0.8, middle 0.8<FRASOR<1.0 and bottom 1.0<FRASOR<1.2, with cuts N_{fit}>40 and θ<60°.

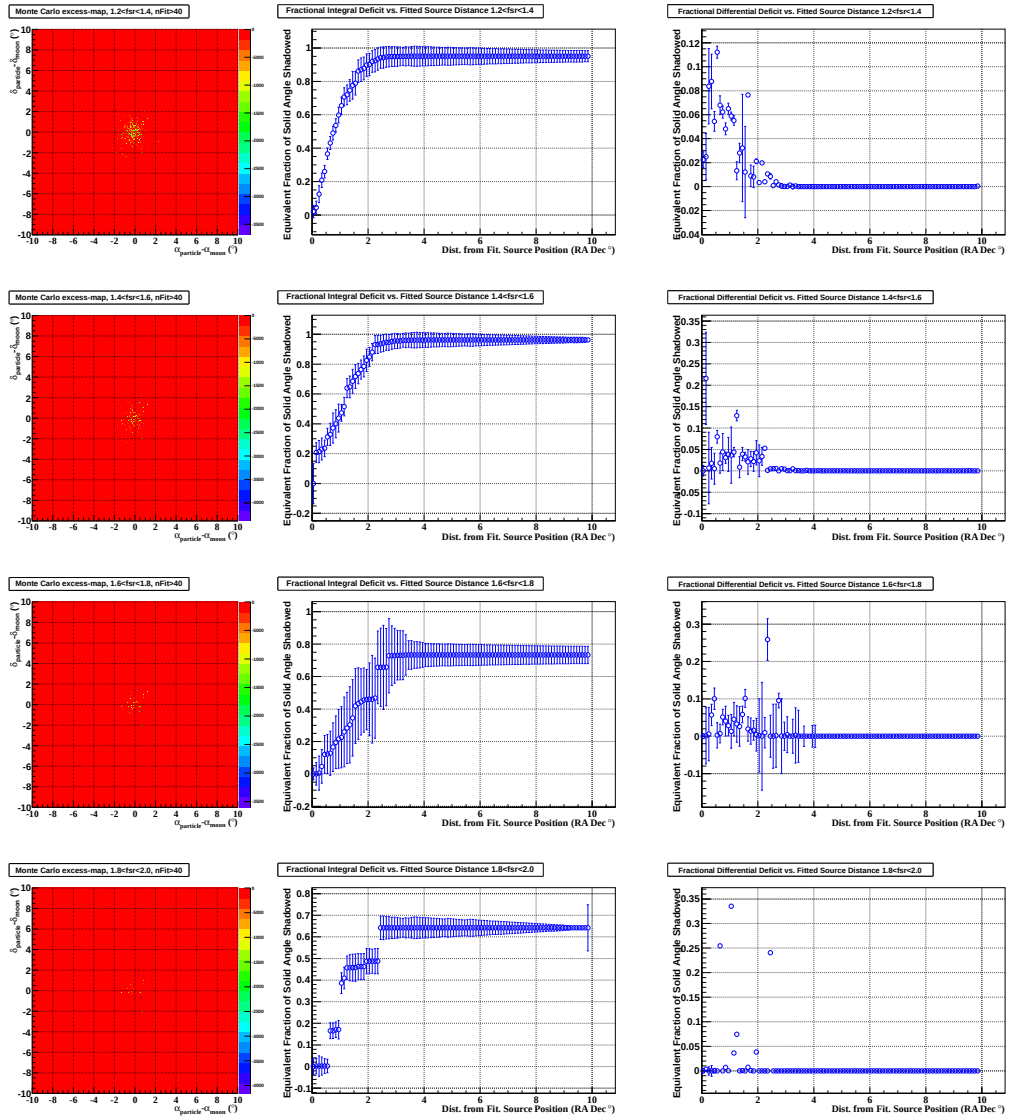

Figure 7.9: Moon-maps for MC in the highest 4 FRASOR bins. Top 1.2<FRASOR<1.4, second 1.4<FRASOR<1.6, third 1.6<FRASOR<1.8 and bottom 1.8<FRASOR<2.0, with cuts N_{fit}>40 and θ<60°.

deflection along RA for low FRASOR bins. The widths also decrease in both RA and dec with increasing FRASOR bin, as expected.

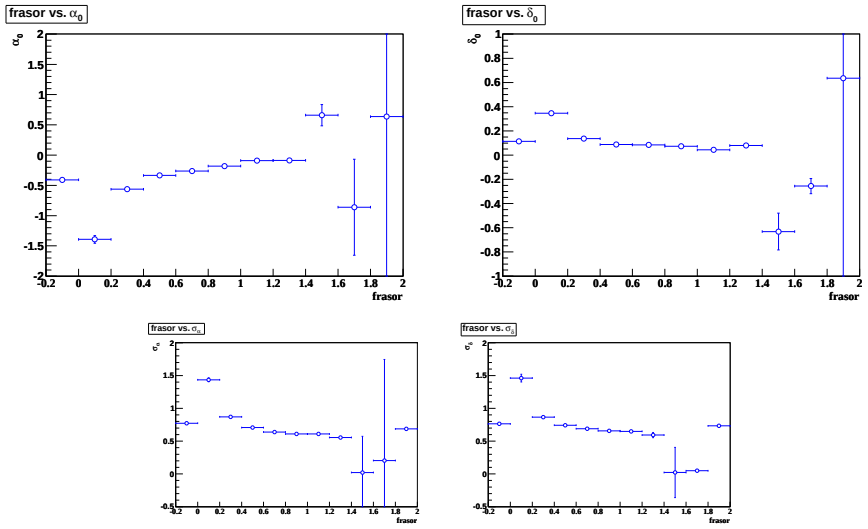

Figure 7.10: Fit parameters from 2-D gaussian in FRASOR bins for the Moon MC. The plots are shadow position along RA and dec respectively. The negative bin is the full set of events with no FRASOR cut.

As expected from the excess-maps in figures 7.7, 7.8 and 7.9, the highest three FRASOR bins do not have sufficient statistics for a good 2-D gaussian fit to the shadow.

The widths in both RA and dec directions are nearly equal, even for low FRASOR bins. One would expect that the width of the shadow along the dec axis would be almost a pure convolution of the Milagro PSF with the Moon as a disc-shaped sink for cosmic rays. In contrast one would expect that along the RA axis the width would contain information about the geomagnetic field which would extend

the width of the shadow in that direction. As a result we would expect an elliptical shadow, particularly for low FRASOR bins, with the major axis along RA. From looking at the fitted shadow position along the RA axis we are clearly very sensitive to the geomagnetic field deflection so it is perhaps surprising not to see this effect in the shadow width.

Chapter 8

A Study of the Possibility of an Energy Calibration of Milagro using the Cosmic-Ray Moon Shadow

Air shower arrays have been operating for 50 years and to date have all relied solely on EAS and detector simulations to calibrate their energies. In this chapter, we describe an attempt at the first such calibration using the cosmic-ray Moon shadow. To do this we need both the shadow in data from chapter 6 and from Monte Carlo in chapter 7.

We proceed as follows: in section 8.1 we discuss the definition of energy scale and how to vary the energy scale of the Moon MC in practice. In section 8.2 we compare the shadow generated from the Moon MC to the shadow from data using

the 2-D gaussian to model the shadow. Then in section 8.3, we compare the data with Moon MC shadows in FRASOR bins generated with different energy scales, again using the 2-D model. In section 8.4 rather than compare the gaussians of data and Monte Carlo, we compare the projections of the Moon shadow along the RA and dec directions. Finally, in section 8.5 we discuss uncertainties in the Moon Monte Carlo that were not quantified in chapter 7.

8.1 Monte Carlo Energy Scale

A particle energy E is rescaled to E′ where

$$E' = xE \tag{8.1}$$

Rescaling the energy, for instance when x=0.5, means that each particle is being scaled to a lower effective area. The particle was deflected in the magnetic field as a particle of energy E, but is detected by Milagro as a particle E′=0.5 E. That is, the effective area of the particle is lowered.

Suppose we found that particles of energy E′=1.2 E generated the Moon MC shadow that was the best match to the data shadow. These particles were deflected by the magnetic field with their true energies, and hence rigidities. Then these particles are detected by Milagro, but Milagro is under-estimating their effective area. Milagro would be said to be incorrect in energy scale by 20%, and would be under-estimating cosmic-ray energies by 20%.

How could this be possible? Milagro has been very carefully been calibrated by the collaboration, using simulated data, as discussed in sec. 3.6. But this is exactly

where the uncertainty arises from. The combination of the models of the EAS using CORSIKA, and the detector simulation using GEANT4 could be causing Milagro to over (or under) estimate its effective area function.

There are two possible methods to vary the energy scale in the Monte Carlo. In the first, using the dipole model described in sec. 4.3.1, we can vary the strength of the dipole and re-propagate the particles to the Moon. Alternatively, we can scale the energy of each particle by the inverse of the same factor. We take the second approach, as re-tracking the particles requires significantly more computational time. Rescaling the energy has the following effects:

- A particle energy E' will fall into a new effective area bin.
- The particle will fall into a different PSF bin.
- The energy must be re-weighted due to the spectrum, by a factor $E'^{-\alpha}/E^{-\alpha}$. This is $x^{-\alpha}$, so with a higher energy scale ($x>1$) the energy weighting is smaller than one, and the energy weighting is greater than one for a lower energy scale ($x<1$).
- If we are FRASOR binning the data the particle will now have a different probability of falling into a FRASOR bin.

8.2 Comparison of Data and Monte Carlo for the Moon's Shadow

The data and Monte Carlo maps generated are both over the period of epochs 7-9, with cuts N_{fit}>40 and zenith angle<60°, as seen in chapters 6 and 7. In figure 8.1 are the integrated and differential fractional deficit plots for the Moon shadow for data and Moon MC with and uncorrected energy scale (x=1.0). We see that the integrated plots from data and Moon MC both take the same shape, and they both plateau to one within error (which is correlated from point to point). The differential plot has uncorrelated errors and again the data and Monte Carlo agree fairly well, though not completely. From this perspective the uncorrected x=1.0 energy scale appears to be a good fit to the data.

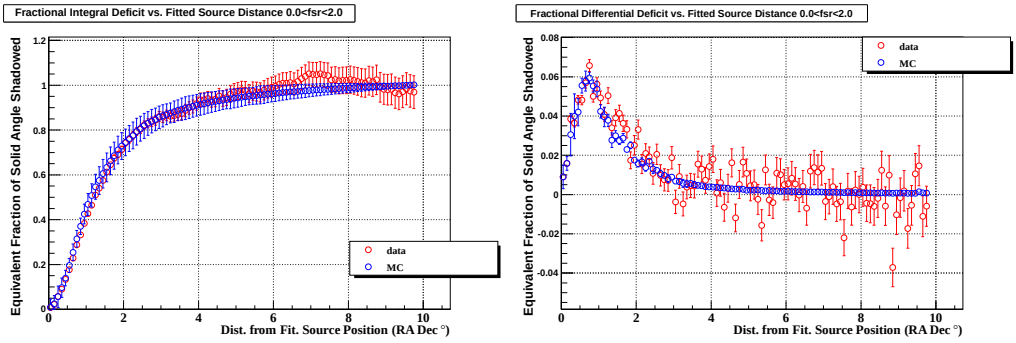

Figure 8.1: Integrated and differential fractional deficit plots for data and Monte Carlo of the Moon. Cuts are N_{fit}>40, zenith angle<60°.

In table 8.1 are the parameters from the 2-D gaussian fit from eq. 6.1 to the Moon shadow, for data and 8 energy scales between x=2.0 and x=0.5. In the dec

x	$\alpha_0(^\circ)$	δ_0 $(^\circ)$	σ_α $(^\circ)$	σ_δ $(^\circ)$
data	-0.265+/-0.019	0.106+/-0.016	0.919+/-0.021	0.779+/-0.018
2.0	-0.488+/-0.033	0.113+/-0.010	0.819+/-0.010	0.787+/-0.016
1.5	-0.442+/-0.032	0.114+/-0.010	0.798+/-0.009	0.772+/-0.015
1.3	-0.423+/-0.032	0.106+/-0.010	0.780+/-0.009	0.778+/-0.015
1.1	-0.387+/-0.032	0.111+/-0.010	0.765+/-0.008	0.775+/-0.014
1.0	-0.408+/-0.034	0.114+/-0.012	0.773+/-0.010	0.764+/-0.015
0.9	-0.367+/-0.032	0.083+/-0.011	0.752+/-0.007	0.776+/-0.014
0.8	-0.348+/-0.032	0.077+/-0.011	0.729+/-0.008	0.758+/-0.015
0.5	-0.247+/-0.031	0.054+/-0.011	0.703+/-0.006	0.730+/-0.014

Table 8.1: Fit parameters for a 2-D gaussian (eq. 6.1) fit to the Moon shadow from data and Monte Carlo from various energy scales.

direction we are modeling the shadow very well. For δ_0, energy scales $1.0< x <2.0$ match the data within error bars, as do energy scales $0.8< x <2.0$ for σ_δ. In the RA direction the picture is more complicated, with only the energy scale x=0.5 agreeing with data shadow position. For the width of the shadow along RA the situation is worse as no energy scale matches the data.

8.2.1 The Convolution of the Energy Scale Parameter with Effective Area and PSF

The effective area of Milagro in protons (fig. 7.2), is steepest for lower energies, and plateaus for high energies. Doubling the energy scale for instance, has a smaller

effect on the effective area at higher energies than at lower energies. If the energy scale is doubled, low energy particles, having low rigidities, are deflected more than higher energy particles, which have high rigidities. When effective area weighted, increasing the energy scale of the lower energy particles has a greater effect than on the high energy particles, as the effective area is flatter at higher energies. Hence the Moon shadow appears to be deflected more along RA when the energy scale is increased.

The PSF of lower energy particles is broader, so as the particles are effective area weighted, the same argument applies and the PSF should increase. The σ_δ parameter then, should increase with a higher energy scale, x. The σ_α parameter is increased by the effective area, and increased by the PSF. Combining the these two effects, σ_α becomes broader with increasing energy scale, and compared to σ_δ, the RA width should be broader for the same energy scale.

8.3 Moon Monte Carlo and Data Comparison in frasor bins at different energy scales

We now compare the data and Moon MC at different energy scales in FRASOR bins. In figures 8.2, 8.3 and 8.4, 8.5 are the integrated fractional deficits and differential deficits in all FRASOR bins of the data and Moon MC.

The integrated and differential plots show the same features. The match is excellent for the middle FRASOR bins. However the match is bad for very high FRASOR bins. This isn't surprising as the high FRASOR bins have very low statis-

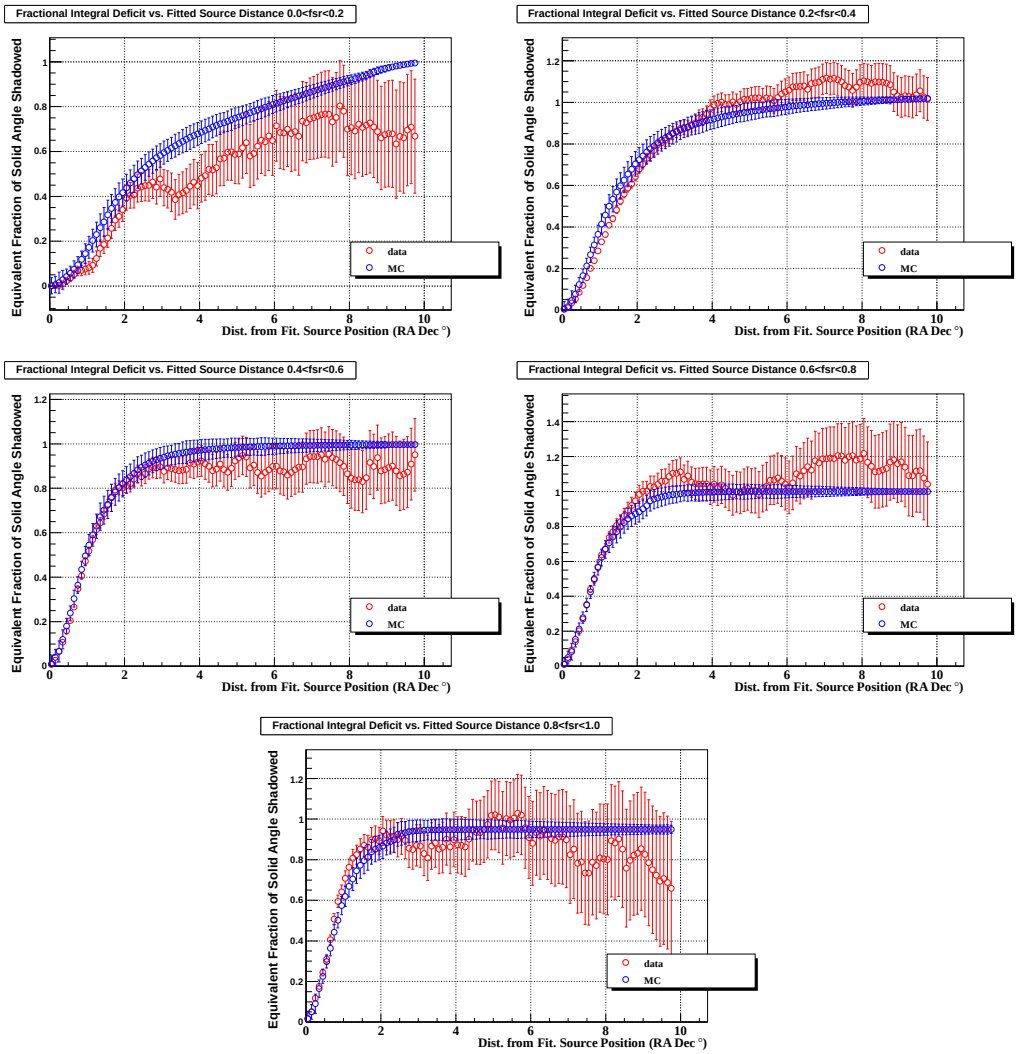

Figure 8.2: Integrated fractional deficit plots for data and Monte Carlo of the Moon for the lowest five FRASOR bins. Cuts are N_{fit}>40, zenith angle<60°.

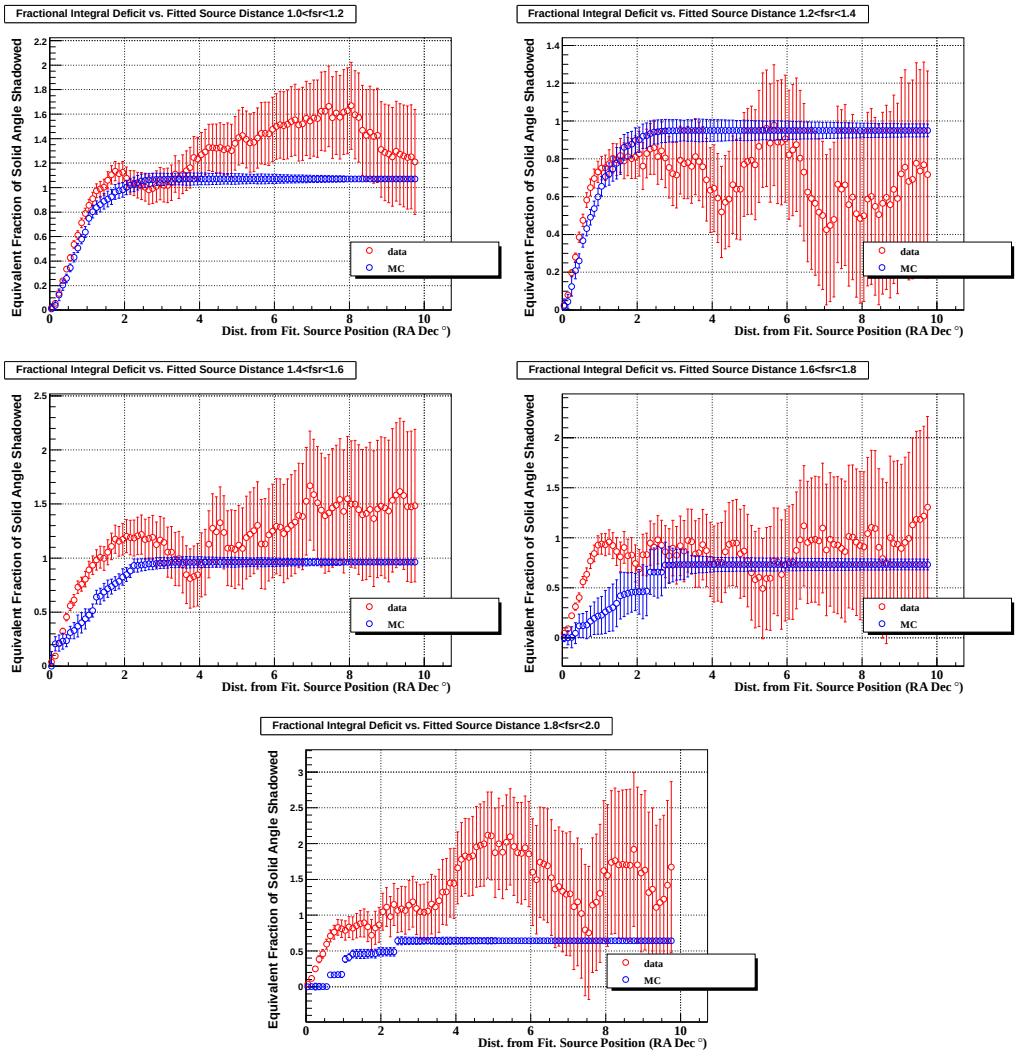

Figure 8.3: Integrated fractional deficit plots for data and Monte Carlo of the Moon for the highest five FRASOR bins. Cuts are N_{fit}>40, zenith angle<60°.

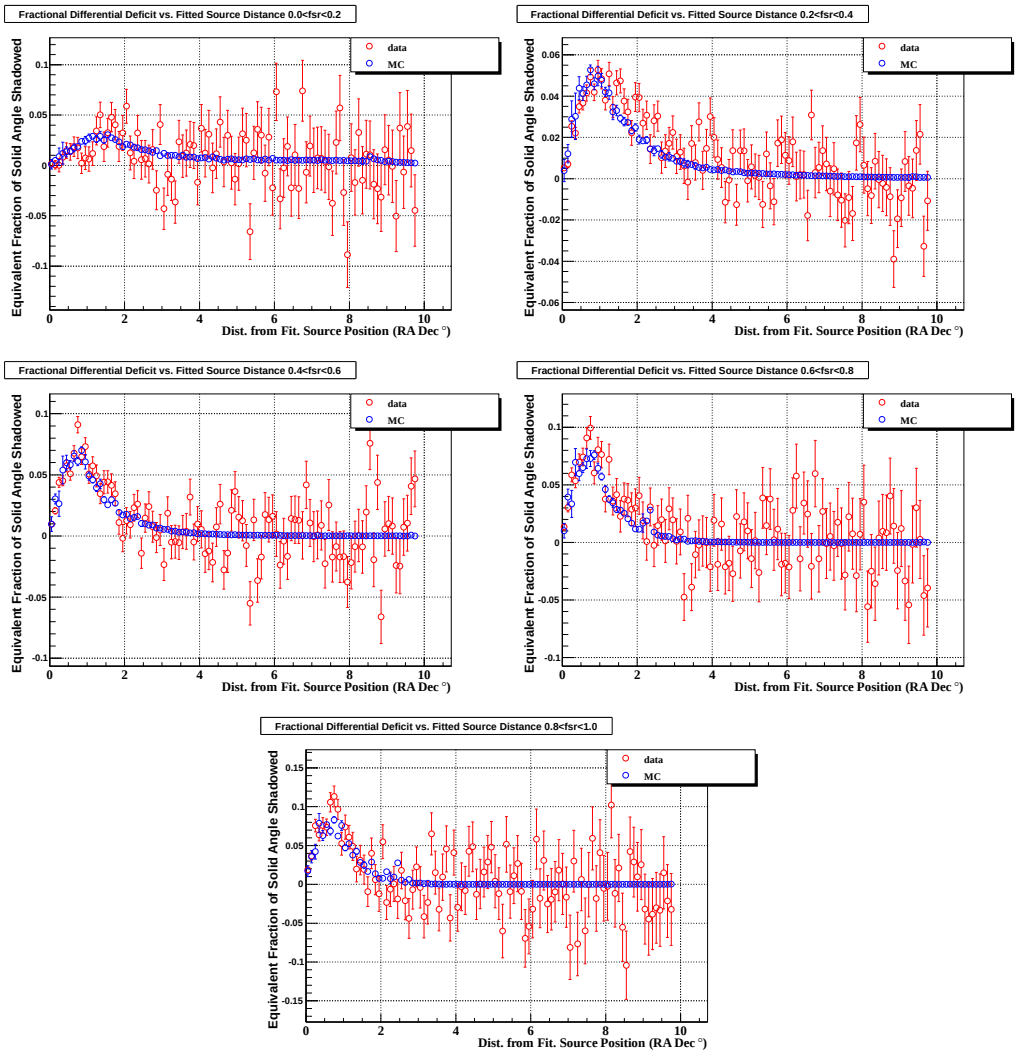

Figure 8.4: Differential fractional deficit plots for data and Monte Carlo of the Moon for the lowest five FRASOR bins. Cuts are N_{fit}>40, zenith angle<60°.

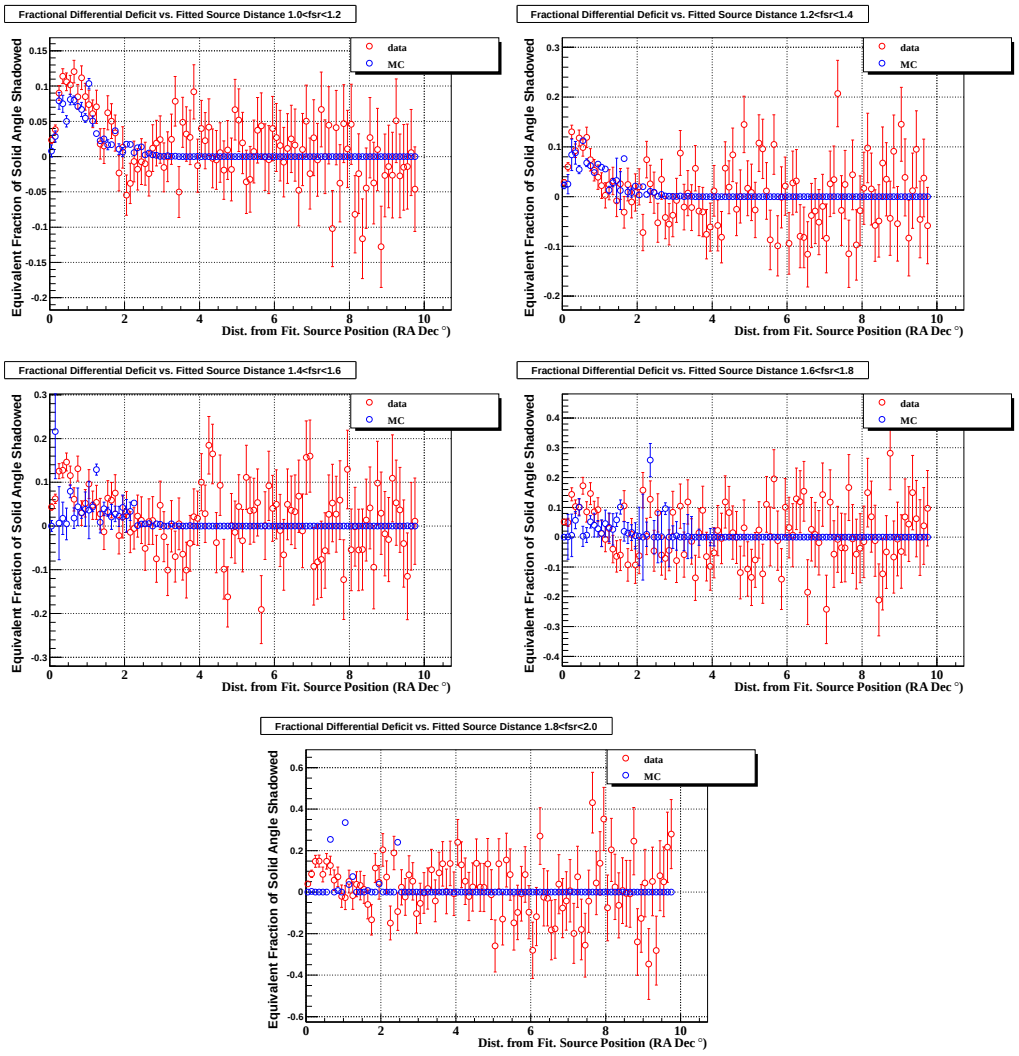

Figure 8.5: Differential fractional deficit plots for data and Monte Carlo of the Moon for the highest five FRASOR bins. Cuts are N_{fit}>40, zenith angle<60°.

tics, as can be seen in figure 7.9, so the fits do not capture the behavior well. The lowest 0<FRASOR<0.2 bin, though a good match here, is difficult to simulate correctly. The sensitivity of the energy threshold to effects from the weather results in variation in the energy of the events that fall into this bin. We therefore use 0.2<FRASOR<1.4 only in the rest of this analysis.

To find useful parameters for an energy calibration, we look at fit parameters of the 2-D gaussian from eq. 6.1. The fits for data and MC in all FRASOR bins are shown in figs. 8.6 and 8.7. For all FRASOR bins we are modeling α_0 and σ_α poorly. The Moon MC is under-estimating the width along RA and over-estimating the deflection along RA. However, the δ_0 and σ_δ parameters are being modeled very well. At this stage it seems possible that some other energy scale for the Moon MC shadow could be a better model for the data shadow.

We first look at the Moon MC at x=0.5 and x=2.0, corresponding respectively to Milagro over-estimating or under-estimating the energy scale by a factor of 2, to see if changing the Moon MC energy scale is behaving qualitatively in the manner we expect. The energy scales of x=0.5 and x=2.0 are compared to both data and x=1.0 in figures 8.8 and 8.9.

For x=0.5, particles are scaled to a lower energy, reducing their effective area. The positions of α_0 confirm this –for all FRASOR bins x=0.5 are deflected less than x=1.0. For δ_0 in higher FRASOR bins the position appears to drift along the negative dec axis. This is unpredicted, and is probably related to the dependence of effective area on particle arrival and energy, coupled with the path of the Moon through the sky. For the shadow width in both the RA and dec directions, the shadow is narrower than the x=1.0 shadow until the higher FRASOR bins.

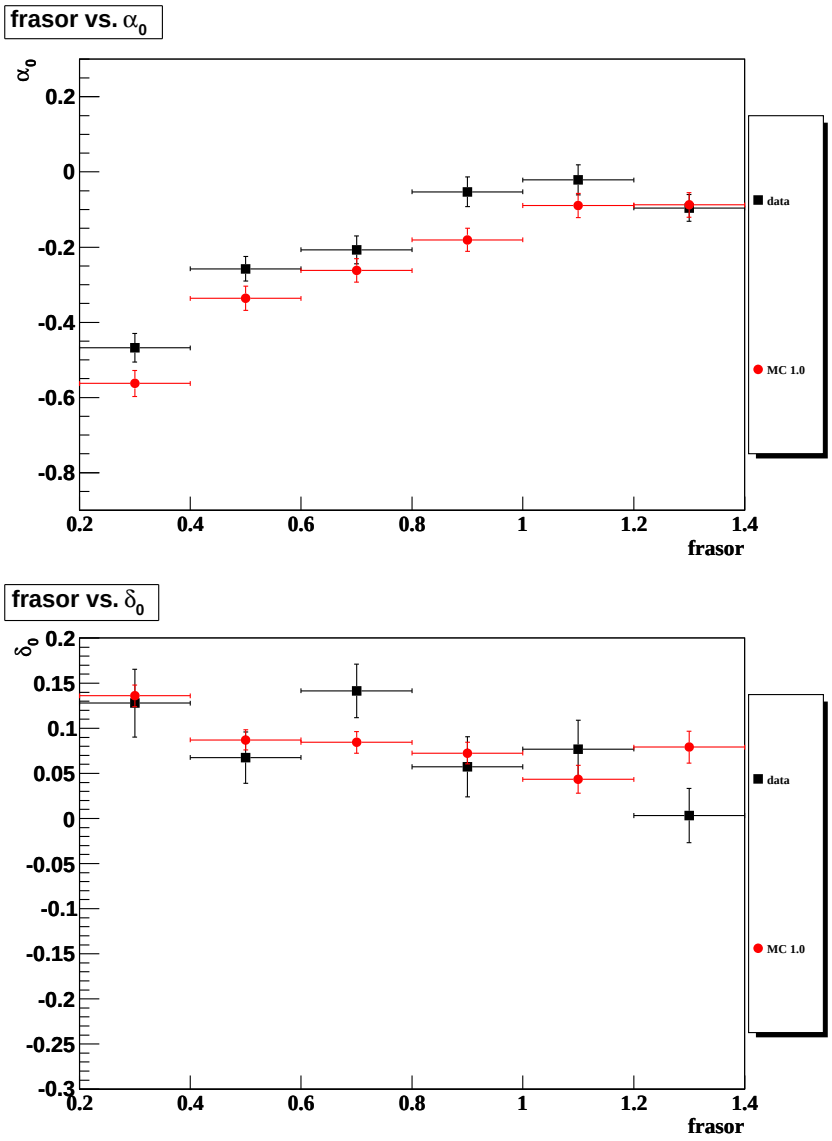

Figure 8.6: Comparison between data and MC in FRASOR bins for the Moon for position parameters from eq. 6.1.

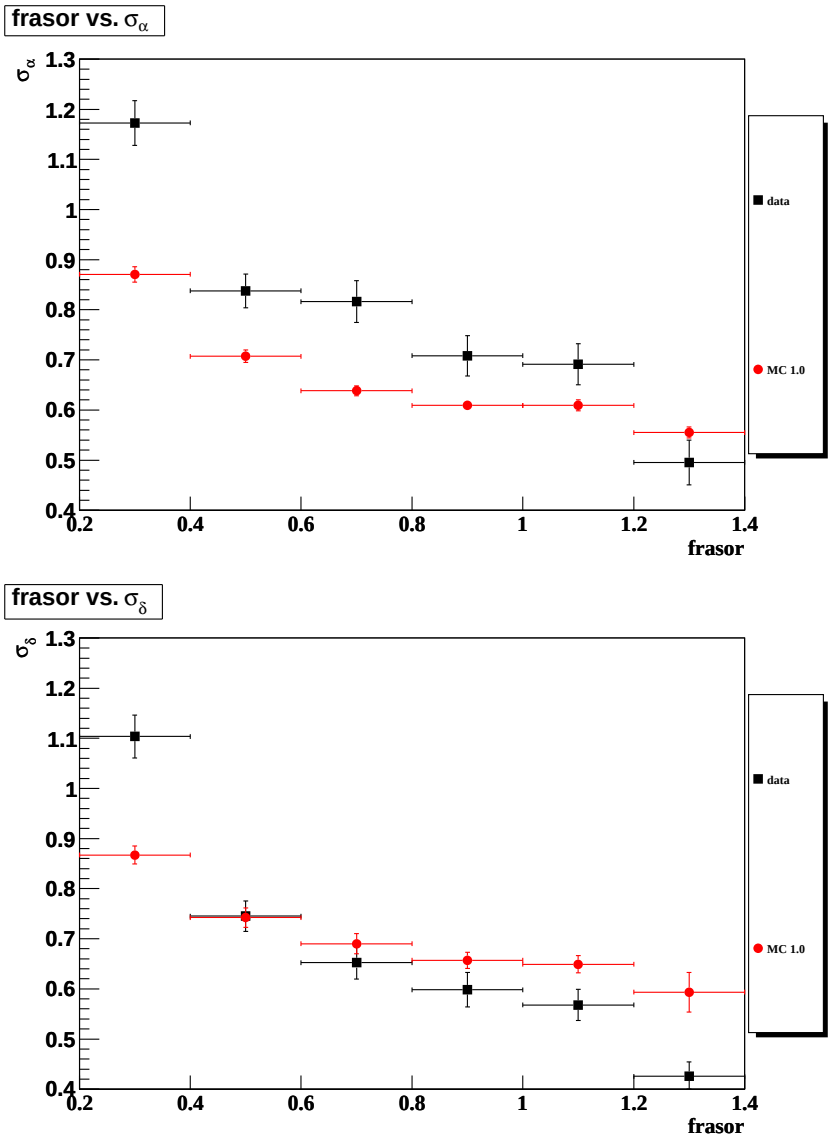

Figure 8.7: Comparison between data and MC in FRASOR bins for the Moon for width from eq. 6.1.

For x=2.0, low energy particles with large magnetic deflections are scaled to a higher energy, increasing their effective area. The shadow position is shifted farther than x=1.0 along the RA axis, as expected, for all FRASOR bins.

For nearly all bins, the x=1.0 parameters lie between the x=0.5 and x=2.0 parameters. Whilst x=1.0 is the best fit by eye in both α_0 and σ_α it is overall a bad match to the data. The energy scale x=0.5 is a better match for α_0 in some FRASOR bins, and the x=2.0 is a good match for some bins in σ_α. However, x=2.0 is a very poor match in α_0 to data as x=0.5 is a bad match in σ_α, providing strong evidence that the Milagro energy scale $0.5<x<2.0$. But this also means that it is unlikely a single energy scale will model all the parameters well.

Smaller shifts in energy scale are shown in figures 8.10 and 8.11 (x=0.8 and x=1.3) and figures 8.12 and 8.13 (a 10% shift of x=0.9 and x=1.1). As expected, the spread is smaller for smaller energy scale changes. In all cases, the Moon MC is again a poor match to α_0 and σ_α. It seems apparent at this point that no single energy scale in the Moon MC will model all the parameters well.

8.4 Comparison of Data and Monte Carlo Projections

Up to this point, comparisons between the data and Monte Carlo shadows of the Moon have relied on the 2-D gaussian fits to both. Rather than compare a model of a model to another model of data a clear direct comparison is available in the form of projections along the α and δ axes. For energy scales $0.5<x<2.0$ projections of

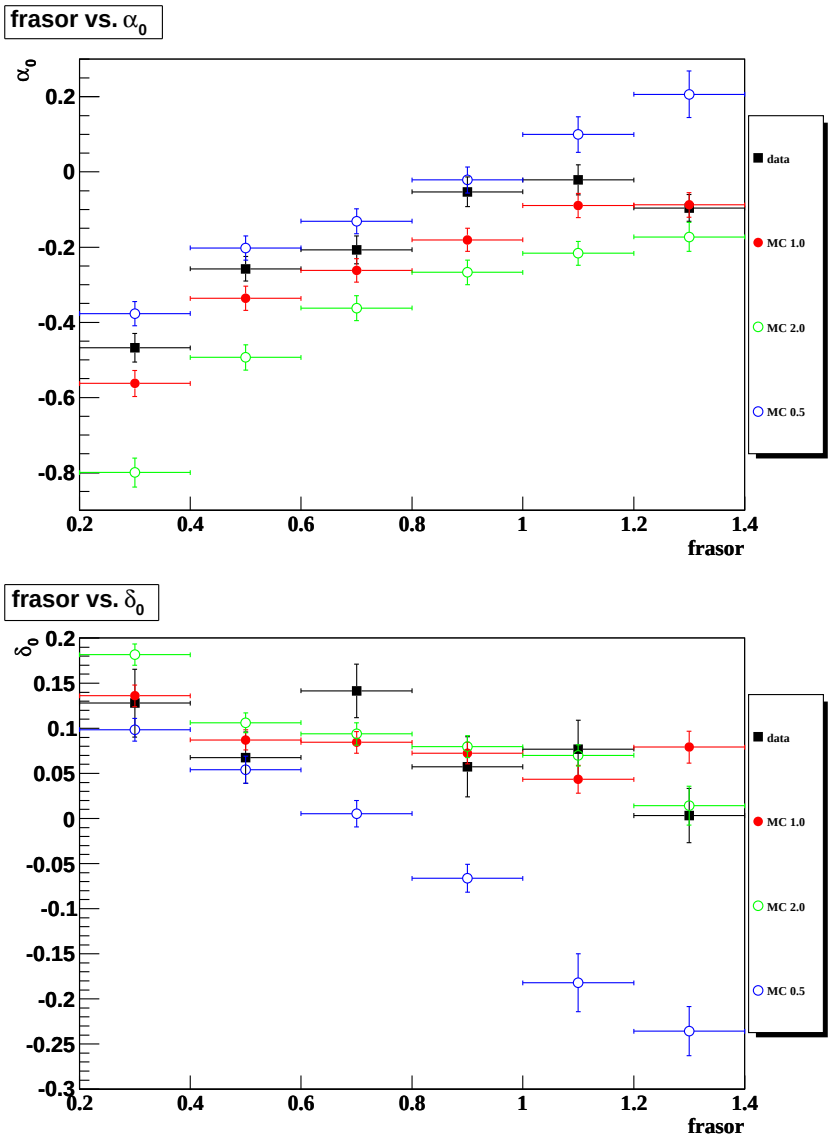

Figure 8.8: Comparison between data and MC for the Moon for position parameters from eq. 6.1, with data, x=1.0, x=2.0 and x=0.5.

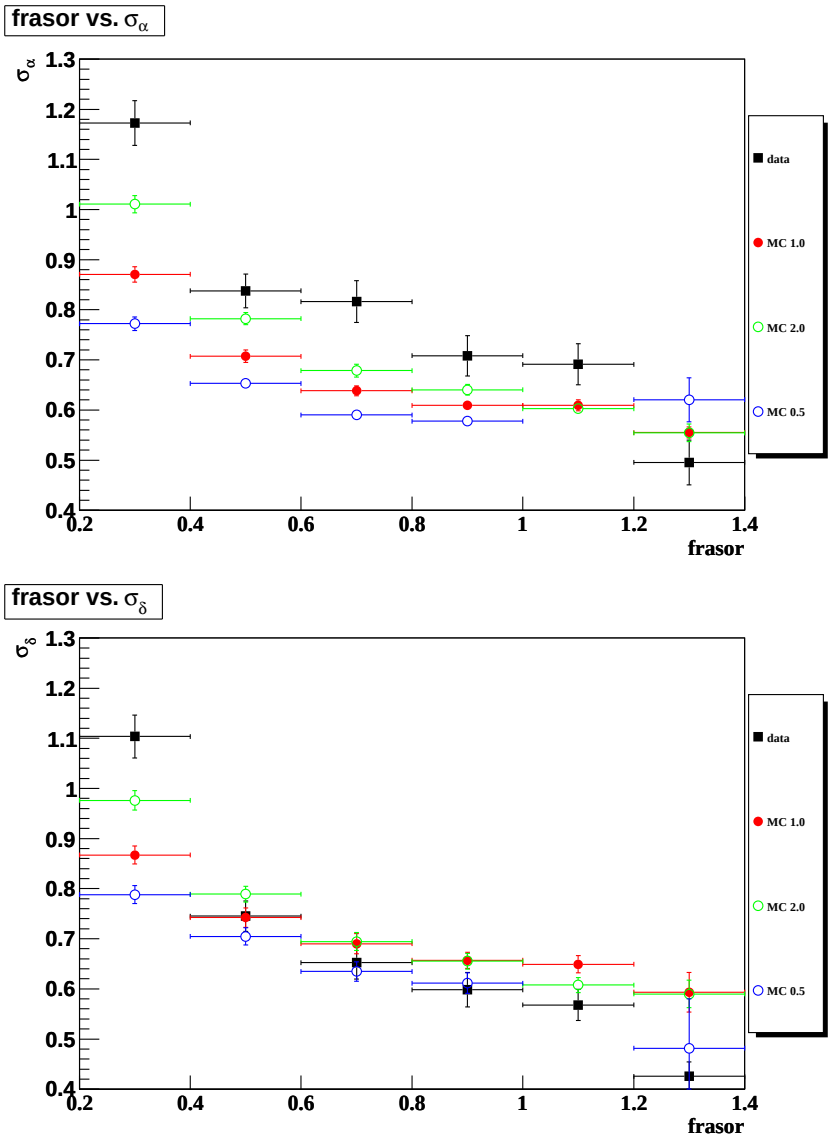

Figure 8.9: Comparison between data and MC for the Moon for width from eq. 6.1, with data, x=1.0, x=2.0 and x=0.5.

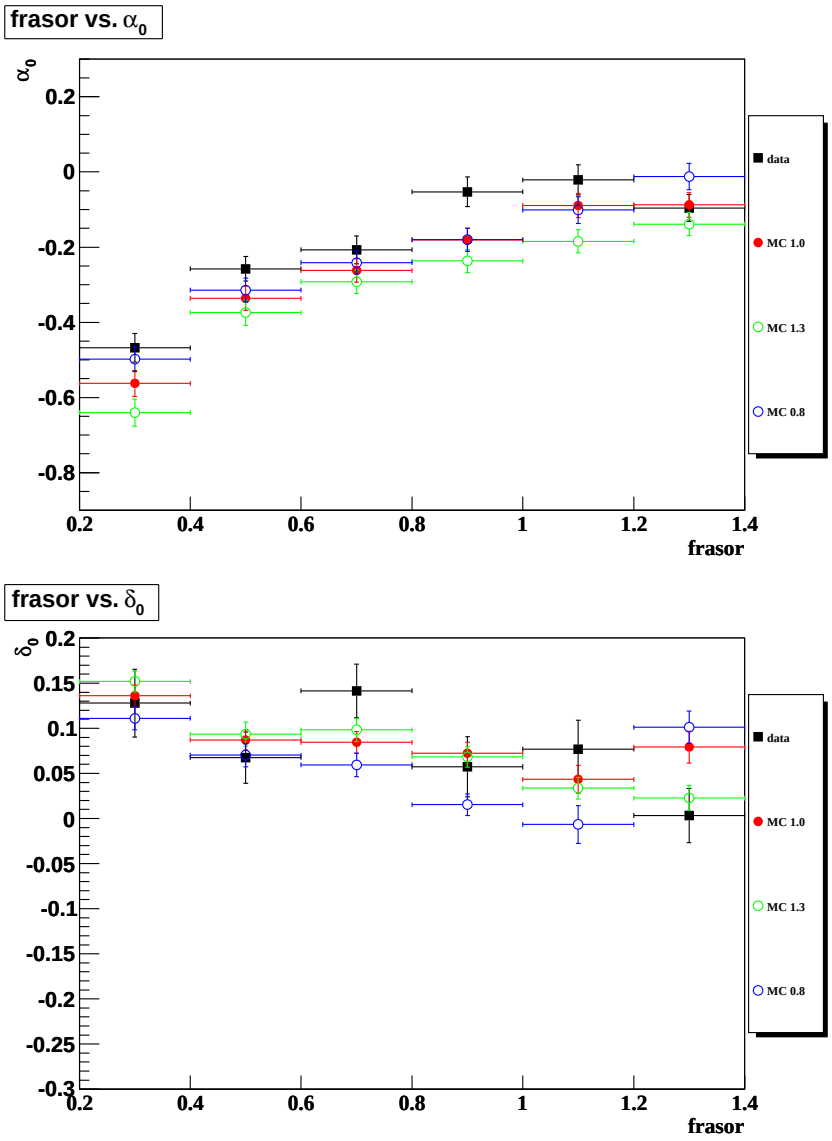

Figure 8.10: Comparison between data and MC for the Moon for position parameters from eq. 6.1, with data, x=1.0, x=1.3 and x=0.8.

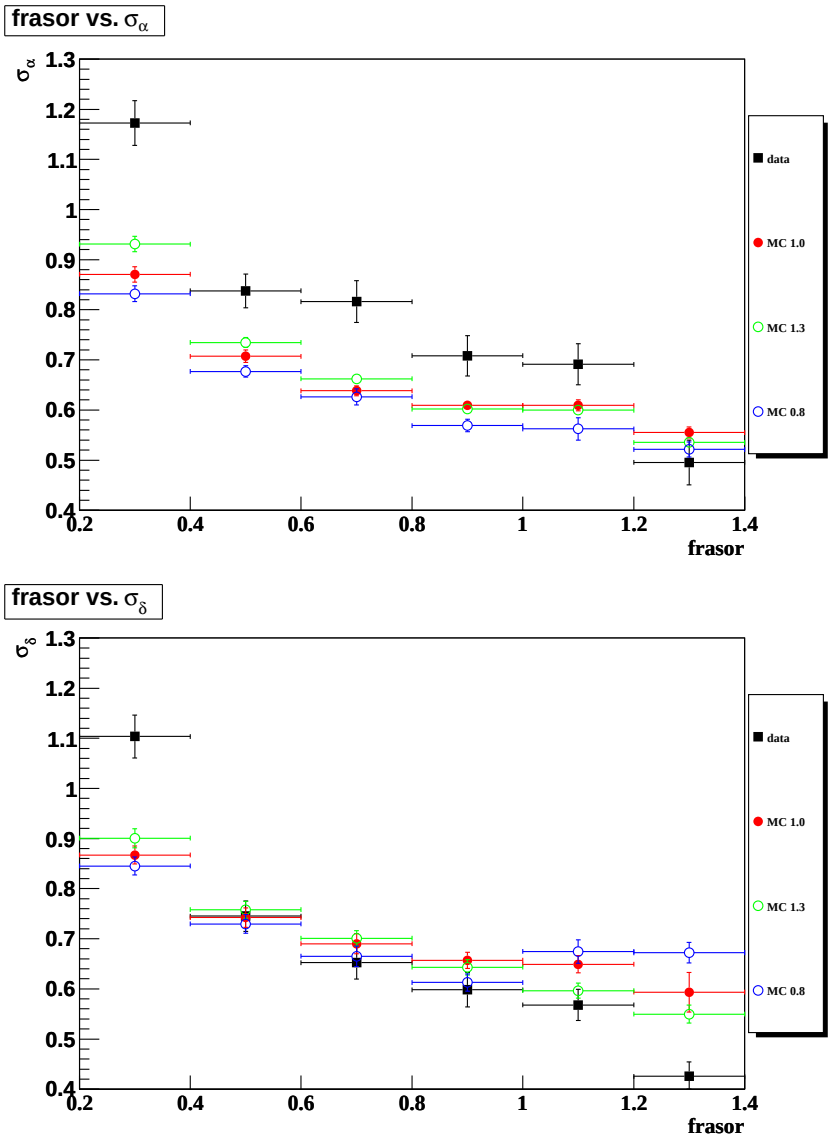

Figure 8.11: Comparison between data and MC for the Moon for width from eq. 6.1, with data, x=1.0, x=1.3 and x=0.8.

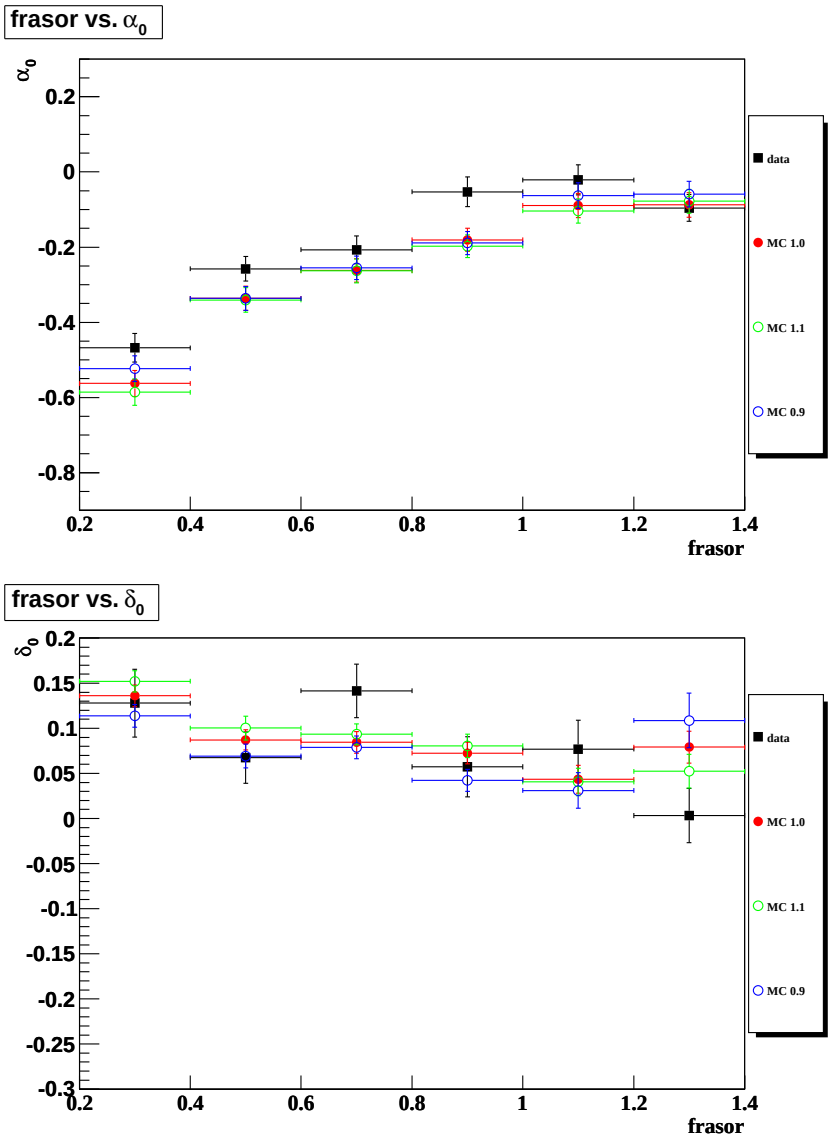

Figure 8.12: Comparison between data and MC for the Moon for position parameters from eq. 6.1, with data, x=1.0, x=1.1 and x=0.9.

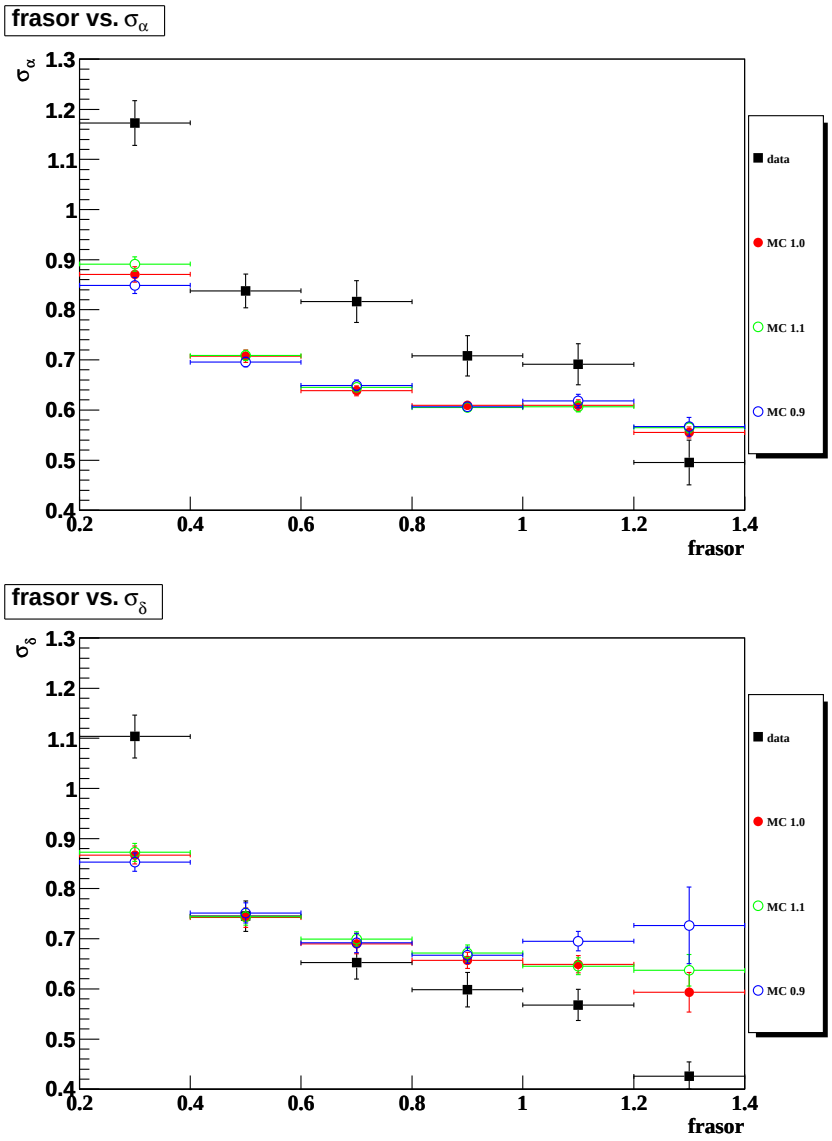

Figure 8.13: Comparison between data and MC for the Moon for width from eq. 6.1, with data, x=1.0, x=1.1 and x=0.9.

excess-maps of $\pm 1^{\circ}$ around the nominal Moon position are shown in figures 8.14 and 8.15.

For all energy scales the dec projections appear to be a good fit, as we saw using the 2-D gauss model. Looking at all energy scales in RA, the shadow is too narrow in the region opposite to the deflection direction. However, in the deflection direction, along negative RA, we see the width of the shadow increase as the energy scale increases. For low energy scales the shadow appears to be too narrow and for energy scales above x=1.0 the tail appears to model the data well. However, for x>1 the position of the peak drifts along the negative RA axis, and becomes a poor fit to the data. Despite not being able to model the shadow perfectly, the Moon MC shadow shows a clear sensitivity to the energy scale.

8.5 Why is no Single Energy Scale able to Model the Moon Shadow?

The Moon MC attempts to model an incredibly complex process. As discussed in section 8.2 the effective area and PSF are being modeled well. The other input into the Moon MC is the magnetic field, but there is also an additional complication from the EAS.

8.5.1 Uncertainty from the Magnetic Field Model

We already know that the Earth's magnetic field is not dipolar, especially close to the Earth's surface, where the majority of magnetic deflection occurs. Local

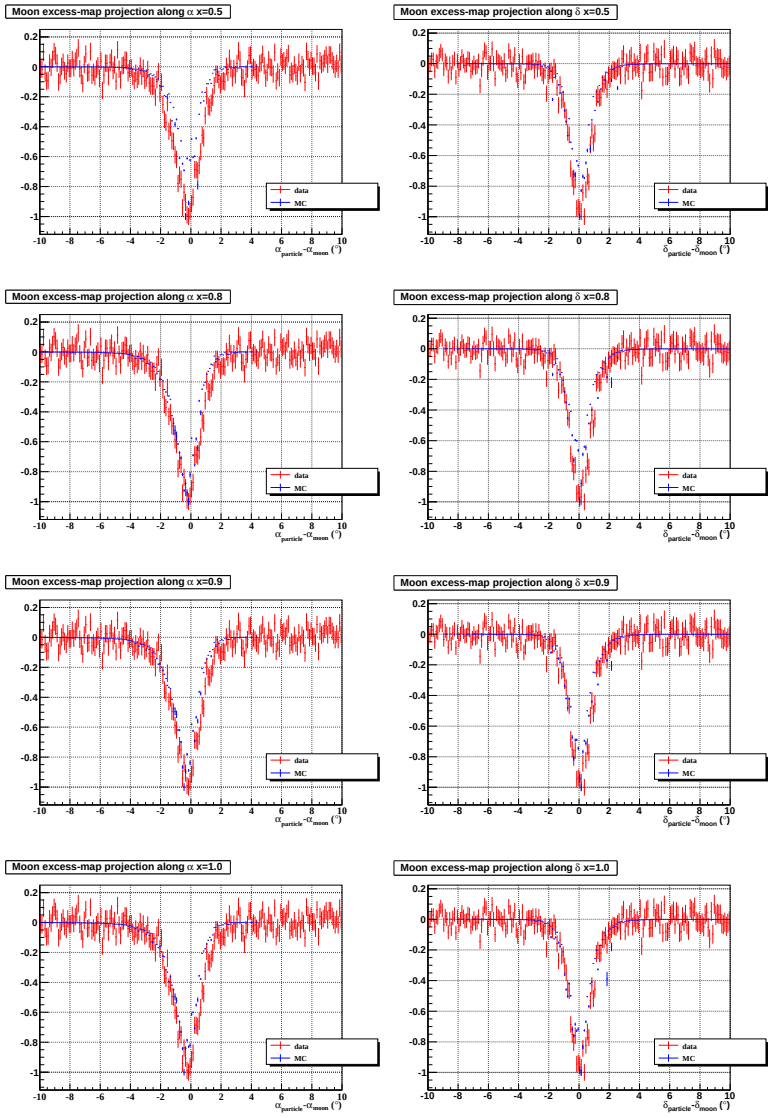

Figure 8.14: Comparison between data and MC for the Moon from projections of 2° slices centered on the nominal Moon position for RA and dec. Top: x=0.5, second: x=0.8 third: x=0.9, bottom: x=1.0. The amplitudes of the data and MC have both been normalized to 1 using the minimum excess bin from their respective excess-maps, as the Monte Carlo is designed to simulated the shadow shape and position, not the Milagro event rate.

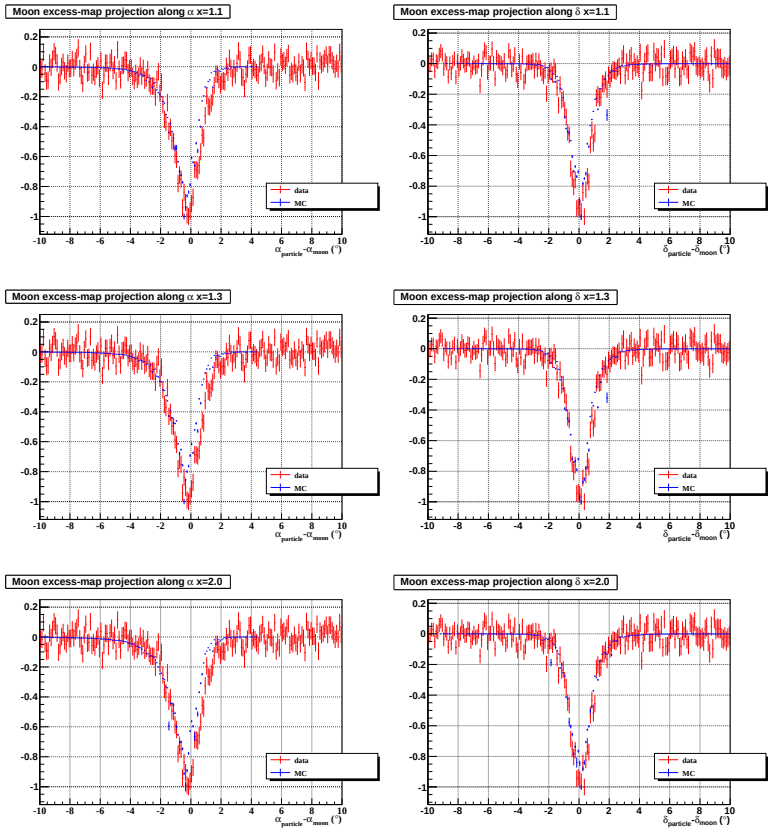

Figure 8.15: Comparison between data and MC for the Moon from projections of 2° slices centered on the nominal Moon position for RA and dec. Top: x=1.1, middle: x=1.3, bottom: x=2.0. The amplitudes of the data and MC have both been normalized to 1 using the minimum excess bin from their respective excess-maps, as the Monte Carlo is designed to simulated the shadow shape and position, not the Milagro event rate.

variations in the field could alter the deflections of the particles, either more or less, and could account for problems in modeling the Moon shadow. At Milagro the magnitude of the magnetic field from the simple dipole model is B_0=48.9 μT and from the IGRF B_0=49.4 μT which is approximately a 1% difference. The differences between the simple dipole and the IGRF field from Milagro to the Moon are complex. The total deflection of a 1 TeV proton is approximately 1.3° for the simple dipole. The differences between the IGRF and the simple dipole model for the path of the Moon across the sky are much larger than the 1% difference in magnitudes at Milagro, and requires a full study. Indeed, a simulation of the Moon shadow designed for the ARGO-B experiment, observed discrepancies on the order of 15% for deflections of sub-TeV particles between a dipole model and the Tsyganenko-IGRF model [101]. This certainly could account for differences between the Moon MC shadow and the data shadow.

8.5.2 Uncertainty from the EAS

We tracked the particles in section 7.2 from Milagro back towards the Moon. But the primary particle reacts in the upper atmosphere approximately 15 km above the surface of the Earth. After the first collision the EAS forms and is composed of both positive and negative particles in nearly equal numbers (as well as neutral particles). To a first approximation the effect of the magnetic field on this swarm of positive and negative particles would be to spread it out –not to deflect it.

This means we are over-estimating the deflection of particles in the Moon MC as we are propagating them through approximately 15 km of atmosphere through

which the shower overall would no longer be deflected. Qualitatively this could account for the increased deflection along the RA axis of the Moon MC. It is unclear what effect this would have on the width of the shadow in RA—the σ_α parameter—as this parameter is a convolution of effective area, the PSF and the magnetic field model.

The gyroradius r_g of a particle in a uniform magnetic field is given by

$$r_g = \frac{\gamma m v}{qB} \tag{8.2}$$

so for a 1 TeV proton passing through 15 km of a uniform field of magnitude B=50 μT the angular deflection is 0.01°, which is unable to account for the differences between the data and the Moon MC.

8.6 Status of the Energy Scale Calibration

The success of the Moon MC is clear. The agreement of width and position along dec is excellent and the agreement along RA is within 0.1° for both width and position along RA. We note that the δ_0 and σ_δ parameters, which are much less dependent on the magnetic field, match the data at an energy scale of 1.0 to within errors of less than two hundredths of a degree, and are inconsistent (at the 3-σ level) with a scale of x=0.5 or less. Looking at the projections appears to bear this out, and shows a clear sensitivity to energy scale. With the additions described above an energy calibration of Milagro is still possible and the work is ongoing.

In the next chapter, we now use the Moon MC as a tool when placing an upper limit on the antiproton/proton ratio.

Chapter 9

An Antiproton/Proton Ratio Upper Limit using the Moon Shadow

In this chapter, we find a 95% upper limit on the antiproton/proton ratio from Milagro data. The antiproton/particle ratio limit is Monte Carlo independent and we only invoke the Moon Monte Carlo to estimate the particle/proton ratio of the Moon shadow to arrive at a $\bar{p}/p$ ratio.

In Milagro data, the Moon particle shadow is a sink deflected to the west, along the negative right-ascension axis, in particle minus Moon coordinates. A second shadow, caused by the presence of antiprotons, would be deflected to the east along the positive RA axis.

The particle shadow is well modeled by a 2-D gaussian –which can be used in an antiproton shadow search, if we assume that the antiproton shadow also takes

this shape. We first search the data for an antiproton shadow at the reflected position and at the same width of the particle shadow. No antiproton shadow is found.

Since no antiproton shadow has been found, a 95% upper limit to the antiproton shadow amplitude is set using the measurement and uncertainties of the amplitude in the fit.

We test the sensitivity of the data search using 1000 simulated maps to search for an antiproton shadow. The limit of the measured result is interpreted in terms of the simulated sensitivity.

To reduce the model dependence of the search we then search over the entire 4 dimensional parameter space of the probable position of the antiproton shadow. The final result is presented as the 95% upper limit over a grid in antiproton shadow center location.

9.1 Fit to the Data with Particle and Antiproton Shadows

In section 6.4, a 2-D gaussian was shown to be a good fit to the particle shadow. Now, using the unsmoothed excess-map, (fig. 6.12) the data is searched for the antiproton shadow, using two gaussians. The first models the particle shadow and the second models the antiproton shadow. The two gaussians used are better described as a twin 2-D gaussian—a six parameter 2-D gaussian—where the positions of the two gaussians are mirrored in the RA and dec axes with identical widths.

It is of the form:

$$g(\alpha,\delta;A,\bar{A},\alpha_0,\delta_0,\sigma_\alpha,\sigma_\delta) = \frac{A}{2\pi\left(\sigma_\alpha^2+\sigma_\delta^2\right)}\exp\left[-\frac{1}{2}\left(\frac{\left(\alpha-\alpha_0\right)^2}{\sigma_\alpha^2}+\frac{\left(\delta-\delta_0\right)^2}{\sigma_\delta^2}\right)\right] + \frac{\bar{A}}{2\pi\left(\sigma_\alpha^2+\sigma_\delta^2\right)}\exp\left[-\frac{1}{2}\left(\frac{\left(\alpha+\alpha_0\right)^2}{\sigma_\alpha^2}+\frac{\left(\delta+\delta_0\right)^2}{\sigma_\delta^2}\right)\right] \tag{9.1}$$

where $\bar{A}$ is the antiproton shadow amplitude. The parameters A, α_0, δ_0, σ_α and σ_δ are all fixed from the fit results of the particle shadow using eq. 6.1 and only the antiproton shadow amplitude may vary.

As stated above the position and width of the antiparticle shadow in the search are fixed. If the antiproton shadow width is free to vary, it assumes the largest width possible and the shadow becomes wide and flat. If, alternatively, the position of the antiproton shadow is free it moves to the boundary, typically at the particle shadow side.

The fit is done in root, using the TMinuit package [102], with χ^2 minimization. The convergence on the χ^2 minimum is parabolic, as shown in fig. 9.1. No antiproton shadow is found. The parameters for the fit are displayed in table 9.1. One may be tempted to cut the Milagro data, in FRASOR or N_{fit}, to produce excess-maps where the Moon shadow is farther from the origin in order to improve the fit. However, these cuts decrease the shadow amplitude which in turn gives a lower $\bar{p}$/particle upper limit. One may also be tempted to split the data into FRASOR bins, and then do an optimized search between maps. However, the $\bar{p}/p$ ratio would not be constant between each map, as it is energy dependent.

parameter	fit	error
2-D gauss fit		
A	-2319	52
α_0	-0.27	0.02
δ_0	0.11	0.02
σ_α	0.92	0.02
σ_δ	0.78	0.02
2-D twin-gaussian fit		
$\bar{A}$	1.0	33

Table 9.1: Results of the 2-D gaussian fit using eq. 6.1 to the data excess-map followed by fitting eq. 9.1 with the 5 parameters from eq. 6.1 fixed.

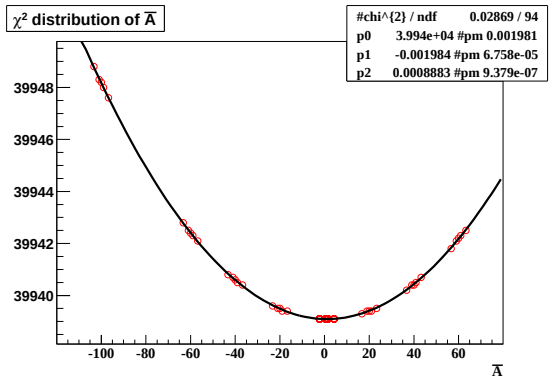

Figure 9.1: χ^2 parabolic convergence of $\bar{A}$. Each collection of points is from a different initial condition. After several iterations they all converge on the minimum. The parabola is not continued further along the positive axis as positive values are unphysical.

9.1.1 A 95% Upper Limit to the Antiproton Shadow Amplitude

Using this fit, we can set a 95% upper limit on the antiproton shadow amplitude and hence the particle/antiproton ratio. We have a measured value for the antiproton shadow amplitude $\bar{A}_{meas} = 1 \pm 33$. The true, unknown value of the amplitude is $\bar{A}_{true}$. The 95% upper limit on $\bar{A}_{true}$ is determined as $\bar{A}_{95}$, that value of $\bar{A}$ which would have a 5% probability of giving $\bar{A}_{meas}$. That is, $\bar{A}_{95}$ is the solution to

$$p(\bar{A} = \bar{A}_{\text{meas}} | \bar{A}_{95}) = 0.05 \tag{9.2}$$

Since the fit to $\bar{A}_{meas}$ is parabolic in χ^2, we can use the gaussian property of χ^2 to determine the 95% value by integrating the gaussian with $\sigma = 33$. We

find $\bar{A}_{95} = -54$ from a gaussian cumulative distribution function. Therefore, the antiproton/particle ratio 95% upper limit is $54/2300 = 2.3\%$.

9.2 Sensitivity Search with Simulated Maps

We can check the sensitivity of the data 95% upper limit on the antiproton shadow amplitude with simulations. We simulate 1000 excess-maps, each with a 2-D gaussian, to simulate the Moon shadow, added to noise. Each map is then fitted to a twin gaussian in the same manner as the data search.

The noise is found using Li-Ma statistics [23], as described in sec. 3.3, to find the uncertainty from the Milagro MDI generated background. The noise is generated bin by bin, so the total bin content h at RA-dec α_i, δ_j is:

$$h\left(\alpha_i, \delta_j\right) = f\left(\alpha_i, \delta_j\right) + N\ \sigma\left(\alpha_i, \delta_j\right) \tag{9.3}$$

where f is the 2-D gaussian from eq. 6.1, σ is the noise and N is a random number chosen from a gaussian distribution $\mu = 0,\ \sigma^2 = 1$. The fluctuations of the Moon particle shadow gaussian are negligible relative to the noise fluctuations so are ignored. The excess-map with and without noise is shown in fig. 9.2.

The 1000 simulated maps are searched, using the twin-gaussian of eq. 9.1 in the same manner as the data search. We then have 1000 values of $\bar{A}_{meas}$. Each value of $\bar{A}_{meas}$ has the same uncertainty –which is the same as that from the data search. Moreover, as the uncertainty is dominated by the background the $\bar{A}_{95}$ distribution can be assumed to have the same width.

The 1000 values of $\bar{A}_{meas}$ follow a gaussian distribution and we find $\langle \bar{A}_{meas} \rangle =$

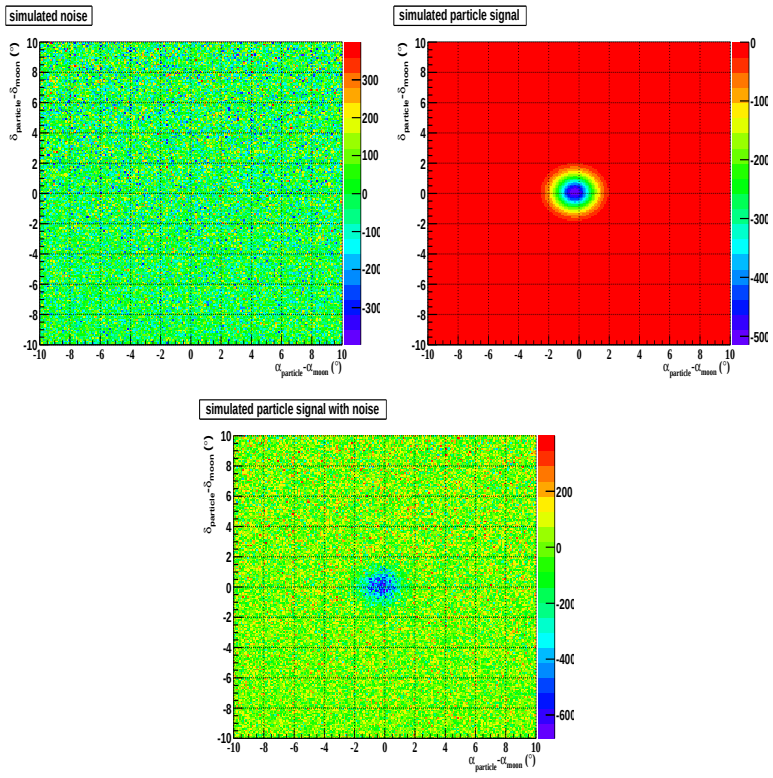

Figure 9.2: a map of noise as given by eq. 9.3, then maps using a 2-D gaussian with parameters from tab. 9.1, then added to make a simulated Moon-map.

$1.8 \pm 33/\sqrt{1000}$. As expected, the width of the distribution of $\bar{A}_{meas}$ is the same as the uncertainty in each individual $\bar{A}_{meas}$ from any map. Given $\langle \bar{A}_{meas} \rangle$, then $\langle \bar{A}_{95} \rangle = -53$, so the measured $\bar{A}$ upper limit is consistent with the expected sensitivity.

9.3 Reducing the Model-Dependence of the Search

So far, we have assumed that the antiproton shadow resides at the mirrored position of the particle shadow. Here we relax this condition.

9.3.1 What do we know of the true antiproton shadow?

There are two effects that lead us to expect that the antiproton shadow would not be where we are modeling it, or be of the width at which we are modeling it.

First, the particle shadow is composed primarily of protons and helium, with a small contribution from heavier elements. The heavier elements have a lower magnetic rigidity for a given energy than protons, so are deflected more by the geomagnetic field. They also have different spectra and different detector response (effective area and point spread function).

Second, an antiproton signal—barring the event of a dominant exotic signal—is the result of spallation of primary cosmic rays producing secondary $\bar{p}$ in the interstellar medium (ISM). Using the boron/carbon ratio as a tracer of the $\bar{p}/p$ ratio, we would expect a softer spectrum of $\bar{p}$ than p. Even if we assume an identical detector response for protons and antiprotons (of the same energy and arrival

direction) and could model the proton shadow perfectly, we could not presume the position and width of the antiproton shadow due to the differing spectra.

9.3.2 Search at the Moon MC Antiproton Shadow Location

We can also search using the Moon Monte Carlo to simulate the antiproton shadow position, modeling the antiproton with an identical spectral index to that of the proton. For the same cuts as the data the particle shadow is at α_0 = -0.36±0.03. With an identical spectrum, the antiproton shadow appears at α_0=0.40, δ_0=-0.07, σ_α=0.73 and σ_δ=0.74. At this position, searching the data we find $\bar{A}$=-0.5±23. Then $\bar{A}_{95}$ = -48, corresponding to a flux ratio $\bar{p}$/particle=2.1%.

9.3.3 Ranged Fit Search

In place of a single point, we now search for the antiproton shadow over the 4-dimensional parameter space of the 2-D gaussian that models the antiproton shadow, leaving the antiproton shadow amplitude free to vary.

Choosing the Range of Fit parameters

The particle shadow fit parameters are displayed in table 9.1 and in the previous section we used the MC to find the antiproton shadow.

A secondary $\bar{p}$ production model would soften the spectrum considerably. Naively, we would expect the antiproton shadow to be deflected further east, but the convolution of a softer spectrum with effective area leaves the outcome un-

clear. Even so, we expect deflection along the positive RA axis on the order of a degree is a reasonable upper limit. Deflection along dec is less than along RA so a reasonable limit for the search is -0.5° to 0.4°.

The width is limited by the Milagro PSF, the lowest width for any particle shadow was for high FRASOR bins, and just less than 0.5°, so here we set a lower limit of 0.4°. As the antiproton shadow is single species, it should not be wider than the particle shadow, so we set a conservative upper limit of 1°.

Ranged Fit Search Results

Varying $0^\circ < \alpha_0 < 1^\circ$, $-0.5^\circ < \delta_0 < 0.4^\circ$, $0.4^\circ < \sigma_\alpha < 1^\circ$ and $0.4^\circ < \sigma_\delta < 1^\circ$, we search over the whole parameter space fixing each of the parameters in 0.1° intervals, leading to a total of 3240 searches, or 36 for each position in α, δ.

The resulting antiproton shadow amplitude of each of the fits can be converted to $\bar{A}_{95}$, the 95% upper limit on the amplitude of the antiproton shadow, as described in sec. 9.1.1. The fit results for α_0=0.1° and δ_0=-0.5° are shown in fig. 9.3

The fit results for a slice in σ_α=0.6° and σ_δ=0.6° are shown in fig. 9.4. These plots show typical slices. The variation in $\bar{A}_{95}$ is small, mostly between $-65 < \bar{A}_{95} < -40$. We show the final results using the worst (deepest) amplitude, when varying σ_α and σ_δ, for each α, δ slice. So for each position we find the largest magnitude amplitude and display those results with each shadow position in fig. 9.5.

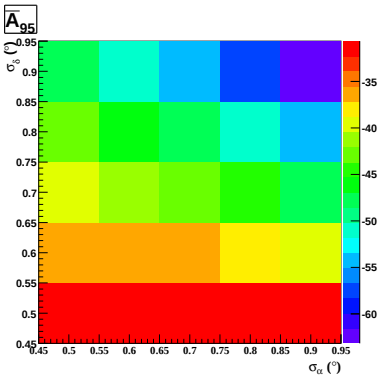

Figure 9.3: $\bar{A}_{95}$ values for a slice through α and δ parameter space with fixed α_0=0.1° and δ_0=-0.5°.

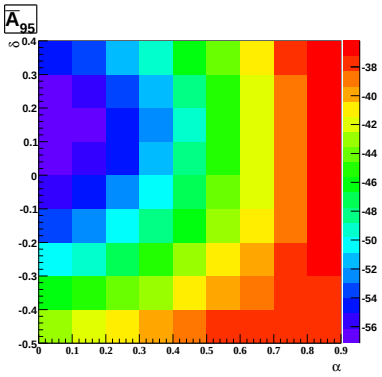

Figure 9.4: $\bar{A}_{95}$ values for a slice through σ_δ and σ_α parameter space with fixed σ_α=0.6° and σ_δ=0.6°.

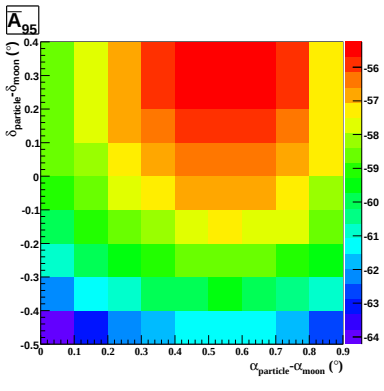

Figure 9.5: A map of $\bar{A}_{95}$ with each the value at each position taken as the deepest shadow for that α, δ slice, which will correspond to the least stringent limit on the antiproton/proton ratio.

Coarseness of the Grid

As a final check, we examine the effect of the coarseness of the grid on the results. The α and δ coarseness is the same as that of the data; finer binning is possible but not necessary. We again build simulated maps, as in section 9.2. Now, in addition to the particle shadow, we add an antiproton shadow of amplitude $\bar{A} = -54$. The other parameters of this simulated antiproton shadow are taken from table 9.1, with α_0 and δ_0 taken as negative as the shadow is modeled as mirrored in the RA and dec axes of the particle shadow.

We fit 1000 simulated maps using eq. 9.1, where the input parameters, other than the antiproton shadow amplitude, are fixed. This fit returns an average fitted amplitude of $\bar{A}= 54 \pm 33/\sqrt{1000}$, which is consistent with the antiproton shadow amplitude that we added to the simulated maps.

To check the coarseness of the binning, we then search the same simulated maps with a shadow smaller in both σ_α and σ_δ by 0.05° –half the grid spacing. This fit gives $\bar{A}$= 53 $\pm 31/\sqrt{1000}$, which is within 1-σ of the input amplitude, which is consistent with our choice of binning in σ_α and σ_δ.

Finally we search the same simulated maps with α_0 and δ_0 offset by 0.05° and we find $\bar{A}$= 54.5 $\pm 33/\sqrt{1000}$, which is within 1-σ of the input amplitude. This is again consistent with our binning choice.

Antiproton/Proton ratio

Up to this point we have remained Monte Carlo independent, but to convert the antiproton/particle ratio into a more informative antiproton/proton ratio we use the Moon Monte Carlo. Rather than compare trigger rates of the detector of protons vs all particles we should compare trigger rates close to the Moon position, so the acceptance rate follows the path of the Moon.

In fact, the best measure of the particle/proton ratio comes from the number of shadowed particles. For the same period as data, tracking the particles and weighting with effective area as described in chapter 7 we find the total number of shadowed particles is 6.26×10^7 and 4.44×10^7 for protons, giving a particle/proton ratio of 1.41. We display the final results as the $\bar{p}/p$ ratio 95% upper limit % by position of the antiproton shadow in fig. 9.6.

Using the Monte Carlo to model the antiproton with an identical spectral index to the proton we found in sec. 9.3.2 that $\bar{p}$/particle=2.1%, which corresponds $\bar{p}/p$=3%.

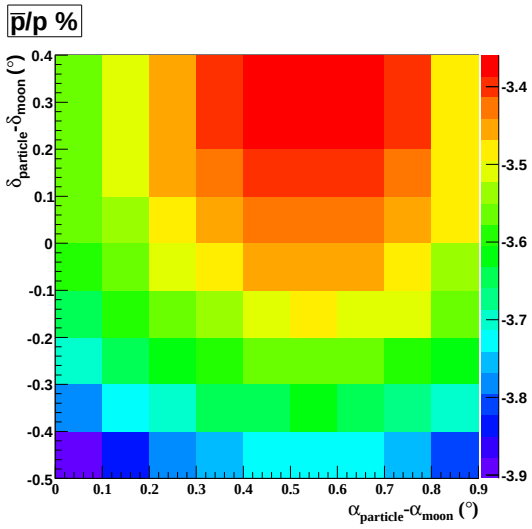

Figure 9.6: 95% $\bar{p}/p$ upper limits in % by fitted antiproton central position.

Median Energy of the Antiproton/Proton ratio

We do not know the energy spectrum of the antiprotons, but we do know the median energy of the protons. As when determining the particle/proton ratio, we use the Moon MC to find the median energy of protons that are shadowed by the Moon which is 1.7 TeV.

Chapter 10

Correlation of the Sun Shadow Depth with the Solar Magnetic Cycle

At the beginning of Milagro operation in 2000, the Sun was at a maximum in its solar cycle and at the end of Milagro operation in 2008 was at minimum, as described in chapter 5. As the Sun becomes more active, events such as coronal mass ejections and sunspots become more frequent. This should mean that particles of a given energy will be less likely to be shadowed as the activity of the Sun increases. To evaluate this time dependence of the Sun shadow we use all available Milagro data from 2000-2008. There are large variations between Milagro epochs, which makes epoch to epoch comparisons difficult. However, we can use the Moon shadow as a check of Milagro systematics to observe the true behavior of the Sun's shadow as the Sun progresses through its magnetic cycle.

10.1 The Yearly Sun Shadow

To look at the solar data over time, we make yearly plots of the Sun shadow and compare these to yearly plots of the Moon shadow in figures 10.1, 10.2 and 10.3. The Moon shadow is always deeper (more significant) than that of the Sun, but the Sun shadow gets deeper over time. The Moon shadow stays more or less at the same depth, with only slight variability, other than for 2000 and 2008, which are only partial years.

To examine this relationship further, we look at the integrated fractional deficit plots over the same periods, in figures 10.4 and 10.5. From early to late years, the Moon plateaus at one, so the Moon is shadowing a number of particles corresponding to its geometric area. The fraction at which the Sun plateaus rises over time. The Sun is shadowing nearly no particles in 2000, but is shadowing a number nearly equal to its geometric area in 2008. This is a result of decreasing solar activity as the Sun moves from maximum to minimum phase.

10.1.1 The Moon Geometrical Area from Year to Year

It should be noted that the geometrical area of the Moon calculated from the Monte Carlo in section 7.7.2 is based on the Moon in all of Epochs 7-9. Therefore only 2008, 2007 and 2006 are correctly normalized. The 2005 Moon has some epoch 6 events, so before and including that year the integrated fractional deficit plots of the Moon are incorrectly normalized. To gain correctly normalized factors the Moon Monte Carlo would have to be extended to simulate the Moon shadow pre-epoch 7, which is not performed in this thesis. However, the 2000-2005 Moon

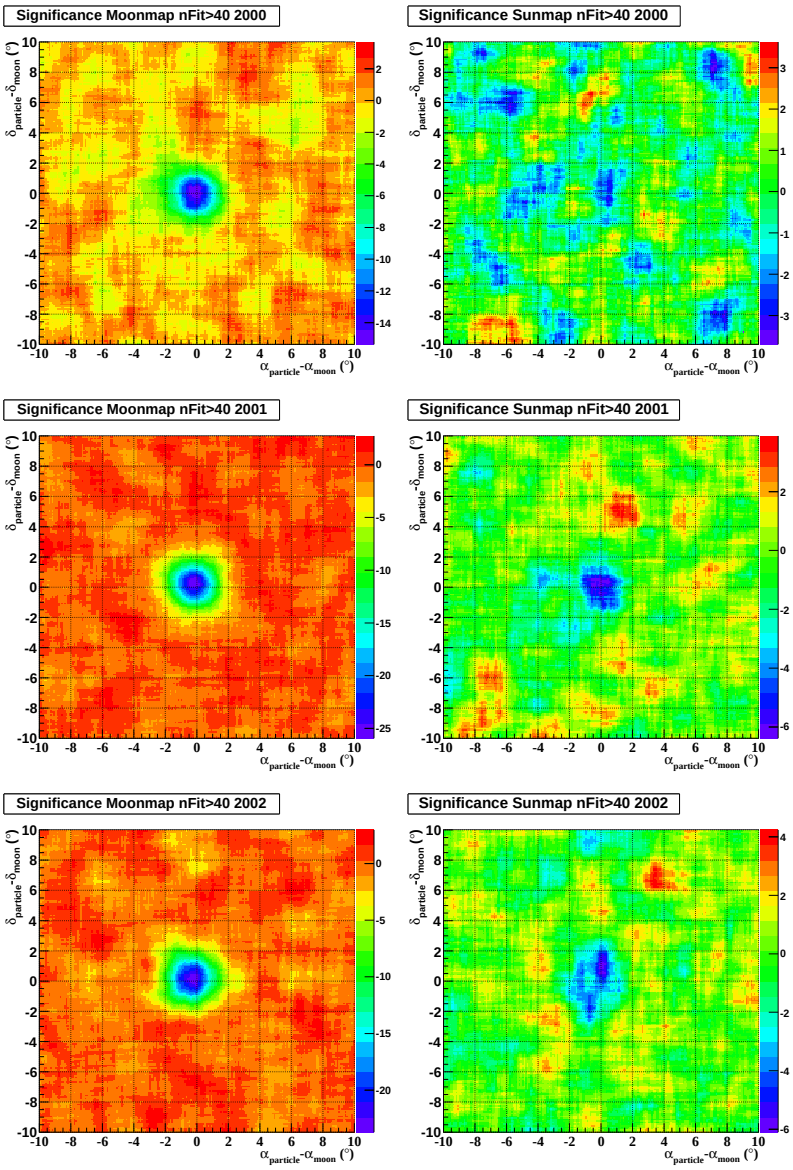

Figure 10.1: The Moon and Sun shadows from 2000-2002. Year 2000 data is not a complete year. Cuts on N_{fit}>40, zenith angle<60°.

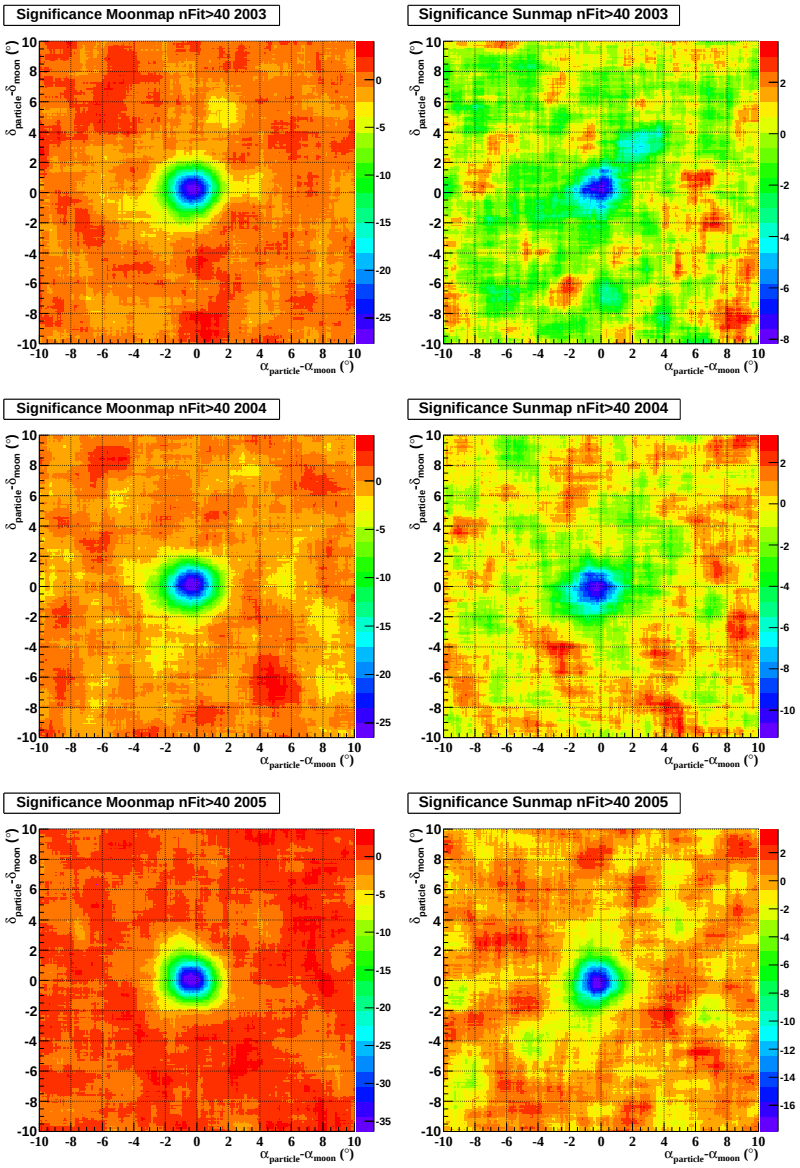

Figure 10.2: The Moon and Sun shadows from 2003-2005. Cuts are N_{fit}>40, zenith angle<60°.

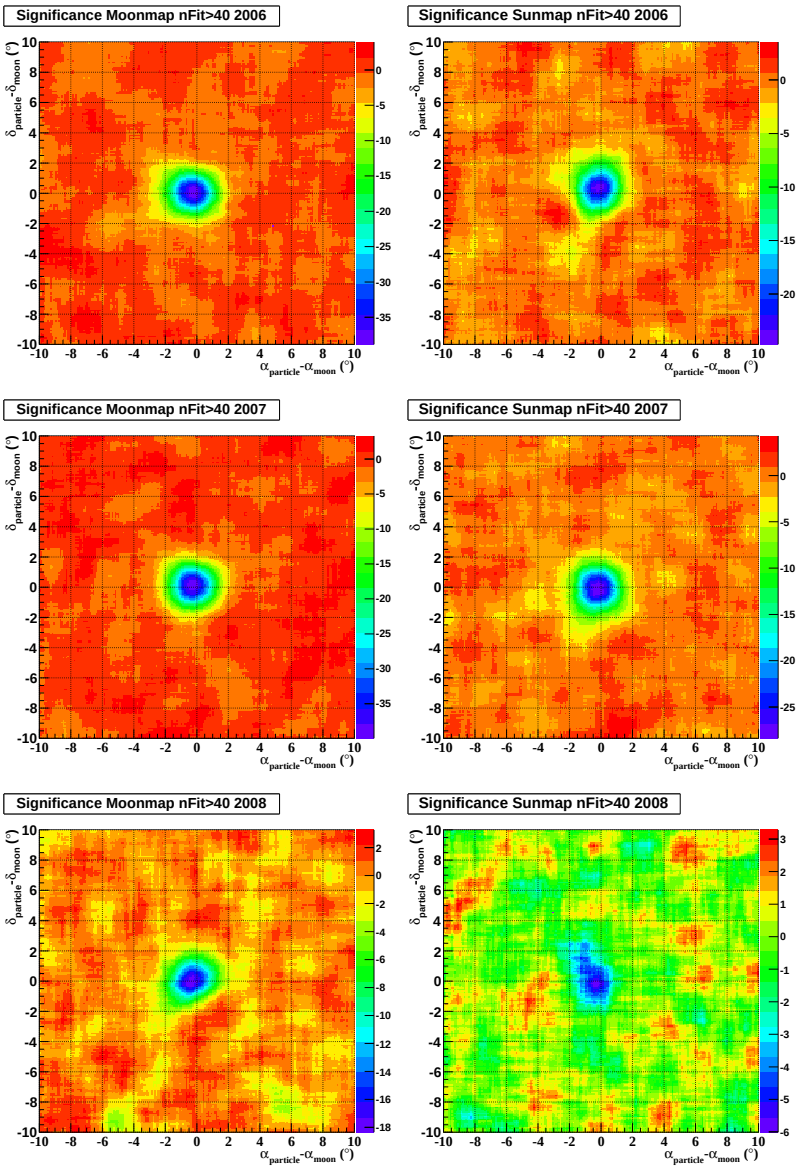

Figure 10.3: The Moon and Sun shadow from 2006-2008. Year 2008 data is not a complete year. Cuts are N_{fit}>40, zenith angle<60°.

remains an effective check of the systematics from epoch to epoch for the Sun's shadow.

10.2 Correlation of the Sun Shadow Depth with Sunspot Numbers with the Moon Shadow as a Systematic Check

To directly compare the time variation of the shadow with the solar magnetic cycle we plot the Moon and Sun integrated deficit at 4° with the relative sunspot number in figure 10.7. We chose to plot the integrated deficit at 4° so the shadow has begun to plateau, but the uncertainties are not too high.

There is a clear anti-correlation with the solar shadow at the integrated fractional deficit at 4° and the sunspot number. Milagro is clearly sensitive to the solar cycle, so the challenge is to then interpret these results in terms of the HMF.

10.3 A Simple Model of the Coronal Magnetic Field

We use the shadow Monte Carlo to model the coronal magnetic field with the simplest possible model at solar minimum, a dipole with strength 1.7×10^{22} Tm^3, and the magnetic poles aligned parallel to the Earth's. This toy model can be extremely informative. Whilst it does not include the Parker spiral or the Fisk field, we would expect the influence of these fields to average out over large periods

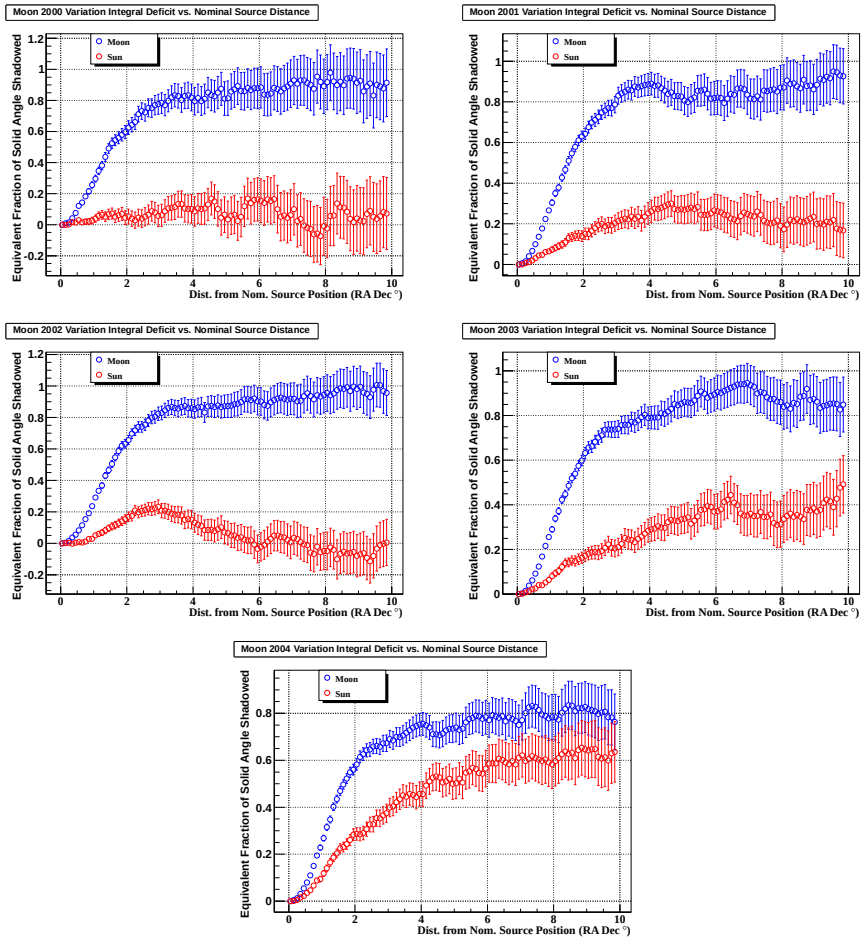

Figure 10.4: The Moon and Sun shadow integrated fractional deficits from 2000-2004. Year 2000 data is not a complete year. Cuts are N_{fit}>40, zenith angle<60°.

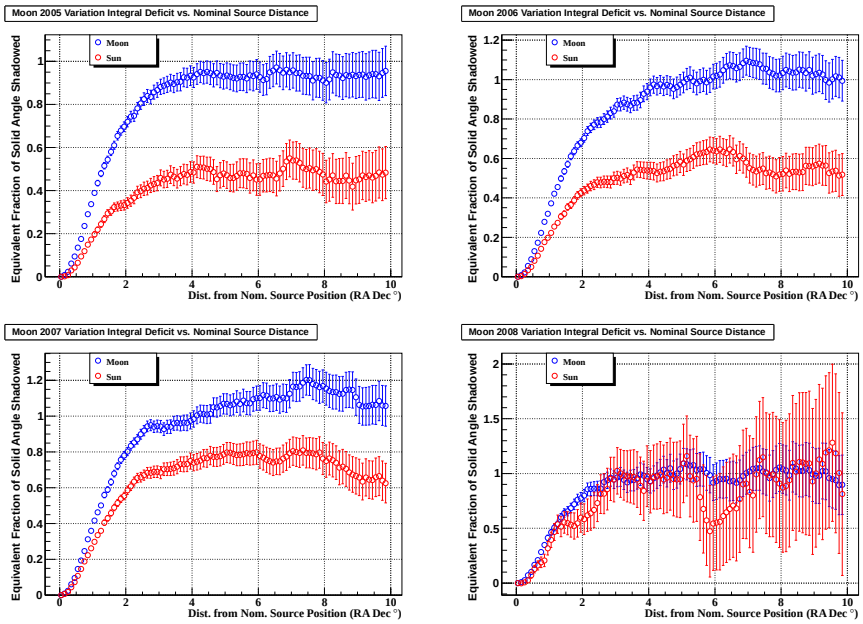

Figure 10.5: The Moon and Sun shadow integrated fractional deficit from 2005-2008. Year 2008 data is not a complete year. Cuts are N_{fit}>40, zenith angle<60°.

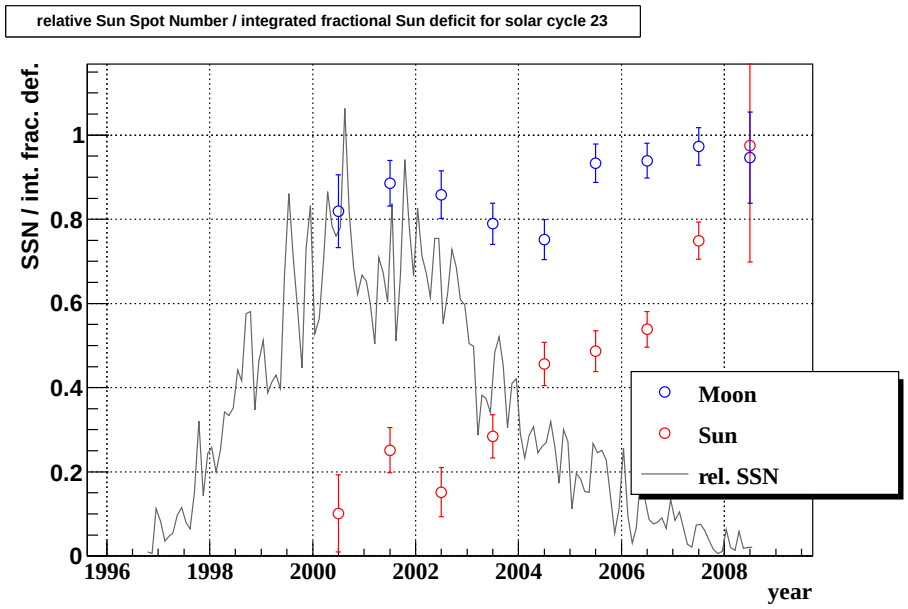

Figure 10.6: Relative sunspot number (sunspot number normalized to one) for solar cycle 23. The NOAA sunspot number is compiled by the US National Oceanic and Atmospheric Administration. The numbers are the monthly averages (SSN). This is displayed with the integrated fractional deficit of the Moon and Sun's shadow at 4° yearly, from 2000-2008. The Moon from 2000-2005 is not correctly normalized, as described in section 10.1.1.

of time as the Earth passes below and above the current sheet and will spend nearly equal times in both sectors. The choice of orientation of the dipole in this model means that the position and width of the Sun shadow should not be taken too seriously. However, the integrated and fractional deficit plots are symmetric views of the character of the Sun shadow so allow comparisons between the model and the data. The principal benefit of this toy model is not the shape of the shadow, is the total fraction of particles the Sun shadows.

As can be recalled from previous sections, the Moon has no magnetic field, so we expect the number of shadowed particles to be equal to that blocked out by the geometrical area of the Moon in the chosen coordinate system. The Sun, in contrast has its own magnetic field so will deflect particles away from its surface by virtue of the coronal field. As phase space volume is conserved, for each particle deflected away from the Sun and away from the path of Milagro, another will be deflected into the path of Milagro. Hence, these particles will not contribute to a solar shadow as a consequence of its coronal field, and the Sun shadow observed is less deep than would be expected based on the geometric area of the Sun. Moreover, the fraction shadowed is a consequence of the magnetic field model used, and does not depend on the orientation of the dipole in the simple model.

In figure we see the Moon MC excess-map of the dipole model of the Sun, for the period of 907 days over epochs 7-9, with usual quality cuts. The shadow shows a similar width and deflection to the data, despite the crudeness of the model. In figure 10.8 are the differential and integral plots from this excess-map. They both appear to show good matches between MC and the data. But remarkably, both the data and MC in the integrated plots plateau to very similar values. A dipole

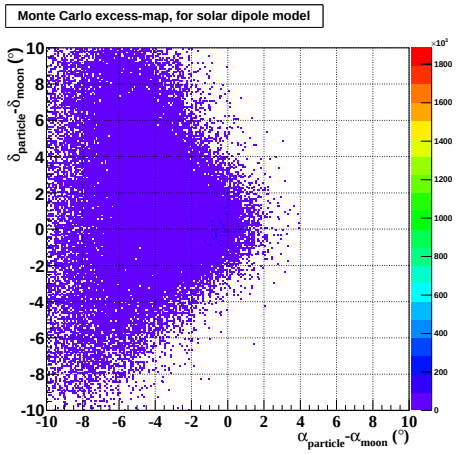

Figure 10.7: Excess map for the Sun MC dipole model, with the sign of shadowed events reversed so they are seen as an excess. Cuts are N_{fit}>40, zenith angle<60° and the simulation is over the period of epochs 7-9.

model is a very good approximation of the coronal field for the solar minimum of cycle 23. However, in the crudeness of the model we have neglected an important effect. We chose the axis of the solar dipole to be parallel to that of the Earth, and nearly perpendicular to the plane of the ecliptic. A dipole axis lower in ecliptic heliographic latitude points in the direction of the Earth for periods of the Earth's orbit. At these times lower energy events are more likely to be shadowed, which increases the fraction of shadowed particles. Early studies found an order 10% difference in the fraction of shadowed particles due to this effect, and studies are ongoing.

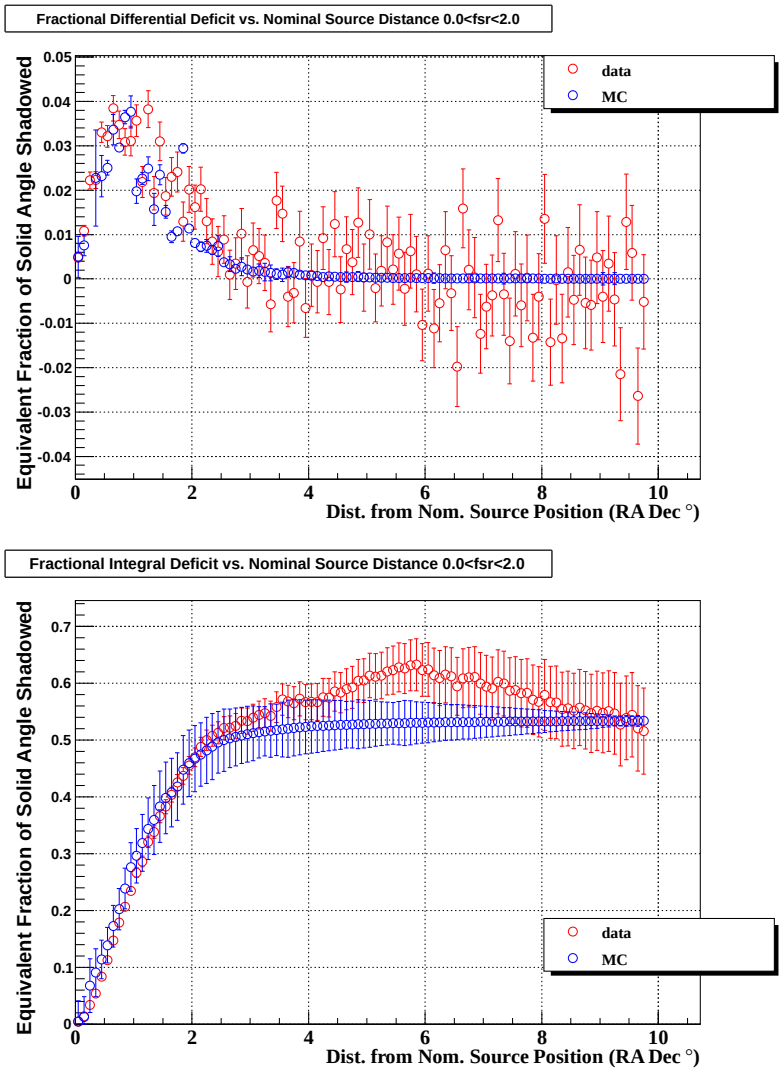

Figure 10.8: Top: Differential fractional deficit. Bottom: Integrated fractional deficit. Data and the dipole model of the coronal field from the Sun MC. Cuts are N_{fit}>40, zenith angle<60°.

Conclusions

Using Milagro data, from 20th September 2005 to 15th March 2008, we observed the Moon to a depth of 60σ, the most significant object yet seen by an air-shower array, and the Sun to a depth of 35σ.

We developed a Monte Carlo designed to simulate the Milagro Moon shadow over this period. The simulated Moon shadow agrees with the Moon shadow in data to within 0.1°, –a remarkable agreement given the complexity of the Milagro detector and the physics involved in the formation of a Moon shadow in TeV cosmic rays.

The Monte Carlo Moon shadow was used in the first attempt, in the 50 years since their first operation, to calibrate the energy scale of an air shower array by comparison to the Moon shadow in data. The measurements and simulation agree to within the uncertainties of 0.02° for properties of the Moon shadow that are less sensitive to the geomagnetic field (position and width of the shadow in declination). However, they disagree by about 0.15° for parameters sensitive to the magnetic field (the shadow position and width in right-ascension), making it difficult to draw conclusions about the energy scale, whose effects are about this size. In order to calibrate the energy scale of Milagro a better model of the magnetic field is needed.

A Monte Carlo independent search of the data was performed to search for the antiproton Moon shadow. No shadow was found, and the fit and its uncertainty were used to place a 95% confidence level upper limit on the $\bar{p}$/particle ratio. A model-free fit was performed over a probable range of parameter space where the antiproton Moon shadow was likely to occur. Invoking the Moon Monte Carlo only to find the ratio of particle/proton triggers, this search yielded 95% upper limits on $\bar{p}/p$ of 3.4 to 3.9% in this range. Using Monte Carlo to find the antiproton shadow location, a $\bar{p}/p$ limit of 3% was found for the case where antiprotons have the same spectrum as protons. The median energy of Milagro triggers for such a spectrum would be 1.7 TeV.

The stability of the Sun's shadow in cosmic rays was observed over the entire operation of Milagro from 2000 to 2008. In yearly data sets, a clear anti-correlation was shown between the fraction of particles shadowed by the Sun—given the Sun's geometrical area—and the sunspot number, which is a measure of solar activity. As the solar magnetic cycle progressed from maximum phase in 2000 to minimum phase in 2008 the fraction of particles shadowed by the Sun increased. The TeV cosmic-ray Sun shadow is here seen to be sensitive to the Sun's magnetic field as it progresses though its magnetic cycle. At solar minimum a simulation of the Sun's shadow was performed, modeling the coronal magnetic field as a dipole. It was found to be consistent with the data for this period, whilst the effects of the orientation of the dipole are the subject of further studies.

Given the quality of the Monte Carlo reproduction of Milagro Moon shadow in data, the next step would be to model the Moon's shadow using a more realistic geomagnetic field. Slight improvements in the performance of the Moon Monte

Carlo could lead to an improved modeling of the data shadow and a unique energy calibration scale may be found.

The limit on the $\bar{p}/p$ flux ratio depends on the specific antiproton spectra models. The measured upper limit to the shadow fraction and the supplied Milagro cosmic-ray effective area curves can be used to test alternative models of the $\bar{p}$ spectrum.

Given its success in modeling the Moon, the Monte Carlo can also be used in complex models of the Sun's shadow, beyond a simple dipole, –such as the PFSS model. The goal would be to reproduce the shadow seen by Milagro in 2006 and 2007, which are full years of data in the period the Moon Monte Carlo was designed to work. Success in this area could lead to attempts to extend the Monte Carlo to pre-epoch 7 data, and model the Sun's shadow closer to maximum.

Bibliography

[1] D. J. Bird et al., *ApJ* **441**, 144 (1995).

[2] W. I. Axford, *ApJ Sup. Ser.* **90**, 937 (1994).

[3] A. M. Hillas, *Ann. Rev. of Astron. and Astrophys.* **22**, 425 (1984).

[4] A. R. Bell, *Monthly Notices of the Royal Astronomical Society* **353**, 550 (2004).

[5] J. H. Buckley et al., *Astron. and Astrophys.* **329**, 639 (1998).

[6] F. Halzen and D. Hooper, *Reports on Progress in Physics* **65**, 1025 (2002).

[7] D. Smart and M. Shea, *Advances in Space Research* **44**, 1107 (2009), Cosmic Rays From Past to Present.

[8] F. Aharonian, J. Buckley, T. Kifune, and G. Sinnis, *Reports on Progress in Physics* **71** (2008).

[9] A. Szabo and R. Protheroe, *Astropart. Phys.* **2** (1994).

[10] J. A. Simpson, W. Fonger, and S. B. Treiman, *Phys. Rev.* **90**, 934 (1953).

[11] F. Schmidt, CORSIKA Shower Images, `http://www.ast.leeds.ac.uk/~fs/showerimages.html`.

[12] M. Amenomori et al., *Nucl. Inst. & Meth. A* **288** (1990).

[13] A. Aloisio et al., The ARGO-YBJ experiment in Tibet, in *Il Nuovo Cimento 24C*, volume 739 of *Il Nuovo Cimento 24C*, 2001.

[14] A. Abdo et al., *Astrophysical Journal Letters* **700** (2009).

[15] A. A. Abdo et al., *ApJ* **698**, 2121 (2009).

[16] M. Amenomori et al., Tibet AS-gamma site, `http://www.icrr.u-tokyo.ac.jp/em/index.html`.

[17] M. Leonor, *Search for a TeV Component of Gamma-Ray Bursts using the Milagro Detector*, PhD thesis, University of California, Irvine, 2000.

[18] Milagro, Milagro UMD site, `http://umdgrb.umd.edu/cosmic/milagro.html`.

[19] R. Fleysher, *Search for gamma ray emission from galactic plane with Milagro*, PhD thesis, NYU, 2003.

[20] A. A. Abdo, *Discovery of locaized TeV gamma-ray sources and diffuse TeV gamma-ray-ray emission from the galactic plane with Milagro using a new background rejection technique*, PhD thesis, Michigan State University, 2007.

[21] UMich, The Celestial Coordinate System, http://www.astro.lsa.umich.edu/undergrad/Labs/coords/index.html.

[22] D. Alexandreas et al., *Nucl. Inst. & Meth.* **A328** (1993).

[23] T. Li and Y. Ma, *ApJ* **272**, 317 (1983).

[24] D. Heck, J. Knapp, J. N. Capdevielle, G. Schatz, and T. Thouw, *CORSIKA: a Monte Carlo code to simulate extensive air showers.*, TIB Hannover, D-30167 Hannover (Germany), 1998.

[25] Geant4 Collaboration, S. Agostinelli, et al., *Nucl. Inst. & Meth. A* **506**, 250 (2003).

[26] R. W. Ellsworth, Calculation of the Trigger Rate from Geant 4 Monte Carlo Data, Collaboration Memorandum.

[27] G. Clark, *Phys. Rev.* **108** (1957), iss. 2.

[28] D. E. Alexandreas et al., *Phys. Rev. D* **43**, 1735 (1991).

[29] I. V. Moskalenko, A. W. Strong, J. F. Ormes, M. S. Potgieter, and U. W. Langner, Secondary antiprotons in cosmic rays, in *International Cosmic Ray Conference*, volume 5 of *International Cosmic Ray Conference*, pp. 1868–1871, 2001.

[30] F. Donato, D. Maurin, P. Salati, A. Barrau, G. Boudoul, and R. Taillet, *ApJ* **563**, 172 (2001).

[31] A. Barrau, G. Boudoul, F. Donato, D. Maurin, P. Salati, and R. Taillet, *Astron. and Astrophys.* **388**, 676 (2002).

[32] J. Alcaraz et al., *Phys. Lett. B* **461**, 387 (1999).

[33] O. Adriani et al., *"Nature"* **458**, 607 (2009).

[34] I. Cernuda, *Astroparticle Physics* **34**, 59 (2010).

[35] P. Blasi and P. D. Serpico, *Phys. Rev. Lett.* **103**, 081103 (2009).

[36] F. W. Stecker and A. W. Wolfendale, *Nature* **309**, 37 (1984).

[37] S. A. Stephens and R. L. Golden, *Space Sci. Rev.* **46**, 31 (1988).

[38] F. Donato, D. Maurin, P. Brun, T. Delahaye, and P. Salati, *Phys. Rev. Lett.* **102**, 071301 (2009).

[39] O. Adriani et al., *Phys. Rev. Lett.* **102**, 051101 (2009).

[40] M. Cirelli, M. Kadastik, M. Raidal, and A. Strumia, *Nucl. Phys. B* **813**, 1 (2009).

[41] T. Bringmann and P. Salati, *Phys. Rev. D* **75**, 083006 (2007).

[42] T. Appelquist, H. Cheng, and B. A. Dobrescu, *Phys. Rev. D* **64**, 035002 (2001).

[43] H.-C. Cheng, K. T. Matchev, and M. Schmaltz, *Phys. Rev. D* **66**, 056006 (2002).

[44] G. Servant and T. M. P. Tait, *Nuclear Physics B* **650**, 391 (2003).

[45] M. Amenomori et al., *Astropart. Phys.* **28**, 137 (2007).

[46] A. Borione et al., *Phys. Rev. D* **49** (1994).

[47] D. J. Boersma, L. Gladstone, A. Karle, and for the IceCube Collaboration, *ArXiv e-prints* (2010).

[48] P. Achard et al., *Astropart. Phys.* **23, issue 4** (2005).

[49] M. Ambrosio et al., *Astropart. Phys.* **20, Issue 2** (2003).

[50] J. Cobb et al., *Phys. Rev. D* **61** (2000).

[51] Y. Andreyev et al., *Cosmic Research* **40 issue 6** (2002).

[52] R. Caballero et al., editors, *MINOS Observations of Shadowing in the Muon Flux Underground*, Merida, 2007, ICRC.

[53] C. C. Finlay et al., *Geophysical Journal International* **183**, 1216 (2010).

[54] N. A. Tsyganenko and M. I. Sitnov, *J. Geophys. Res.* **110**, A03208 (2005).

[55] N. Tsyganenko, Modeling the Earth's Magnetosphere Using Spacecraft Magnetometer Data, `http://geo.phys.spbu.ru/~tsyganenko/modeling.html`.

[56] G. Di Sciascio and R. Iuppa, *ArXiv e-prints* (2010).

[57] A. Karle and et al., Observation of the Shadowing of Cosmic Rays by the Moon and the Sun, in *International Cosmic Ray Conference*, volume 4 of *International Cosmic Ray Conference*, pp. 460–+, 1991.

[58] A. Oshima et al., *Astropart. Phys.* **33**, 97 (2010).

[59] O. Adriani et al., *Phys. Rev. Lett.* **105**, 121101 (2010).

[60] P. Brun, *The European Physical Journal C - Particles and Fields* **56**, 27 (2008), 10.1140/epjc/s10052-008-0659-6.

[61] Y. Asaoka et al., *Phys. Rev. Lett.* **88**, 051101 (2002).

[62] K. Abe et al., *Physics Letters B* **670**, 103 (2008).

[63] M. Boezio et al., *ApJ* **487**, 415 (1997).

[64] M. Boezio et al., *ApJ* **561**, 787 (2001).

[65] A. S. Beach et al., *Phys. Rev. Lett.* **87**, 271101 (2001).

[66] G. D. Sciascio and R. Iuppa, *Nucl. Inst. & Meth. A* **In Press, Corrected Proof**, (2010).

[67] G. Basini, The Flux of Cosmic Ray Antiprotons from 3.7 to 24 GeV, in *ICRC*, volume 3 of *International Cosmic Ray Conference*, pp. 77–+, 1999.

[68] J. W. Mitchell et al., *Phys. Rev. Lett.* **76**, 3057 (1996).

[69] S. P. Ahlen et al., *Phys. Rev. Lett.* **61**, 145 (1988).

[70] R. E. S. others, *Advances in Space Research* **9**, 65 (1989).

[71] E. A. Bogomolov et al., Galactic Antiproton Spectrum in the 0.2-5 GEV Range, in *ICRC*, volume 2 of *International Cosmic Ray Conference*, pp. 72–+, 1987.

[72] R. L. Golden et al., *Phys. Rev. Lett.* **43**, 1196 (1979).

[73] R. L. Golden, B. G. Mauger, S. Nunn, and S. Horan, *Astrophys. Lett.* **24**, 75 (1984).

[74] A. Buffington, S. M. Schindler, and C. R. Pennypacker, *ApJ* **248**, 1179 (1981).

[75] S. T. Suess et al., *Space Sci. Rev.* **83**, 75 (1998).

[76] A. Balogh, L. J. Lanzerotti, S. T. Suess, D. H. Hathaway, and S. T. Suess, Solar cycle 23, in *The Heliosphere through the Solar Activity Cycle*, Springer Praxis Books, pp. 21–39, Springer Berlin Heidelberg, 2008.

[77] J. Jiang, R. Cameron, D. Schmitt, and M. Schüssler, *ApJ* **709**, 301 (2010).

[78] D. Hathaway, D. Nandy, and R. Wilson, *ApJ* **589**, 665 (2003).

[79] M. A. Hapgood, *"Planetary and Space Science"* **40**, 711 (1992).

[80] E. N. Parker, *Interplanetary dynamical processes.*, New York, Interscience Publishers, 1963.

[81] L. A. Fisk, *J. Geophys. Res.* **101**, 15547 (1996).

[82] S. M. White, Coronal Magnetic Field Measurements Through Gyroresonance Emission, in *Solar and Space Weather Radiophysics*, edited by D. E. Gary and C. U. Keller, volume 314 of *Astrophysics and Space Science Library*, pp. 89–113, Springer Netherlands, 2005.

[83] T. Hoeksema, The Wilcox Solar Observatory, `http://wso.stanford.edu`.

[84] W. T. Thompson, *Astron. and Astrophys.* **449**, 791 (2006).

[85] C. N. Arge and V. J. Pizzo, *J. Geophys. Res.* **105**, 10465 (2000).

[86] M. D. Altschuler and G. Newkirk, *Solar Physics* **9**, 131 (1969).

[87] K. H. Schatten, J. M. Wilcox, and N. F. Ness, *Solar Physics* **6**, 442 (1969).

[88] J. T. Hoeksema, *Structure and Evolution of the Large Scale Solar Heliospheric Magnetic Fields*, PhD thesis, Stanford University, 1984.

[89] Y. Wang and N. R. Sheeley, Jr., *ApJ* **392**, 310 (1992).

[90] G. Aielli et al., *ApJ* **729**, 113 (2011).

[91] M. Amenomori et al., *Phys. Rev. D* **47**, 2675 (1993).

[92] M. Amenomori et al., *ApJ* **541**, 1051 (2000).

[93] K. Asakimori et al., *ApJ* **502**, 278 (1998).

[94] A. D. Panov et al., *Bulletin of the Russian Academy of Science, Phys.* **71**, 494 (2007).

[95] T. Sanuki et al., *ApJ* **545**, 1135 (2000).

[96] O. Adriani et al., *Science* (2011).

[97] M. Boezio et al., *Astropart. Phys.* **19**, 583 (2003).

[98] H. S. Ahn et al., *ApJ* **707**, 593 (2009).

[99] L. E. Garey and C. J. Gladwin, *International Journal of Computer Mathematics* (1992).

[100] R. W. Ellsworth and A. I. Mincer, Comparison of Magnetic Deflection Calculations and Study of the Energy Dependence of the Deflection Direction, Collaboration Memorandum.

[101] G. di Sciascio and R. Iuppa, *Nucl. Inst. & Meth. A* **630**, 301 (2011).

[102] I. Antcheva et al., *Computer Physics Communications* **180**, 2499 (2009), 40 YEARS OF CPC: A celebratory issue focused on quality software for high performance, grid and novel computing architectures.